University of Wollongong

Research Online

University of Wollongong Thesis Collection 1954-2016

University of Wollongong Thesis Collections

2015

Physics of MR image distortion: Impact on breast cancer radiotherapy

Amy Walker
University of Wollongong

Follow this and additional works at: https://ro.uow.edu.au/theses

University of Wollongong

Copyright Warning

You may print or download ONE copy of this document for the purpose of your own research or study. The University does not authorise you to copy, communicate or otherwise make available electronically to any other person any copyright material contained on this site.

You are reminded of the following: This work is copyright. Apart from any use permitted under the Copyright Act 1968, no part of this work may be reproduced by any process, nor may any other exclusive right be exercised, without the permission of the author. Copyright owners are entitled to take legal action against persons who infringe their copyright. A reproduction of material that is protected by copyright may be a copyright infringement. A court may impose penalties and award damages in relation to offences and infringements relating to copyright material. Higher penalties may apply, and higher damages may be awarded, for offences and infringements involving the conversion of material into digital or electronic form.

Unless otherwise indicated, the views expressed in this thesis are those of the author and do not necessarily represent the views of the University of Wollongong.

Recommended Citation

Walker, Amy, Physics of MR image distortion: Impact on breast cancer radiotherapy, Doctor of Philosophy thesis, Faculty of Engineering, University of Wollongong, 2015. https://ro.uow.edu.au/theses/4578

Research Online is the open access institutional repository for the University of Wollongong. For further information contact the UOW Library: research-pubs@uow.edu.au

PHYSICS OF MR IMAGE DISTORTION: IMPACT ON BREAST CANCER RADIOTHERAPY

A Dissertation Submitted in Fulfilment of
the Requirements for the Award of the Degree of

Doctor of Philosophy

from

UNIVERSITY OF WOLLONGONG

by

Amy L. Walker

B.Med.Rad.Phys.Adv (Hons)

Centre for Medical Radiation Physics
Faculty of Engineering

2015

© Copyright 2015

by

Amy L. Walker

ALL RIGHTS RESERVED

Table of Contents

List of Tables

List of Figures

PHYSICS OF MR IMAGE DISTORTION: IMPACT ON BREAST CANCER RADIOTHERAPY

Amy L. Walker

A Thesis for Doctorate of Philosphy

Centre for Medical Radiation Physics
University of Wollongong

ABSTRACT

Magnetic Resonance Imaging (MRI) has superior soft tissue contrast compared to Computed Tomography (CT). This soft tissue contrast can be utilised to enable improvements in delineation of tumour and organ at risk volumes for radiotherapy treatment planning. CT is the imaging modality currently utilised for radiotherapy treatment planning. It provides accurate geometry of patient anatomy and provides electron density information as required for dose calculations. Currently, MR images are generally fused with CT images to enable the generation of radiotherapy treatment plans. There are continual advances being made to enable use of MR images alone for radiotherapy treatment plan dose calculations, as well as for in-room image guidance.

Geometric distortions associated with MRI are still a limiting factor in its more widespread application for radiotherapy treatment planning, where accuracy is a crucial requirement. Systematic distortions result from inhomogeneities in the magnetic field of the scanner, and nonlinearities in the gradient fields which combine to localise the signal from within the scanner. The patient introduces additional geometric distortions from differing tissue susceptibilities also leading to geometric uncertainties. The aim of this thesis was to quantify the distortions across a large field of view as would be required for radiotherapy treatment planning and determine implications of these geometric distortions on whole breast radiotherapy.

The initial work conducted in this study looked at quantifying systematic geometric distortions associated with MRI to determine the magnitude of geometric uncertainty when utilising MRI in the treatment planning process. This is of particular importance if considering the use of MR images alone for treatment planning purposes. A 2-dimensional diagnostic phantom was initially scanned on four diagnostic scanners with a number of standard clinical imaging sequences. Distortion vector maps were found to differ between scanners due

to the individual performance specifications for each system. Differences in distortion magnitude were observed for different acquisition sequences. A comparison was made between images acquired with and without the application of a vendor supplied correction algorithm for one of the scanners. The maximum distortion observed was reduced from 5.0 mm to 2.3 mm for a spoiled gradient echo sequence when the distortion correction algorithm was applied. The distortion maps were compared to the positions of various anatomical sites within the bore of MRI scanners. Distortions are larger in magnitude in regions where the lung and breast volumes can be located.

The phantom utilised in the first section of this study did not enable the determination of distortions across a large field of view (FOV) as required for the purposes of radiotherapy treatment planning. Hence, a phantom was developed to meet this need. This phantom was then scanned on a MRI scanner dedicated for imaging for radiotherapy, to quantify the residual distortions observed on the system. Two approaches for reducing geometric distortions were examined, namely the application of a vendor-supplied 3D correction algorithm and image acquisition with a continuously moving table. The maximum distortion was halved when the vendor supplied 3D correction algorithm was applied as opposed to only the 2D correction algorithm. For a standard spin echo sequence, the maximum distortion was reduced from 9.81 mm to 4.37 mm. Differences in distortion distribution were observed between images acquired with a conventional static couch to those acquired with a continuously moving table (TimCT). TimCT enabled the whole phantom (length of 513 mm) to be imaged, whereas the conventional static table acquisition only imaged 71% of the volume. Additionally, the magnitude of the distortions observed was also reduced from 6.1 mm (71% phantom volume) to 4.4 mm with a table speed of 1 mm/s (100% phantom volume). While the distortions are reduced with the moving table acquisition, blurring is introduced into the image due to the movement of the table and the amount of distortion increases with increasing table speed (maximum distortion 5.8 mm at a table speed of 2 mm/s).

The final section of this thesis investigates the implications of geometric distortions from both system and patient sources, on whole breast radiotherapy treatment planning. A retrospective study was performed on data from 18 patients that underwent whole breast radiotherapy as part of their treatment. To simulate the effects of MRI systematic geometric distortions, deformation maps obtained from phantom measurements on two different scanners were used to deform the original patient CT images. To assess the impact of combined

patient and systematic geometric distortions, CTs of the patient were deformably registered to the corresponding patient MRI. Whole breast IMRT treatment plans were generated on these altered CT datasets then the radiation dose recomputed on the original image, in order to determine the impact of these distortions on the treatment planning process. The effects of the systematic distortions alone had a minimal dosimetric impact. The combined effects of the patient and system induced geometric distortions resulted in distortions within the lung of 11.3 $\pm$ 8.6 mm compared to 3.0 $\pm$ 1.3 mm with only the systematic distortions present. A dosimetric impact was observed for 8 of the 18 patients, with a mean variation in PTV $V_{47.5Gy}$ coverage of 0.2 $\pm$ 2.2% across all patients, indicating that the geometric distortions resulting from the patient within the magnetic field is the largest contributing factor for whole breast radiotherapy.

When considering incorporating MRI into the radiotherapy treatment planning workflow, geometric distortions must be considered. Geometric distortions should be quantified on any scanner to be utilised for radiotherapy so that the limitations of the system are known and the potential impact assessed.

KEYWORDS: Magnetic Resonance Imaging, Geometric Distortion, Phantom, Breast Radiotherapy

Acknowledgements

Firstly, I would like to saw a huge thank you to my supervisors for getting me through the past three and a half years. To Peter Metcalfe, thank you for the continued support over the past few years, for always being around (on my good and bad days) when I needed direction, focus and someone to keep me on track to get this "stuff" done. Thank you to Lois Holloway. Her supervision, patience drive and motivation has been invaluable in keeping my driven and motivated to progress my work and keep looking for now opportunities. To Gary Liney, thank you for the MRI expertise brought to this project. This expertise and the advice on my publications definitely helped my project along and kept things on track.

I would like to thank the staff at Liverpool and Macarthur Cancer Centres for their assistance and support throughout the PhD. I would particularly like to thank Vikneswary Batumalai and Shivani Kumar for having the patience to teach me treatment planning and always being up for a chat, Robba Rai and Ewa Juresic for the MRI scanning and singing sessions, and Michael Jameson for discussions about projects and future prospects. To Prof. Geoff Delaney, Dr. Miriam Boxer, Dr. Mei Yap and Dr. Eng-Siew Koh, thank you for the numerous plan checks conducted throughout this project.

Thank you to Jason Dowling and the guys at CSIRO for all of the support for the image registration component of this project and allowing me to visit and get things all set up. Thanks specifically to David Rivest-Henault for assistance with the deformable image registration, Neil Burdett for software support and Shekar Chandra for assistance with image visualisation.

A lot of this work was very dependent on the acquisition and development of MRI phantoms. Thank you to Peter Greer for supplying the initial phantom which got the project

kick started, Jonathan Knott for helping to put together the design drawings for the developed phantom and Craig Davis for constructing the phantom. A huge thanks to Carrie Glide-Hurst for providing phantom data and engaging in collaborative discussions. To Elise Pogson, Kylie Dundas and Haijie Jin, thank you for the work conducted on the breast radiotherapy planning scripts and showing my how to use the end product. It definitely helped ensure that this project was completed in a timely fashion. A big thank you to the past and present students and staff at the Centre for Medical Radiation Physics (CMRP) for making the past several years quite enjoyable and for helping on another along the way. To Jayde, Sally, Valentina, Pauline, Lauren, Brad, Weaver, Anthony, Anya, Jeremy, Stephen and Dean (and others) thank you for the numerous coffee sessions and overall great times, something I am sure I will miss as I move on from this chapter. Thank you too to the students from around the world who have conduced some form of research through Liverpool Hospital and the Ingham Institute. It has been a pleasure to meet you all and made the time spent at the hospital enjoyable and interesting.

I wish to acknowledge the funding assistance supplied by the APA scholarship and the Liverpool and Macarthur Therapy Centre Trust Funds. Thank you to the CMRP for the opportunities received to travel nationally and internationally, allowing me to promote my work and giving me opportunities to network and enhance my career prospects.

Finally, I would like to thank my family and Pete, for keeping me sane throughout these past few years.

Publication List

Published

A. Walker, G. Liney, L. Holloway, J. Dowling, D. Rivest-Hénult, P. Metcalfe, "Continuous table acquisition MRI for radiotherapy treatment planning: distortion assessment with a new extended 3D volumetric phantom", *Medical Physics*, 42, (4), 1982-1991 (2015)

A. Walker, G. Liney, P. Metcalfe, L. Holloway, "MRI distortion: considerations for MRI based radiotherapy treatment planning", *Australasian Physical and Engineering Sciences in Medicine*, 37, (1), 103-113 (2014)

P. Metcalfe, G. Liney, L. Holloway, **A. Walker**, M. Barton, G. P. Delaney, S. Vinod, W. Tome, "The Potential for an Enhanced Role for MRI in Radiation-Therapy Treatment Planning", *Technology in Cancer Research and Treatment*, 12, (5), 429-446 (2013)

In Submission

A. Walker, P. Metcalfe, G. Liney, V. Batumalai, K. Dundas, C. Glide-Hurst, G.P. Delaney, M. Boxer, M.L. Yap, J. Dowling, D. Rivest-Hénult, E. Pogson, L. Holloway, "MRI geometric distortion: Impact on tangential whole breast IMRT ", *JACMP*, **(In Submission)**

A. Xing, L. Holloway, S. Arumugam, **A. Walker**, G. Goozee, E. Juresic, R. Rai, L. Cassapi, S.K. Vinod, G.P. Liney, "Commissioning and quality control of a dedicated wide bore 3T MRI simulator for radiotherapy planning", *International Journal of Cancer Therapy and Oncology*, **(In Submission)**

Conference Presentations

A. Walker, P. Metcalfe, G. Liney, V. Batumalai, K. Dundas, C. Glide-Hurst, G. Delaney, M. Boxer, ML. Yap, J. Dowling, D. Rivest-Hénult, E. Pogson, L. Holloway, *Impact of MRI geometric distortion on tangential whole breast IMRT*, Poster presentation, MR in RT Symposium, Lund, Sweden, 2015

A. Walker, G. Liney, L. Holloway, J. Dowling, D. Rivest-Hénult, P. Metcalfe, *Variations in geometric distortion using static and moving table acquisition for radiotherapy treatment planning applications*, Oral presentation, World Congress on Medical Physics and Biomedical Engineering, Toronto, Canada, 2015

A. Walker, G. Liney, L. Holloway, J. Dowling, D. Rivest-Hénult, P. Metcalfe, *3D mapping of geometric distortion using static and moving table acquisitions for radiotherapy treatment planning applications*, Oral presentation, International Society for Magnetic Resonance in Medicine 23rd Annual Meeting, Toronto, Canada, 2015

A. Walker, V. Batumalai, K. Dundas, G. Delaney, M. Boxer, ES. Koh, ML. Yap, P. Metcalfe, G. Liney, J. Dowling, L. Holloway, *Impact of MRI geometric distortion on tangential IMRT breast plans*, Oral presentation, MedPhys14, Sydney, Australia, 2014

A. Walker, V. Batumalai, K. Dundas, G. Delaney, M. Boxer, ES. Koh, ML. Yap, P. Metcalfe, G. Liney, J. Dowling, L. Holloway, *Impact of MRI geometric distortion on tangential IMRT breast plans*, Oral presentation, Combined Scientific Meeting, Melbourne, Australia, 2014

A. Walker, L. Holloway, P. Metcalfe, J. Dowling, G. Liney, *An assessment of continuous table acquisition for reducing MRI distortion in radiotherapy imaging using a new 3D volumetric phantom*, Electronic and static posters, Combined Scientific Meeting, Melbourne, Australia, 2014

A. Walker, V. Batumalai, K. Dundas, G. Delaney, M. Boxer, ES. Koh, ML. Yap, E. Pogson, T. Young, P. Metcalfe, L. Holloway, *Comparison of planning techniques for supine whole breast treatments*, Electronic poster, Combined Scientific Meeting, Melbourne, Australia, 2014

A. Walker, L. Holloway, P. Metcalfe, G. Liney, *Phantom development for full field of view distortion assessment on an MRI simulator*, Oral presentation, MR in RT Symposium, Saint Louis Missouri, USA, 2014

A. Walker, L. Holloway, G. Liney, P. Metcalfe, *A comparison of MRI distortion between scanners and sequences for radiotherapy purposes*, Oral presentation, AAPM, Indianapolis, Indiana, USA, 2013

A. Walker, G. Liney, P. Metcalfe, L. Holloway, *A comparison of MRI distortion between scanners and sequences for radiotherapy purposes*, Oral presentation, MedPhys13, Sydney, Australia, 2013

A. Walker, G. Liney, L. Holloway, S. Deshpande, P. Metcalfe, *An assessment of MRI distortion for the purpose of radiotherapy treatment planning*, Electronic poster, 2nd ESTRO Forum, Geneva, Switzerland, 2013

A. Walker, L. Holloway, G. Liney, P. Metcalfe, *Phantom prototype development for MRI distortion analysis for radiotherapy treatment planning application*, Oral presentation, MedPhys12, Sydney, Australia, 2012

A. Walker, L. Holloway, P. Metcalfe, *Prototype designs of a phantom to assess MRI distortion for radiotherapy treatment planning*, Oral presentation, EPSM, Gold Coast, Australia, 2012

Invited Talks

A. Walker, *MRI distortion and the impact for breast RTP*, Presented at the MRI linac collaborators meeting, Sydney, Australia, December 2014

P. Metcalfe, **A. Walker**, *Distortion correction for MRI treatment planning and MRI Linac*, Presented at Micro-Mini & Nano Dosimetry and Prostate Cancer Treatment Workshop, Port Douglas, Australia, October 2014

List of Abbreviations

3D-CRT	Three-Dimensional Conformal Radiotherapy
AAPM	American Association of Physicists in Medicine
Ant	Anterior
B_0	Magnetic Field
BW	Bandwidth
CISS	Constructive Interface in Steady State
CSIRO	Commonwealth Scientific and Industrial Research Organisation
CTV	Clinical Target Volume
CT	Computed Tomography
DSV	Diameter of Spherical Volume
DVH	Dose Volume Histogram
EBRT	External Beam Radiotherapy
FOV	Field Of View
Gd	Gadolinium
GRE	Gradient Echo
HU	Hounsfield Units
IGRT	Image Guided Radiotherapy
IMAT	Intensity Modulated Arc Therapy

IMRT	Intensity Modulated Radiation Therapy
MRA	Magnetic Resonance Angiography
MRI	Magnetic Resonance Imaging
MU	Monitor Units
MV	Megavoltage
NMR	Nuclear Magnetic Resonance
OAR	Organs At Risk
PBI	Partial Breast Irradiation
Post	Posterior
ppm	Parts Per Million
PTV	Planning Target Volume
QA	Quality Assurance
RF	Radio Frequency
RTP	Radiotherapy Treatment Planning
s-CT	Substitute CT
SE	Spin Echo
SMILI	Simple Medical Imaging Library Interface
SMS	Sliding Multislice
SNR	Signal-to-Noise Ratio
ss-TSE	Single Shot Turbo Spin Echo
TE	Echo Time
TimCT	Total Imaging Matrix, Continuous Table
TPS	Treatment Planning Systems

TR	Repetition Time
TSE	Turbo Spin Echo
T	Tesla
UTE	Ultra-Short TE
V-interp	Volume Interpolated

Chapter 1

Introduction

In radiotherapy, there have been continuous advancements in imaging and treatment techniques. In order for new and emerging technologies to be utilised in a clinical scenario on a daily basis, they need to show merit and benefit over the existing technologies.

The utilisation of Magnetic Resonance Imaging (MRI) in radiotherapy is increasing for the purposes of treatment planning and image guidance [1]. MRI offers superior soft tissue information compared with Computed Tomography (CT), the current primary imaging modality in radiotherapy. This improved information can improve the accuracy in delineation of tumour and organ structures, providing more targeted radiotherapy for patients [2].

One of the underlying issues with MRI that has previously restricted its widespread utilisation in radiotherapy is the geometric distortions inherent to the acquisition of images [3]. These result from both systematic sources, from the specific performance specifications of the MRI scanner and patient induced factors resulting from differences in magnetic properties of varying tissues.

This thesis is an investigation of geometric MRI distortion and the potential consequences for radiotherapy treatment planning. Methods for quantifying systematic distortions on a dedicated MRI simulator are presented. This thesis also reports the implications of systematic and patient related distortions on whole breast radiotherapy treatment planning.

1.1 Project Aims

This section outlines the scope of this project by stating the project aims with associated research questions and the thesis chapters that address each research aim.

Aim 1. Compare the advantages and disadvantages of utilising MRI and CT for radiotherapy treatment planning

Research questions:

What are the advantages of utilising MRI for radiotherapy treatment planning?

What are the disadvantages and challenges of increased utilisation of MRI for radiotherapy treatment planning?

Content Overview:

Chapter 2 summarises the literature on the use of MRI in radiotherapy treatment planning (RTP). It addresses the benefits and limitations compared to CT, the current primary imaging modality for radiotherapy treatment planning. Of particular focus is MR geometric distortions in the acquired images. The causes and methods for dealing with them are investigated, as well as potential implications for RTP.

Aim 2. Quantify MRI geometric distortion utilising a diagnostic imaging phantom

Research questions:

What are the variations in geometric distortion when scanning with and without the application of a vendor supplied 2D correction algorithm?

What is the magnitude of geometric distortions corresponding to the location of common radiotherapy anatomical sites within the scanner?

What are the limitations when using a 2 dimensional diagnostic imaging phantom for measuring distortion for radiotherapy treatment planning purposes?

Content Overview:

Chapter 3 details a phantom study investigating the benefits and limitations of using a 2 dimensional diagnostic phantom to assess geometric distortion for the purposes of RTP across four different MRI scanners. It addresses a number of geometric considerations that must be made when utilising MRI for RTP, including regions of the patient anatomy that are likely to experience more substantial spatial mismapping and the effects of applying 2D correction algorithms.

Aim 3. Design and construct a full field of view 3 dimensional phantom appropriate for measuring MRI distortion for RTP

Research question:

What specifications are required for a full field of view phantom for MRI distortion assessment for radiotherapy planning?

Is the designed phantom appropriate for measuring distortion for radiotherapy treatment planning?

Content Overview:

Based on the limitations with the phantom utilised in Chapter 3, Chapter 4 details the development of a 3 dimensional, full field of view distortion phantom.

Aim 4. Measure the geometric distortion on a 3 T scanner dedicated to RTP, comparing conventional static image acquisition and acquisition with a continuously moving table

Research questions:

What is geometric performance of the MRI scanner with conventional acquisition sequences?

How do the distortion patterns obtained with a continuously moving couch compare to static couch acquisitions?

Content Overview:

Utilising the final phantom design from Chapter 4, Chapter 5 measures the distortion on a 3.0 T closed wide bore MRI scanner. Distortion is quantified for conventional acquisition techniques and compared to the distortion patterns observed when acquiring images with a continuously moving table. These 2 techniques are compared to investigate if one acquisition technique may be more useful in imaging various anatomical sites.

Aim 5. Assess the impact that MRI geometric distortion has on breast radiotherapy

Research questions:

Does MRI distortion impact the dose distribution for whole breast radiotherapy treatment planning?

Can phantom measurements adequately predict the distortions for whole breast radiotherapy?

Content Overview:

Chapter 6 investigates the impact of the MRI uncorrected distortions on whole breast radiotherapy treatments with Intensity Modulated Radiation Therapy (IMRT). The distortion impact is assessed by phantom measurements on a high field closed bore system, phantom measurements on a low field open bore system and patient specific factors on the high field scanner for tangential whole breast radiotherapy treatments.

Chapter 2

Literature Review

2.1 Radiotherapy

Radiotherapy is a routine treatment technique for cancer. The aim of radiotherapy is to utilise targeted ionising radiation to kill the cancerous cells, whilst sparing the surrounding healthy tissues. External beam radiotherapy (EBRT) involves the treatment of tumours with high energy photons produced by a linear accelerator. It was reported that as of 2012 that ideally, 48.3% of new cancer cases in Australia would receive megavoltage (MV) EBRT at some point during the course treatment [4].

2.2 Imaging for radiotherapy

Imaging of the patient anatomy plays an important role in the detection and treatment of cancer. Images are acquired during the patient diagnosis stages. If radiotherapy is prescribed, the patient will undergo additional imaging for the purposes of planning the radiotherapy treatment delivery. Figure 2.1 shows the basic radiotherapy workflow and the purpose of imaging at each stage.

2.2.1 Radiotherapy treatment planning

In radiotherapy treatment planning (RTP), the patient is set-up and imaged in the position required for their course of radiotherapy. These images are imported into the treatment planning system (TPS) where radiation oncologists will define the tumour volume(s) to be

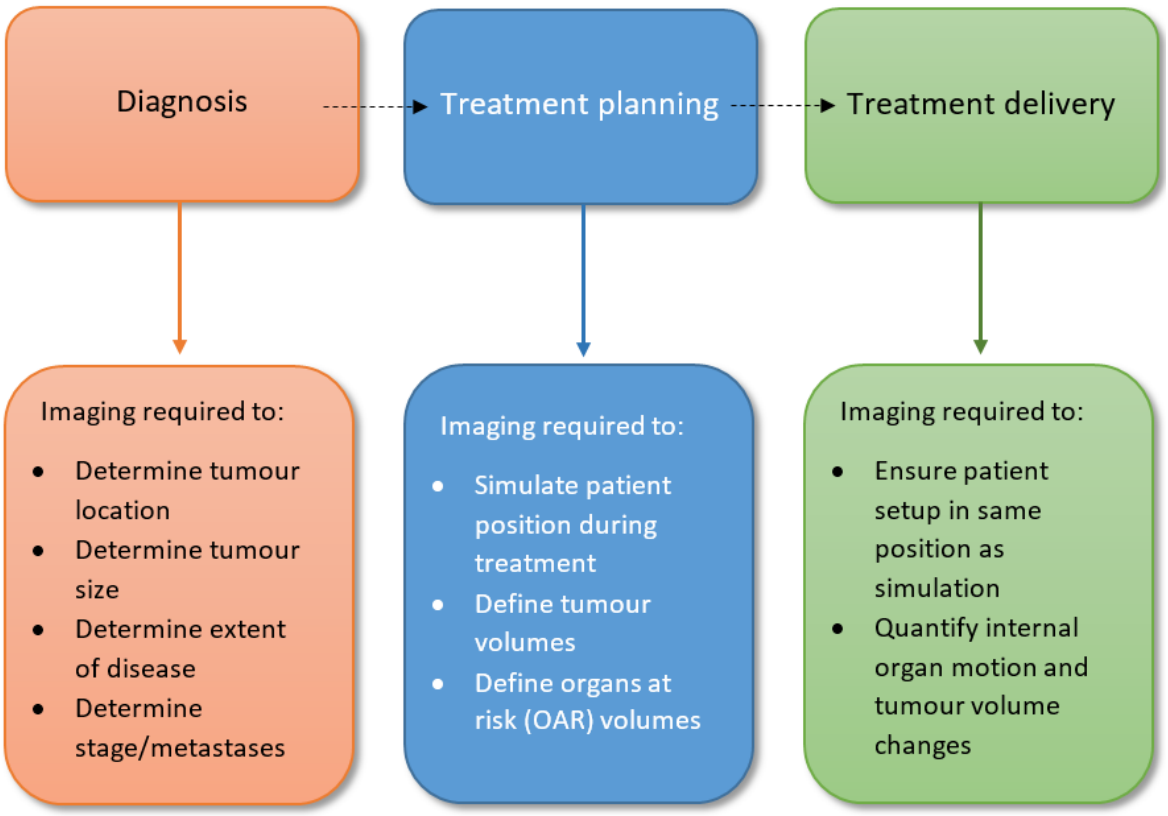

Figure 2.1: Basic workflow of the radiotherapy process.

targeted during treatment and organs at risk (OAR), which should receive the lowest dose possible to avoid damaging normal tissues.

Treatment plans are created on these images and structures. The plans are generated to meet the treatment requirements set by the radiation oncologist to meet individual patient treatment needs.

Computed Tomography (CT) uses the attenuation of x-rays through the body to create 3D anatomical images [5, 6]. CT is currently the primary imaging modality for RTP with all EBRT patients undergoing CT-simulation prior to treatment. The electron density information obtained from CT datasets is required for the treatment planning process for determining the dose distribution within the patient anatomy. CT numbers are integer values of the attenuation of x-rays through matter. The electron density information relates to the Compton interactions of high energy photons with matter [5]. Calibration curves are used to convert CT numbers (Hounsfield Units) to electron density maps [7]. Dose calculations such as convolution [8] and Monte Carlo [9] use raytracing [10] which relies on accurate electron density maps in order to generate accurate dose maps. Since CT depends on variations in x-ray attenuation through the body, there is a limit as to how well certain anatomical boundaries can be visualised, particularly between structures of similar attenuation.

In magnetic resonance imaging (MRI), the acquisition of images is based on the proton densities and relaxation properties of tissues, as opposed to variations in x-ray attenuation (Section 2.3). As such, MR images are superior in their ability to differentiate and characterise soft tissue structures compared to CT [2] (Figure 2.2). Additionally, they do not use ionising radiation to acquire the images. Due to these factors, the use of MRI for RTP has increased, with potential benefits in defining tumour extent and stage [11–13], tumour localisation and delineation [14–20], image guidance [21–27] and response monitoring [20, 28–31] during treatment. Two limitations of MRI which have inhibited its more widespread use in radiotherapy treatment planning are the geometric distortions inherent to the acquisition of these images [32] (Section 2.4) and the lack of electron density information (Section 2.5).

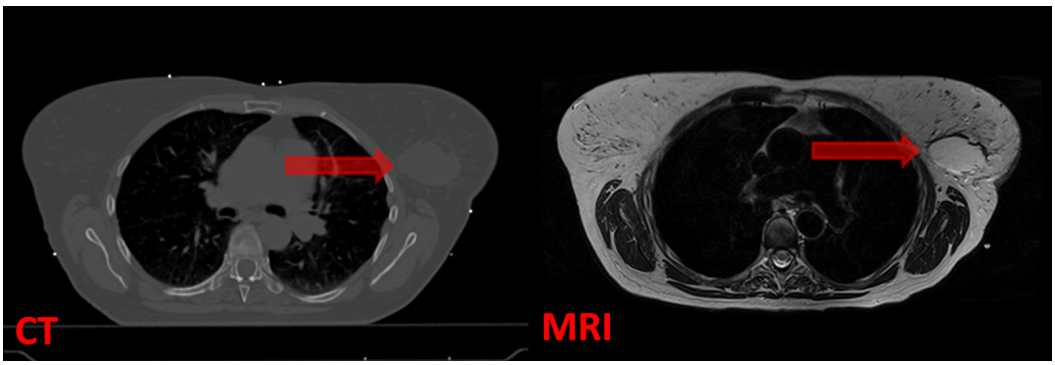

Figure 2.2: Comparison of a breast imaged with CT and MRI. Visualisation of the seroma volume is enhanced in the MR image.

2.3 Physics of MRI

MRI is based on the nuclear magnetic resonance (NMR) phenomenon - 'study of the magnetic properties of the nucleus of the atom' [33]. Since tissues within the body are primarily composed of water, the hydrogen atoms within these molecules can be manipulated and investigated.

Within a water molecule, each hydrogen nucleus spins around its own axis. In the presence of an applied external magnetic field (B_0), the nuclei begins to precess in a circular motion in the direction of B_0. The speed of precession is defined by the Lamour equation:

$$\omega_0 = B_0\gamma \tag{2.1}$$

where ω_0 is the precessional frequency, B_0 represents the strength of the applied magnetic field in Tesla (T) and γ is the gyromagnetic ratio (42.57 MHz/T for hydrogen). The precessional frequency of hydrogen is 63.86 MHz at 1.5 T and 127.71 MHz at 3 T, two common strengths of current clinical MRI scanners.

When a radio frequency (RF) pulse is applied to the human body, perpendicular to B_0 and at the same precessional frequency as the hydrogen atoms at applied field strength, the hydrogen nuclei resonate in an excited state as they receive energy from the RF pulse. The nuclei align in spin-up or spin-down states, creating a net magnetisation vector which produces the MR signal. Once the RF pulse is switched off, the nuclei undergo free decay, relaxing to their original, unexcited state. This process is governed by the relaxation times.

There are two primary relaxation times critical to the acquisition of MR images (Figure 2.3). At time t after the removal of the applied RF pulse, the recovery of the longitudinal magnetisation is defined as:

$$M_z(t) = M_0(1 - e^{-t/T1}) \tag{2.2}$$

T1 relaxation (or longitudinal relaxation) is defined as the time required for the recovery of the longitudinal magnetisation to 63% of its original value. It is often referred to as spin-lattice relaxation due to its dependence on energy transfer between excited spin states and the lattice structure of the tissue.

At time t after the removal of the applied RF pulse, the signal decay in the transverse plane is defined as:

$$M_{xy}(t) = M_0 e^{-t/T2} \tag{2.3}$$

T2 relaxation (or transverse relaxation) is defined as the time required for the transverse magnetisation to decay to 37% of its original value. It is also referred to as spin-spin relaxation time due to its dependence on the interactions of the magnetic properties between adjacent nuclei.

T2* relaxation, like T2 relaxation, involves a decay in magnetisation in the transverse plane. However T2* also incorporates magnetic field inhomogeneities and is much shorter due to the dephasing of the magnetisation for individual nuclei.

Image contrast is governed by these relaxation times which vary depending on the relaxation times of particular tissues [2]. By exploiting the differences in relaxation times in neighbouring tissues, T1, T2 or T2* weighted images can be created. Differences in repetition time between consecutive RF pulses (TR) and the times at which an echo is produced after the RF pulse (TE) enable these differences to be exploited.

In 1973, Lauterbur proposed using magnetic gradients as a way of differentiating the location of signal from within a magnetic field [34]. In modern MRI scanners, in order to differentiate where signals are originating from within the scanner, a series of gradient fields are superimposed over the main magnetic field in all three imaging planes. These gradients provide slight linear variation in the total magnetic field across the whole imaging field of view (FOV) so that no one point experiences the exact same magnetic field and the signal

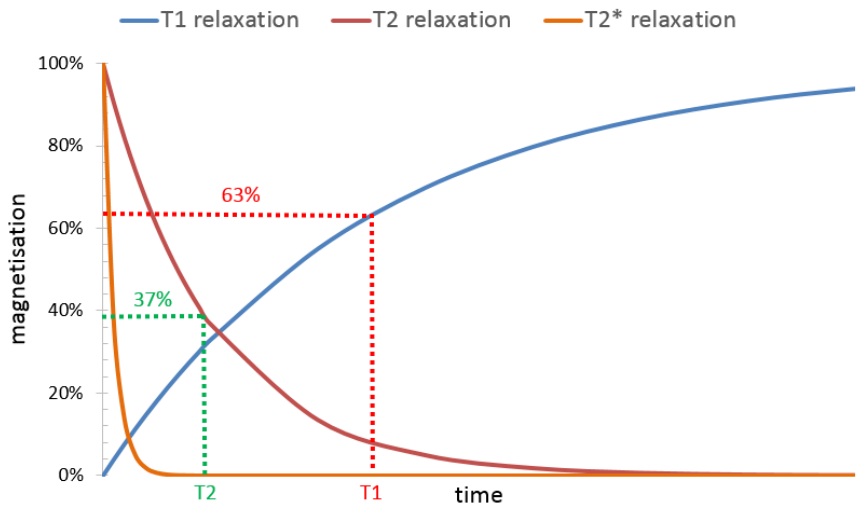

Figure 2.3: Comparison of the T1, T2 and T2* relaxation times.

information obtained can be spatially encoded. The three gradients are:

(i) Slice select gradient

(ii) Frequency encode gradient

(iii) Phase encode gradient

They are applied in a specific order, depending on the acquisition sequence in order to produce useful 3-dimensional anatomical images. The direction of these gradients will depend upon whether the images are being acquired in the axial, sagittal or coronal planes. Figures 2.4 and 2.5 show the timing of these gradients with respect to the initial RF pulse and the resulting signal for standard spin echo (SE) and gradient echo (GRE) sequences respectively.

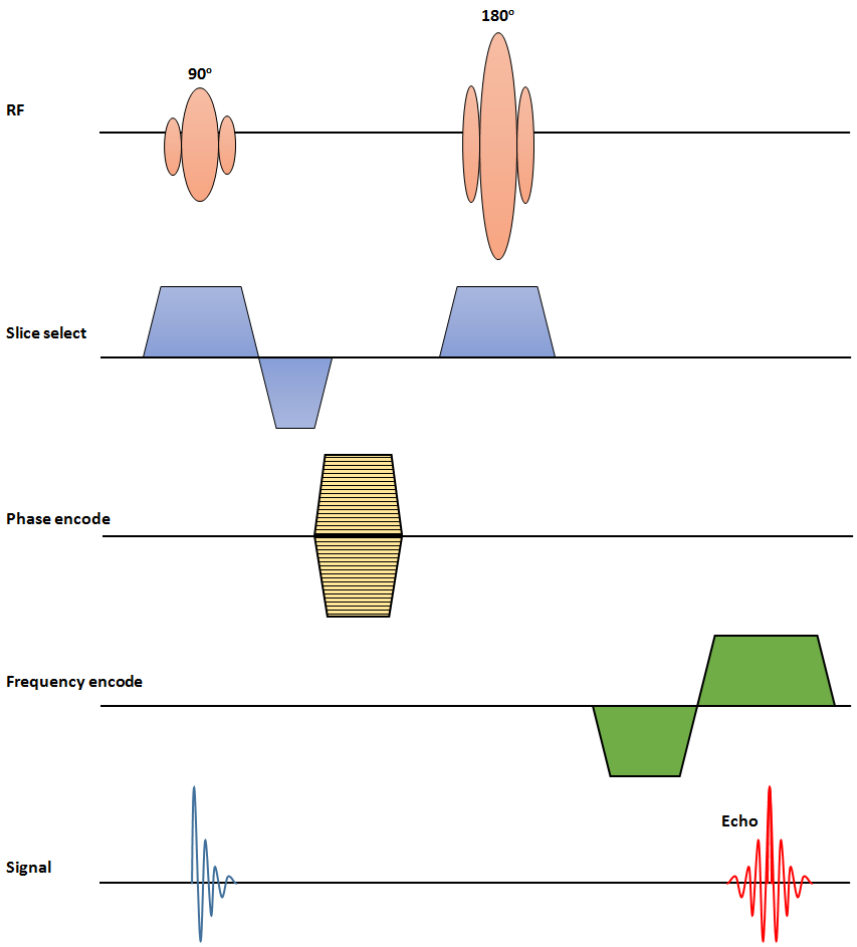

Figure 2.4: Schematic of a spin echo sequence showing the timing of the RF excitation pulses and the application of the gradients.

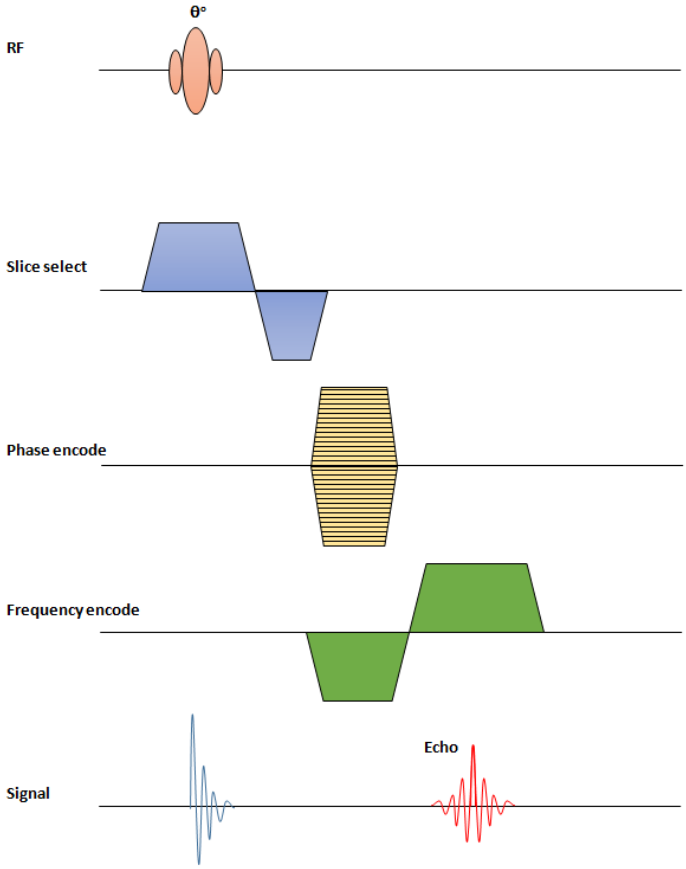

Figure 2.5: Schematic of a gradient echo sequence showing the timing of the RF excitation pulses and the application of the gradients. θ represents the variable angle at which the RF pulse is applied.

2.4 MRI distortion

Due to the modality's strong dependence on the main magnetic field and the gradient fields, any imperfections in the performance of these results in distortions and artifacts in the images. Geometric distortions can arise from systematic issues from the scanner, as well as from the presence of an object within the scanner [35].

2.4.1 Systematic distortions

System related distortions arise from variations of the scanner specifications. The two main sources of systematic distortions arise from inhomogeneities in the B_0 field and nonlinearities in the gradient coils. The B_0 field in combination with the gradient field enable localization of the signal from within the scanner. The homogeneity and linearity of the field and coils deteriorate with increasing distance from the isocenter of the scanner.

1. **B_0 inhomogeneities**

   MRI scanners operate on the assumption that the B_0 field is homogeneous. The homogeneity of the B_0 field is measured in parts per million (ppm) over a Diameter of Spherical Volume (DSV) extending out from the scanner isocenter. Homogeneity values for current scanners are typically 1.1 ppm across a 50 cm DSV. For a 1.5 T scanner, this corresponds to a frequency offset of 70.2 Hz. For an image acquired with a pixel size of 1 mm x 1mm and an imaging BW of 220 Hz/pixel, this equates to a geometric shift of 0.32 mm. Such variations in homogeneity creates discrepancies in signal location and result in intensity variations and distortions within acquired images.

   Modern scanners allow for shimming of the B_0 field, to improve uniformity in the sensitive central volume of the scanner.

2. **Gradient non-linearities**

   When acquiring images, MRI systems assume that the gradient coils have a linear response. Since the performance of these coils is fundamental to the localisation of signal (see Section 2.3), any nonlinearities create variations in signal location between where it originates within the scanner to where the system perceives it to be (Figure 2.6). Hence, the result is a geometrically distorted image.

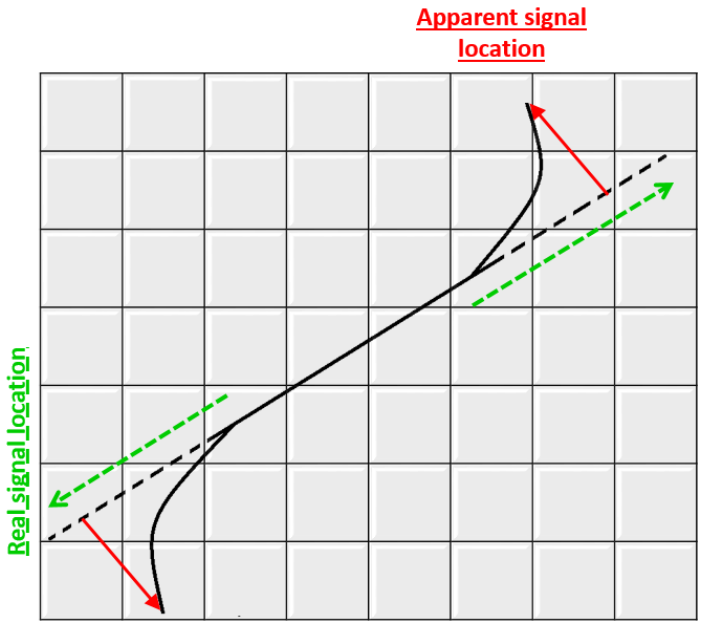

Figure 2.6: Mismapping of voxels due to non-linear gradients. The apparent signal location varies from the actual signal location within the patient.

General specifications for scanner body gradient coils on diagnostic systems is for the gradient error to be less than 2% of the gradient strength over a 40 cm DSV [36]. Performance specifications of additional gradient coil inserts which may be utilised in some situations are characteristically less than this, which can lead to increased nonlinearity effects [37].

To reduce the distortions associated with gradient non-linearities, most vendors now supply correction algorithms (in 2D and/or 3D) which can be applied on or off line. While these algorithms provide a reduction in the geometric distortions present, they are not completely eradicated [38, 39].

Improvements in technology with the shimming and correction algorithm options has seen a reduction in the magnitude of geometric distortions. However the practicality of obtaining a perfectly homogeneous B_0 field and linear gradients remains challenging. Wider, shorter bore designs in modern clinical MRI scanners to improve patient comfort [40] and increasing the magnetic field strength to allow for faster imaging with improved imaging quality makes the optimisation of scanners more challenging [3].

Traditionally, scanners have been optimised to perform best within a spherical volume. Recent design developments have seen a move towards cylindrically optimised magnets to account for the changing scanner designs and to ensure the optimisation is more suited to the imaging volume over the patient anatomy [41].

Each scanner has its own characteristic uniformity and linearity distortions.

2.4.2 Patient induced distortions

When placed within a MRI scanner, patients introduce additional imperfections in the homogeneity of the B_0 field.

1. **Chemical shift**

   Chemical shift arises from differences in the chemical structure of the nuclei of water and fat molecules. Fat molecules consist of a carbon-hydrogen structure whilst water has a oxygen-hydrogen molecular structure. This results in a variation of the resonant frequencies of these two molecules, with fat precessing at a slower rate than water. This chemical shift equates to a magnetic field variation of 3.5 ppm [3]. Chemical shift results in tissues containing fat molecules to be shifted in the frequency encode direction of the image.

2. **Magnetic susceptibility**

   Magnetic susceptibility arises from variations in the magnetisation properties of different tissue types within the body. When a patient (or another irregular object) is introduced into the scanner, the tissues become magnetised by varying degrees and a field opposing the applied field is induced (i.e. a demagnetising field). The overall field then varies throughout the patient volume (due to differences in tissue structures throughout the anatomy) and can be determined by the sum of the applied and demagnetising fields. Susceptibility artefacts are largest at air-tissue interfaces where the difference in magnetisation properties are greatest.

   The variation in magnetic field creates geometric distortions and can produce signal voids within the image. Distortion magnitude due to susceptibility in a cylindrical bore with a parallel field can be defined by:

$$\Delta x = \Delta\chi B_0 / G_F \tag{2.4}$$

Where Δx is the positional error, $\Delta\chi$ is the difference in magnetic susceptibility, B_0 is the main magnetic field strength and G_F is the gradient strength in the frequency encode direction [42]. Field perturbations can be larger than that observed with chemical shift, with perturbations of between -5 to 6 ppm being reported for head and neck [3] with the potential for variations as great as $\pm$ 9 ppm [42]. Susceptibility affects are most prevalent in the frequency encoding direction of images.

Patient induced distortions are dependent on the field strength of the scanner. The difference between the resonance of fat and water increases with field strength. Similarly, the positional errors resulting from susceptibility variations between different tissues also increase with field strength. Therefore the patient induced distortions are larger in magnitude at higher field strengths than at a lower field strengths [35].

2.4.3 Managing MRI system distortions

The American Association of Physicists in Medicine (AAPM) report 100 for MRI quality assurance (QA) [43] recommends the geometric accuracy of clinical MRI scanners be quantified. A common method for characterising MRI geometric distortions is to obtain phantom images with a known geometry and compare the apparent position of phantom structures within the MR image to the known structure locations in order to create a distortion map across the FOV.

While commercial phantoms have been available for distortion measurements, they have previously been limited in size. This is useful when investigating the distortions across a small FOV such as the brain [44, 45]. However when characterising distortion for a full FOV which would be required for a more widespread implementation of MRI in RTP, these phantoms do not cover the required area.

Many studies have developed their own phantoms in order to characterise larger FOV distortions for radiotherapy. One of the earliest to do this was Bakker in 1992 where a rectangular grid phantom consisting of tubes filled with sodium chloride or hydrogen sulphate was imaged on MRI [46]. Distortion magnitude was quantified by comparing the apparent grid point locations from each tube with the known positions.

A number of studies utilise phantoms with liquid filled tubes surrounded by air to test for

geometric distortions. The study conducted by Karger et al. investigated distortions within the head, hence the phantom dimensions were limited to 23 cm length and 18 cm diameter. Within this volume, they observed maximum distortions of 1.2 mm to 5.8 mm over 4 different scanners (mean: 1.0 mm to 4.6 mm) [47]. In a study by Tanner et al., a tube-based linearity test object was utilised to quantify distortions over a larger FOV, with maximum distortions of 16 mm observed in a volume corresponding to that required for whole pelvic imaging [48].

Grid based phantoms designs are common for MRI distortion quantification. Crijns et al. used a plastic box with a rectangular grid insert, surrounded with water [49]. The maximum distortions observed were 2.9 mm, however this was only across the small phantom volume of 150 mm x 150 mm x 30 mm. Grid phantoms designed to determine geometric distortions for the purposes of RTP consist of multiple grid sheets layered in 3D within a box. The box is then filled with a liquid solution, with the grid material producing no signal on MRI resulting in visual control points from which the apparent point locations can be compared to the known grid geometry. Wang et al. used such a phantom with external dimensions of 310 mm x 310 mm x 310 mm [38, 50]. Within a 240 mm x 240 mm x 240 mm cube, maximum distortion across four different scanners were found to range from 4.8 mm to 11.4 mm without vendor correction algorithms applied and 3.4 mm to 9.6 mm with vendor corrections applied. Baldwin et al. investigated the distortions within a 300 mm x 300 mm x 300 mm phantom [40] and with the same phantom again but with additional lateral phantom extensions to cover the entire magnet bore (578 mm) [51]. Over an imaging volume of 260 mm x 265 mm x 87 mm, peak-to-peak distortions were 5.4 mm, 5.0 mm and 1.6 mm (x, y and z respectively). These values nearly doubled to 10.6 mm, 9.8 mm and 3.1 mm when measured over a larger imaging volume (440 mm x 265 mm x 87 mm) .

Studies by Mizowaki et al. [52], Viard et al. [53] and Mah et al. [39] characterise the geometric distortions observed on open-bore systems. Mizowaki at al. and Viard et al. investigated scanners with a field strength of 0.2 T. Within the central FOV region (<100 mm), the maximum distortions observed were below 4 mm. Maximum distortions observed were up to 15 mm within a 350 mm FOV (Mizowaki et al.) and 18 mm within a 190 mm radial distance from scanner isocentre (Viard et al.). These were largest at the outer edges of the FOV and no vendor supplied correction algorithms were applied. The study conducted by Mah et al. investigated the systematic distortions on a 0.23 T scanner with post-processing distortion correction provided by the manufacturer. They observed reduced

distortions compared to the previous two studies as a result of this correction, with maximum distortions below 10 mm within a radial distance of 200 mm from scanner isocentre. Beyond a radial distance of 200 mm, maximum distortions were observed to be > 40 mm without correction which was reduced to 30 mm with correction.

In radiotherapy, the treatment planning process and treatment QA require a geometric accuracy of within 2 mm [54]. Hence, comprehensive distortion mapping of each system is recommended to determine the tolerances and constraints to minimise MRI distortion impact for RTP or provide data for a correction scheme where appropriate.

A theoretical approach to correct for systematic distortions involves applying spherical harmonic deconvolution methods [55]. This method is the basis for the correction algorithms utilised on some commercial scanners and also includes a correction for intensity variations induced by these distortions [47]. Distortions greater than 2 mm may need to be corrected for to ensure radiotherapy treatment dose map accuracy [47, 49]. Whilst vendor supplied correction algorithms reduce geometric distortions, they do not completely remove them. As such, off-line corrections can be performed on images after they are acquired with developed correction techniques.

Distortion maps generated during the quantification of systematic distortion can be utilised to correct for geometric distortions off-line [40, 47, 49–51, 56–61]. Another approach combines phantom measurements and field-derived methods for quantifying and correcting distortions by measuring points along a restricted boundary and utilising spherical harmonics to determine the magnitude of distortions. This combination has been found to give results comparable to that of 3D grid phantom correction based methods [62].

Studies have also been performed to quantify and reduce geometric distortions resulting from the presence of the patient within the magnetic field and the associated chemical shift and susceptibility artefacts [63–65].

While these are viable correction techniques, they can be time consuming, may require a lot of computing power and involve the manipulation of the images. Unfamiliarity with MRI within a radiotherapy department may result in misunderstanding of the potential implications that distortions may have on the treatment planning process. After the application of vendor correction algorithms, residual distortions are still present and could impact the

accuracy of the generated treatment if these distortions are not quantified and if large in magnitude, left unaccounted for.

2.5 Role of MRI in radiotherapy treatment planning

The utilisation of MRI in the radiotherapy treatment planning process has increased significantly over the last few decades. Okamoto et al. began investigating MRI scanners dedicated to radiotherapy as early as 1993 [66]. Since then, many more centres have investigated the utilisation of dedicated MRI scanners for RTP [39, 67–70]. Dedicated MRI scanners within the radiotherapy departments enables MRI-simulation of the patient in the same way they would in CT. It streamlines the workflow, with patients able to be imaged with minimal movement between modalities.

Several questions can be asked when considering utilising a dedicated MRI scanner for radiotherapy. These include:

(i) An open or closed bore scanner?

Devic summarises the benefits and limitations of open and closed bore systems for RTP utilisation [71]. This summary suggests that an open bore configuration is the ideal choice for MR imaging for RTP due to advantages in patient positioning and a more uniform magnetic field. A limitation of such systems is the associated lower magnetic field strength (see following point). Liney et al. highlight the recent development of closed bore systems, making them a more viable option, with wider bore designs, improved homogeneity and dedicated radiotherapy equipment [3].

(ii) A high or low field strength scanner?

There are benefits to high and low field scanners. Open bore scanners generally operate at lower field strengths (0.5 - 1 T), with the closed bore systems generally operating at higher field strengths (1.5 - 3 T). Susceptibility and chemical shift artefacts are more pronounced at higher field strengths (Section 2.4.2) and the higher the field strength (namely 3 T), the risk of heating increases. However SNR increases in a linear fashion with increasing field strength, allowing for improved soft tissue contrast and potential improvements in delineation for the higher strength systems. Associated decreases in scan times also reduces patient movement [20]. Imaging options including frequency

selective fat suppression and MR spectroscopy have better performance on 3 T scanners than lower strength systems [3]. The ideal field strength remains unknown, with both low [39, 67, 70, 72, 73] and high [3, 25, 27, 69, 74–77] field options for MRI simulation being pursued.

(iii) CT/MRI workflow or MRI-only workflow?

The benefits and limitations of each workflow are highlighted in Table 2.1 and summarised in more detail in the sections below.

Table 2.1: Limitations of CT-MRI and MRI-only radiotherapy treatment planning workflows.

Workflow	*Benefits*	*Limitations*
CT-MRI	Contains electron density information	Ionising radiation delivered to patient during imaging
	Short image acquisition time	Time/movement of patient between scans
	Geometrically accurate	Image registration required
MRI-only	Superior soft tissue information	No electron density information
	Streamlined workflow	Longer image acquisition time
	No multi-modality image registration errors	Uncorrected geometric distortions still present in planning image

2.5.1 Utilisation of MRI in a CT-based treatment planning work-flow

As well as geometric distortions, the lack of electron density information in MR images has been a limiting factor in the widespread use of MRI for RTP. This is a key motivation behind a combined CT-MRI workflow for treatment planning.

In a CT-MRI workflow, patient images are acquired on both modalities. The MRI provides the superior soft tissue information beneficial for improved tumour and OAR delineation [2]. The CT provides the geometric gold standard representation of the patient anatomy without the distortions and intensity variations associated with MRI and provides the electron density information required for treatment planning dose calculations. The MRI and any delineated structures are then registered to the primary CT dataset after image acquisition

[78].

There are a number of different techniques that can be utilised for registering MRI and CT images. These include manual, point-based, surface matching, chamfer matching and feature-based registration techniques [35, 79]. A study by Dean et al. investigated the co-registration accuracy of four CT-MRI registration techniques in patients with rectal cancer [80]. They found that an automated registration technique performed the best, with the results being able to be utilised in a radiotherapy workflow for prone rectal patient, with an accuracy of within 2 mm. It should be noted however that these images are registered by rigid body techniques, hence the MRI geometric distortions are still present and require consideration.

Image acquisition and patient positioning are crucial to the CT-MRI workflow [81]. Adequate immobilisation devices are required to ensure that the patient is in a reproducible position, both for the image registration and treatment stages. Additionally acquisition protocols should be selected to ensure that there is no detrimental effect to the image registration process (e.g. adequate pixel bandwidth to ensure that the susceptibility and chemical shift effects are minimised).

If acquiring only MRIs for the planning process, the associated acquisition time could be a limitation. MRI-only simulation would be more time consuming than that of conventional CT simulation. If integrating MR images into a CT based workflow, the MR simulation time could be reduced by acquiring large low-resolution images to obtain the overall anatomical locations, followed by higher-resolution small FOV images, focusing on the anatomy of interest for treatment [71]. The MRI and any associated anatomical contours delineated can then be registered to the whole patient CT [82]. The combined structures from CT and MRI can then be utilised in the planning process on the patient CT. Scanning at a smaller FOV in the centre of the scanner also minimises the distortions that would be observed in the image, particularly at the patient surface, which is further from the isocentre and prone to larger geometric uncertainties.

Paulson et al. [83] conducted a large study over eight anatomical sites with a CT-MRI workflow. At least one large FOV scan was acquired for the purposes of MR to CT registration via a six degree-of-freedom rigid body registration. This methodology incorporated strategies appropriate for incorporating MR into CT-based RTP. While they see the possibility

of having radiation oncology and diagnostic imaging work together to obtain the required images, they highlight the advantages of having an MRI-simulator in the radiation oncology department, even for a combined CT-MR RTP workflow. These include the ability to schedule patient MRI simulation at the same time as CT, without large periods of time in between and transportation of both the patient and any immobilisation equipment required.

2.5.2 Utilisation of MRI in a MR-only treatment planning work-flow

With the improved image quality of MRI, there is a push to remove CT from the planning process altogether. This would streamline the RTP process for the patient, remove image registration errors and reduce the ionising radiation delivered to the normal tissues from simulation and verification imaging.

A number of groups have investigated ways of overcoming the lack of electron density information in MR images to make MRI a viable stand-alone imaging modality for RTP. Since the MRI can't define density in the same way as CT, this information has to be assigned (often referred to as substitute CT (s-CT) or pseudo-CT). One method involves manual or automatic segmentation of images after which a uniform bulk-density is assigned to a given segmented region [84–88]. These studies found the differences between bulk-density assigned and CT electron density information to be clinically insignificant for the anatomical sites they investigated.

Other methods have been investigated to minimise potential errors due to inter-observer variability and auto-segmentation errors. Dowling et al. have investigated atlas-based methods, where patient MR images are averaged to generate an atlas image and matching organ labels which can be utilised to segment a new patient MR image [89]. A corresponding CT atlas can then be generated and the appropriate electron density information be assigned. Other studies have investigated an intensity-based approach whereby the tissues are characterised by their intensity in the acquired images [90]. Gudur et al. developed a method to derive electron density information combining both intensity and geometry information from T1-weighted MR images using a unified Bayesian method in which two conditional probability density functions of electron densities are calculated for each voxel [91]. Since bone has a short T2 relaxation time relative to the other soft tissue structures, studies into image acquisitions with ultra-short echo times (UTE) are being studied in order to be able to segment bone for the RTP process [70, 90].

Nyholm et al. investigated the uncertainties in both CT-MRI and MRI-only workflows for prostate RTP [92]. The study concluded that a MR-only workflow was the most ideal, with systematic uncertainties larger for the CT-MR methodology due to the associated systematic errors throughout the treatment process introduced by the multi-modality image registration. In a study conducted by Stanescu et al., a comparison was performed between CT-MRI and MRI-only based treatment planning [93]. The results showed that the MRI-only methodology implemented performed similarly to the CT-MRI workflow and was a viable option for treatment planning of the brain. This methodology included a correction of MRI distortions, automatic segmentation of pre-defined structures and the assignment of bulk densities to provide the CT information required for dose planning calculations.

2.5.3 Utilisation of MRI for radiotherapy image guidance

Image guided radiotherapy (IGRT) is common place in radiotherapy departments. Verifying the patient setup and variations due to tumour growth or reduction during treatment are crucial for ensuring accurate treatment delivery. If MRI is to be the primary imaging modality for RTP, MRI guidance systems would be a requirement [27]. The required technology has come a long way and continues to develop in order to achieve this [26].

There are several systems available for MRI-guided radiotherapy. Jaffray et al. have developed an MRI guidance facility based on a MRI on rails system with a 1.5 T scanner and a separate linear accelerator [21]. The ViewRay system is a commercially available system, integrating a 0.35 T MRI scanner with a Cobalt-60 radiation treatment unit [22].

Several systems are being developed incorporating a MRI scanner and a linear accelerator into one system. Lagendijk et al. are developing a fully integrated 1.5 T MRI scanner with a 6MV linac [25, 94]. Fallone et al. are investigating a rotating system combining a 0.6 T MRI scanner and a 6MV linac waveguide placed either perpendicular or parallel to the magnetic field [23, 95]. Keall et al. are proposing the combination of 1 T open bore MRI with a 6MV linac inline or perpendicular to the magnetic field with 3 different configurations: 1) fixed beam/horizontal rotating patient; 2) fixed beam/sitting or standing rotating patient; and 3) rotating beam and magnet [24].

As patients undergo radiotherapy, their bodies respond and change throughout the course of treatment. Changes in tumour volume size, daily organ shifts and/or patient weight are

examples of where differences in the simulated and daily anatomical geometry can have a profound impact on the patients treatment. Improvements in image guidance technology, such as these MRI-linac systems will allow for the individualised treatment adaptation throughout the course of radiotherapy, to ultimately improve the outcome for the patient [27].

MRI can also enable the monitoring of tumour response throughout the course of a patients treatment [20, 29–31]. This is beneficial in determining how to proceed with the treatment, if the tumour is well responding to the radiotherapy, or when response is poor modifying the course of treatment accordingly. Diffusion weighted imaging (DWI) is an imaging technique which can be used for this purpose, monitoring the tissue-water mobility between tumours and normal tissues (where tumours will exhibit larger restrictions in the motion of water molecules due to the high cellularity of the tumour volume) [96].

2.6 Impact of MRI distortion in radiotherapy

Investigations into the dosimetric impact of MRI geometric distortions in RTP have focused primarily on brain and prostate patients. For these sites, under the specified study conditions, MR distortions were not found to have a significant impact on dosimetry. Since the brain is located in a small FOV at the centre of the scanner, the observed distortions are minimal and gives dosimetric results similar to that obtained with CT treatment plan generation [32, 76, 97]. The prostate studies were conducted on low magnetic field strength scanners [73, 98], with no corresponding patient CT data over a small cohort [99], or on phantom geometry [77].

These studies previously investigated represent anatomical sites which the target and organ at risk volumes lie predominately in the central regions of the FOV where geometric distortions should be at a minimum. Anatomical sites in which the treatment volume lies in regions of higher geometric distortions (further away from the isocenter of the scanner) could potentially have a more significant impact on the treatment planning process.

The breast represents an anatomical location which lies further from the isocentre of the MRI scanner and may be subject to larger geometric distortions. Prott et al. [100] suggest that geometric accuracy implications for RTP of anatomical sites further from the scanner

isocentre including the breast, be investigated in greater detail. Based on their virtual planning study, Prott also emphasises that variations in dose between planned and treated dose distributions to OAR structures indicate that distortions should be evaluated on a patient specific basis. Breast radiotherapy treatment planning will be investigated in this thesis.

Chapter 3

Quantifying MRI distortion with a 2D distortion phantom

3.1 Introduction

There is a growing interest in utilising MRI for radiotherapy treatment planning (RTP). One of the main reasons for this is the superior soft tissue information that MRI can provide, improving the differentiation between various soft tissue structures and increased accuracy in volume delineation [2, 98]. One of the potential issues in the radiotherapy community impacting on the more widespread uptake of MRI for RTP is geometric distortion within the image [32]. Changing the geometric integrity of the patient anatomy has the potential to affect the precision of beam targeting and dose calculations within radiotherapy treatment planning systems. This has the potential to result in variations in clinical outcomes. These distortions are caused by both system specific and patient related factors.

System specific distortions result from variations in the homogeneity of the main magnetic field (B_0) and the nonlinearities of the gradient fields within the scanner (see Section 2.4). Altering parameters in the image protocol alters the dependence of the acquisition on the gradient coils, altering the distortion present in the image, based on the imperfections in these features. The effects resulting from these intrinsic scanner components alone are reproducible for the same scan protocols, whilst varying between scanners due to variations in system specifications and performance [40].

[1]Part of this chapter has been published:
Walker A, Liney G, Metcalfe P, Holloway L. MRI distortion: considerations for MRI based radiotherapy treatment planning. *Australian College of Physical Scientists and Engineers in Medicine* 2014; 37(1):103-113

The gradient coils allow for the localisation of a signal from within the body, enabling the anatomy to be visualised. Images are constructed on the premise that these gradients are linear and there is a homogeneous main magnetic field (B_0). In modern scanners there is a trade-off in gradient linearity to allow for utilisation of fast imaging sequences and stronger gradient strengths. Whilst such advances can reduce the effects of patient movement and increase patient comfort, the geometric distortions may be greater due to these gradient nonlinearities. This causes a mismapping of pixels, affecting the geometrical integrity of the resulting image. General specifications for scanner body gradient coils are that the gradient error should be less than 2% the gradient strength over a 40 cm diameter of spherical volume (DSV)[37]. Performance specifications of additional gradient coil inserts are characteristically less than this, which can lead to increased nonlinearity effects [37].

The B_0 field homogeneity is another system property which can alter the distortion present in images. Main field homogeneity is measured in parts per million (ppm) over a DSV extending out from the scanner isocentre. Homogeneity values for current scanners are typically 1.1 ppm across a 50 cm DSV. For a 1.5 T scanner, this corresponds to a frequency offset of 70.2 Hz. For an image acquired with a pixel size of 1 mm x 1mm and an imaging BW of 220 Hz/pixel, this equates to a geometric shift of 0.32 mm. Such homogeneity variations can create discrepancies in signal location and manifest as image intensity variations and residual distortions within the image.

There have been a number of different methods proposed for dealing with nonlinear gradient distortions for use in RTP. Many of these methods are based on obtaining phantom images with a known geometry and comparing the apparent position of structures within the MR image to the known point locations to create a distortion map across the field of view (FOV) [49, 50, 52, 58, 101]. After this, post-processing can be conducted in order to correct for the residual distortion based on these maps with the aim to reduce distortions below 2 mm. Distortions greater than this may need to be corrected for to meet the tolerance limits for imaging in radiotherapy [54], in order to ensure accurate radiotherapy treatment [47, 49]. Any residual distortions would need to be considered when determining planning volumes to ensure that the target volume is covered [102]. This would depend on the location of the anatomical site and the magnitude of the distortions observed within that region of the scanner.

A more theoretical approach can be utilised by applying spherical harmonic deconvolution

methods to correct for distortions within a specific device's FOV [55]. This method is the basis for the correction algorithms utilised on some commercial scanners and also includes a density correction for intensity variations caused by these distortions [47].

While distortions are unwanted in any image, their impact is dependent on how the images are utilised. This chapter evaluates geometrical inaccuracy with respect to the application of images for RTP purposes. A number of studies have investigated the geometric accuracy of clinical MRI scanners for the purposes of RTP [39, 49, 103, 104]. Previous studies of MRI distortion investigating the use of MRI for radiotherapy for a number of anatomical sites have focused on one specific acquisition sequence [40, 46, 49–51, 58, 60, 73, 101]. These studies were also focused on anatomical locations which would be placed close to the centre of the scanner such as the prostate [49, 73, 98], head and neck [47, 64, 76] as well as stereotactic radiosurgery applications [45].

In this study, images of a test phantom were obtained in one imaging plane using a number of different clinical MRI protocols with varying selection parameters. Four MRI scanners from different centres were investigated. Differences in magnitude and direction of the distortion between scanners and imaging protocols were assessed. This data was then compared to the location of anatomical sites which may be of interest when considering the use of MRI in RTP. This study also investigated the effects of varying bandwidth (BW) on distortion and the signal-to-noise ratio (SNR). By acquiring images at two different bandwidths it was also possible to estimate the homogeneity using the method described by Chen et al. [105]. This study only considered distortions from systematic factors. Patient related distortions were not addressed.

3.2 Method

3.2.1 Phantom

To determine the distortion magnitude and pattern, MR images of a FLUKE Biomedical phantom were acquired (Figure 3.1). This commercially developed phantom conforms to the specifications as outlined in the AAPM nuclear magnetic resonance task group number 1 [106]. It is designed to enable the testing of uniformity and linearity of MRI scanners. The acrylic phantom has outer dimensions of 330 mm x 330 mm x 102 mm, with the grid region

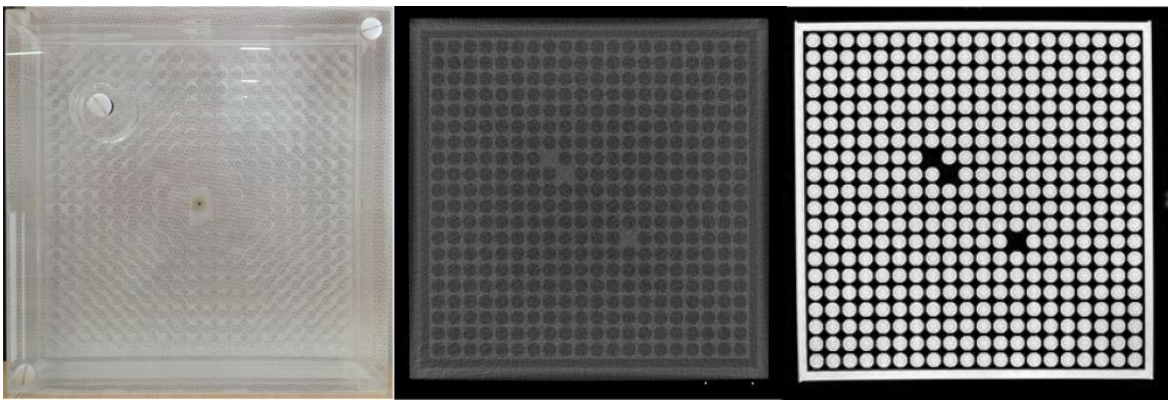

Figure 3.1: From left to right: the phantom used for this study, CT scan of the phantom and a turbo spin echo image of the phantom.

of dimensions 277 mm x 277 mm x 25 mm. Contained within this were 397 cylindrical grid points in a 20 x 20 2D grid layout, with three points removed for consistent orientation and alignment. The spacing between the axial centres of each grid point is approximately 15 mm, with each grid point having a diameter of 12 mm. The grid points were created by systematically placed holes milled into the acrylic structure. The holes were filled with saline to create the 2D grid pattern. The centre of the phantom was aligned in the horizontal direction to the centre of the scanner. The vertical position of the phantom was determined by the fixed couch height of each scanner.

3.2.2 Phantom imaging procedures

CT

A CT scan of the phantom was undertaken on a Siemens SOMATOM Sensation scanner. This was taken to be the 'gold standard' scan, assumed to have negligible distortion for determining the grid point locations. Scan parameters included a FOV of 500 mm, 512 x 512 matrix (spatial resolution 0.98 mm) and a slice thickness of 2 mm.

MRI

Measurements were made on four clinical MRI scanners, a 60 cm bore Intera Achieva Nova Dual 1.5 T (Philips Medical Systems, The Netherlands), a 60 cm bore MAGNETOM® Symphony Syngo 1.5 T, a 70 cm bore MAGNETOM® Verio 3 T and a 70 cm bore MAGNETOM®

Skyra 3 T (Siemens Medical Systems, Erlangen, Germany). A number of sequences were investigated based on their clinical applications for radiotherapy treatment planning. Table 3.1 shows the acquisition details for each of these sequences. The sequences were matched as closely as possible on the different MRI scanners for comparative purposes.

To ensure set-up reproducibility on different scanners, round MRI compatible multi-modality markers were fixed to the sides of the phantom and the laser system on the scanners used to align these markers to the scanner isocentre. Analysis of both CT and MR images were conducted on the axial image slice corresponding to the centre of the scanner and the central region of the phantoms grid structure. To overcome the issue of the rounded/padded couch, one of two approaches was taken, depending on the scanner.

For the Siemens 3 T Verio and the Philips 1.5 T scanners, the phantom was placed on a flat Styrofoam board to ensure its stability on the couch. The spine coil was removed on the Siemens 1.5 T Symphony and 3 T Skyra scanners, allowing for stable placement of the phantom as well as creating better alignment between the phantom centre and the scanner isocentre. The position of the phantom with respect to the scanner isocentre was noted so that all distortion measurements could be made with reference to the distance from this point. The vertical position of the phantom was dependent on the couch height.

For both the Siemens 3 T scanners, there was an option in the acquisition setup allowing for application of inbuilt gradient correction algorithms. The 2D algorithms were applied on these scanners, since the phantom design meant that distortion could only effectively be measured within a 2D imaging plane. For comparative purposes on the Siemens Verio 3 T scanner, phantom images were also analysed without the application of the 2D gradient correction algorithm. The images were initially acquired with the algorithm turned on. Once all of the sequences had been acquired and saved, non-corrected images were then obtained through post processing methods, by deselecting the 2D algorithm option in the control panel and re-saving the image sets. The corresponding changes in distortion between the two modes of acquisition could then be determined. Not all scanners had the capability of applying 3D distortion corrections so only the 2D correction algorithms were assessed. Additionally, only a thin section of the phantom in the axial plane at isocenter was analysed and hence the impact of distortion correction in the slice-selection direction was considered to be minimal for these measurements.

Table 3.1: Parameter of the MRI acquisition sequences for which distortion was assessed

Scanner	**Sequence**	**Image weight**	**2D/ 3D**	**TR/TE (ms)**	**FOV (mm)**	**Flip angle (°)**	**Slice thickness (mm)**	**Pixel BW (Hz/pix)**
Philips 1.5 T Intera Achieva[a]	Spoiled GRE	T1	3D	25/4.6	450x450	30	3	131
	Spoiled GRE	T1	2D	2.6/4.6 7.0/4.8	450x450	80	3	1818
	V-Interp GRE	T1	3D	4.3/2.1	450x450	9	4	434
	V-Interp GRE	T1	3D	1500/ 120	450x450	9	4	434
	SS-TSE	T2	2D	2000/ 350.8	450x450	124	4	355
	3D TSE	T2	3D	4012.9/ 100	450x450	120	5	417
	TSE	T2	2D		450x450	90	4	191
Siemens 1.5 T Symphony Syngo[b]	Spoiled GRE	T1	3D	7.2/2.8	450x450	20	1.3	175
	Spoiled GRE	T1	2D	139/ 2.32	450x450	70	4	390
	SS-TSE	T2	2D	1890/ 115	450x450	120	4	115
	3D TSE	T2	3D	1820/ 471	420x420	120	2.5	125
	TSE	T2	2D	4550/ 127	450x450	120	4	85
	TSE	T2	2D	4550/ 127	450x450	120	4	85
	3D SE	T2	3D	9.4/4.8	420x420	20	5	150

Table 3.1: Parameter of the MRI acquisition sequences for which distortion was assessed

Scanner	**Sequence**	**Image weight**	**2D/ 3D**	**TR/TE (ms)**	**FOV (mm)**	**Flip angle (°)**	**Slice thickness (mm)**	**Pixel BW (Hz/pix)**
Siemens 3 T Verio[c]	Spoiled GRE	T1	3D	6.0/2.5	450x450	20	1.3	399
	Spoiled GRE	T1	2D	167/ 2.5	420x420	70	4	279
	V-Interp GRE	T1	3D	4.4/2.5	450x365	9	3	679
	V-Interp GRE	T1	3D	4.6/2.0	450x450	9	2	401
	SS-TSE	T2	2D	1890/ 119	450x450	120	4	507
	3D TSE	T2	3D	1280/ 90	450x450	120	2.5	244
	TSE	T2	2D	5030/ 81	450x450	80	4	228
Siemens 3 T Verio[d]	Spoiled GRE	T1	3D	5.7/2.5	340x340	20	3	390
	Spoiled GRE	T1	2D	90/ 2.5	340x340	70	4	280
	V-Interp GRE	T1	3D	4.2/2.4	380x368	9	3	675
	V-Interp GRE	T1	3D	4.4/2.1	340x340	9	2	400
	V-Interp GRE	T1	3D	4.4/1.2	380x380	9	3	975
	SS-TSE	T2	2D	900/ 87	340x340	120	3	505
	TSE	T2	2D	4780/ 81	340x340	80	3	230

GRE = Gradient Echo; V-interp = Volume interpolated

TSE = Turbo Spin Echo; ss-TSE = Single Shot Turbo Spin Echo

[a] Maximum gradient strength 66 mT/m, slew rate 160 T/m/s

[b] Maximum gradient strength 30 mT/m, slew rate 125 T/m/s

[c] Maximum gradient strength 45 mT/m, slew rate 200 T/m/s

[d] Maximum gradient strength 45 mT/m, slew rate 200 T/m/s

3.2.3 Distortion analysis

MATLAB code was developed in-house and implemented to determine the position of each phantom grid point in the x and y plane. Each image was converted into a binary image by manually altering the threshold value so that all grid points could be differentiated from each other and any noise present in the image. The code was designed to calculate the central positions of each of these points. The distortion for each grid point was expressed as a function of its radial distance from scanner isocentre by comparing the positioning of the centre of the phantom relative to isocentre. Comparisons of distortion magnitude and patterns from isocentre were then undertaken for all sequences and scanners. The distortion magnitude was assessed relative to an assessment criterion of 2 mm. The 2 mm criterion is taken from image accuracy requirements for radiotherapy simulation [43]. Also, the accuracy of the distortion measurement will be limited by the voxel size used to acquire the images, hence 2 mm is a reasonable relative measurement.

3.2.4 Bandwidth Investigation

The effects of changing bandwidth on the distortion and signal to noise ratio (SNR) follow the relationship displayed in equation 3.1:

$$SNR \propto \frac{1}{\sqrt{receiver\ bandwidth}} \propto Distortion \tag{3.1}$$

Scans were conducted on the Siemens 1.5 T MAGNETOM® Symphony Syngo scanner, for both visual and quantitative analysis of this relationship. The acquisition sequence utilised was a standard T1 weighted spin echo with TE = 30 ms, TR = 500 ms, FOV = 340 x 340 mm, slice thickness = 4 mm and echo train length = 1. The impact of varying both the bandwidth and the phase encoding direction was assessed to investigate variations in distortion patterns and magnitudes. The receiver bandwidths investigated were 7.7, 25.6, 51.2, 76.8 kHz and 200 kHz with the readout gradient tested both in the anterior-posterior and right-left directions for each bandwidth value.

The impact on SNR with changing bandwidth was calculated from equation 3.2:

$$SNR = \frac{average\ signal}{std.deviation of background} \tag{3.2}$$

The signal was calculated for each bandwidth by analysing twenty predetermined grid point regions of interest (ROI's) selected across the phantom area. The image noise was also sampled with ROI's of the same size across the background of each image.

3.2.5 Homogeneity assessment

The homogeneity of the scanners B_0 field is another system property which can alter the distortion present in images. Main field homogeneity is measured in parts per million (ppm) over a DSV extending out from the scanner isocentre. Homogeneity values for current scanners are typically 1.1 ppm across a 50 cm DSV. For a 1.5 T scanner, this corresponds to a frequency offset of 70.2 Hz. Such homogeneity variations can create discrepancies in signal location and manifest as image intensity variations and distortions within the image.

The homogeneity of the central scanner region was assessed across a range of different areas across the central imaging plane of the scanner. Comparisons were made between the differences in distortion values for narrow and wide bandwidth values. This was tested on the Siemens 1.5 T scanner. This was based on the work of Chen et al., utilising the following for expressing H_B [105]:

$$H_{\mathrm{B}}(ppm) = \frac{BW_1 \cdot BW_2 \cdot (x'_1 - x'_2)}{(\gamma/2\pi) \cdot B_0 \cdot FOV \cdot (BW_2 - BW_1)} \tag{3.3}$$

where $\gamma/2\pi$ = 42.576 MHz/T for protons, BW_1 and BW_2 are the bandwidths of the data sets being compared, x_1 and x_2 are the coordinates in the frequency encoding direction of corresponding grid points for each bandwidth, B_0 is the main magnetic field strength and FOV is the field of view. The values were determined for a number of circular areas of varying diameters within the imaging plane.

3.2.6 Anatomical locations

Seven anatomical sites of interest for radiotherapy treatment planning were investigated to determine their common location with respect to the distance from the centre of both 60 cm and 70 cm bore MRI scanners. Contoured radiotherapy CT data sets of the breast, lung, oral cavity, larynx, brain stem, prostate and cervix were obtained for ten patients. In-house MATLAB code was utilised to determine the coordinates of the centre and extent of each

contoured volume in the x and y planes.

The maximum radial distance that each anatomical contour extended from the scanner isocentre was recorded. It should be noted that the head and neck structures were based on CT scans obtained with the clinical radiotherapy set up practised in the department where the region is elevated off the couch top.

3.3 Results

3.3.1 Sequence and scanner distortion comparison

Figures 3.2 and 3.3 compare the distortion distribution for the different sequences and scanners investigated. The average distortion of the markers across the phantom area was less than 2 mm for the sequences tested. An increase in distortions above 2 mm generally occurred as the radial distance from isocentre extended beyond 100 mm. Due to the variations in bore size, the phantom was located closer to the edge of the bore, extending further from the isocentre in the 60 cm bore scanners in comparison to the 70 cm.

3.3.2 Bandwidth analysis

Table 3.2 shows the variation in average and maximum distortion values for the various receiver bandwidth values and the corresponding readout direction. The SNR for bandwidths between 7.68 kHz to 76.8 kHz decreased by a factor of 3.1, (theoretical value = 3.2 for a tenfold increase in BW). Bandwidths greater than 76.8 kHz were not assessed due to the poor signal to noise observed in the images. For a bandwidth of 200 kHz, the SNR was reduced to 3.7, preventing the calculation of grid point locations. The homogeneity of the scanner was less than 0.4 ppm across areas with diameters ranging from 12 cm to 20 cm. On the 1.5 T scanner, a variation of 0.4 ppm in the magnetic field strength accounts for a distortion of 0.85 pixels for a bandwidth of 7.68 kHz. In these images, that equates to 1.13 mm distortion. For a receiver bandwidth of 76.8 kHz, this value is reduced to a distortion of 0.08 pixels (0.11 mm).

Table 3.2: Comparison of the effects on the distortion values measured across the phantom for variations in the receiver bandwidth and phase encoding direction

Bandwidth (kHz)	**Phase encode direction**	**Avg distortion (mm ± SD)**	**Maximum distortion (mm)**	**SNR**
7.7	Ant - Post	2.16 ± 1.66	6.33 ± 0.66	
7.7	Right - Left	2.21 ± 1.48	5.27 ± 0.66	20.01
25.6	Ant - Post	0.80 ± 0.57	3.00 ± 0.66	
25.6	Right - Left	0.68 ± 0.45	2.16 ± 0.66	11.29
51.2	Ant - Post	0.77 ± 0.44	2.23 ± 0.66	
51.2	Right - Left	0.59 ± 0.37	1.96 ± 0.66	7.69
76.8	Ant - Post	0.60 ± 0.36	1.93 ± 0.66	
76.8	Right - Left	0.60 ± 0.37	1.74 ± 0.66	6.54

3.3.3 Vendor 2D corrected vs. non-corrected images

Figure 3.4 shows the variations observed in changes in distortion magnitude and distribution across the phantom area with the application of the 2D correction algorithm for both a spin echo and gradient spin echo sequence. With the correction algorithm, both the average and maximum distortion values were minimised in some areas but were not completely removed. In some regions of the phantom, the distortion actually became worse with the 2D correction algorithm applied as opposed to without. Whilst the average distortions across the phantom area were all reduced to below 1.5 mm with the correction algorithm, the maximum distortions still remained greater than 2 mm, increasing with increasing distance from the isocentre. The performance of the correction algorithm with respect to radial distance from the scanner isocentre is highlighted in table 3.3.3. Figure 3.5 shows a distortion vector map comparing the difference in distortion between the grid point locations as seen with and without the correction algorithm applied. This shows the algorithm is not required to provide much correction for smaller radial distances where distortions were generally found to be below 2 mm.

Table 3.3: Comparison of the variation in mean and average distortions observed for radial distances above and below 100 mm radial distance from the scanner isocenter

Sequence	**Mean distortion Below 100 mm**	**Mean distortion Above 100 mm**	**Max distortion Below 100 mm**	**Max distortion Above 100 mm**
3D TSE				
- Corrected	0.53	1.09	1.32	2.81
- Non Corrected	0.47	1.86	1.19	4.41
3D spoiled GRE				
- Corrected	0.61	1.01	1.68	2.34
- Non Corrected	0.56	2.03	1.37	5.00

3.3.4 Anatomical locations

Figure 3.6 displays the distortion obtained on both Philips and Siemens T2 weighted turbo spin echo sequences with reference to the determined mean locations of the breast, lung, cervix, prostate and head and neck structures relative to the isocentre within a 2D axial imaging plane. The length of each represents the regions where each anatomical feature lies with respect to the centre of the scanner. The breast was the only anatomical structure investigated where the contour did not pass through the scanner isocentre.

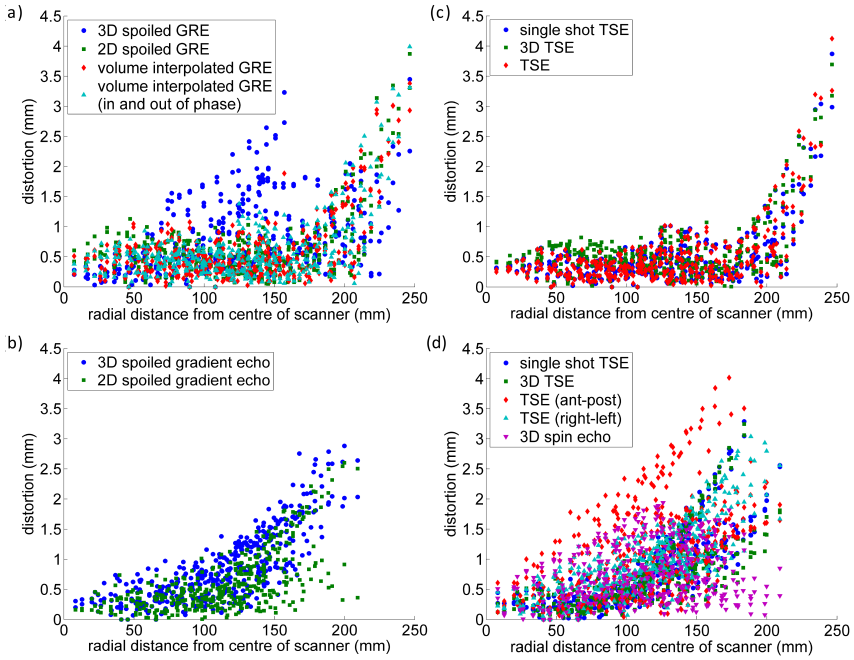

Figure 3.2: Distortion distribution across the phantom area on the 1.5 T scanners for a. Philips Intera gradient echo sequences; b. Siemens Syngo gradient echo sequences; c. Philips Intera spin echo sequences; and d. Siemens Syngo spin echo sequences.

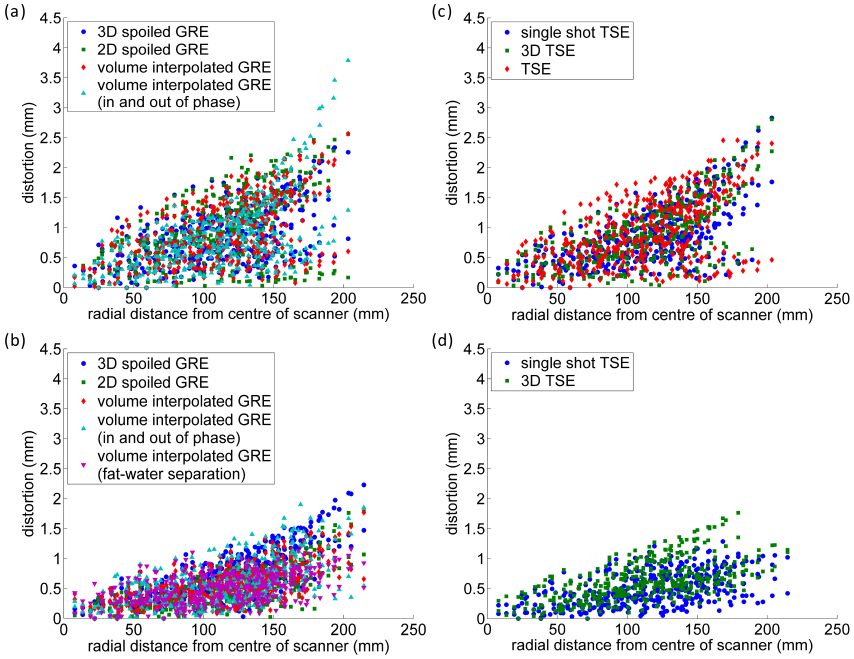

Figure 3.3: Distortion distribution across the phantom area on the 3 T scanners for a. the Siemens Verio gradient echo sequences (2D correction applied); b. Siemens Skyra gradient echo sequences (2D correction applied); c. Siemens Verio spin echo sequences (2D correction applied); and d. Siemens Skyra spin echo sequences (2D correction applied).

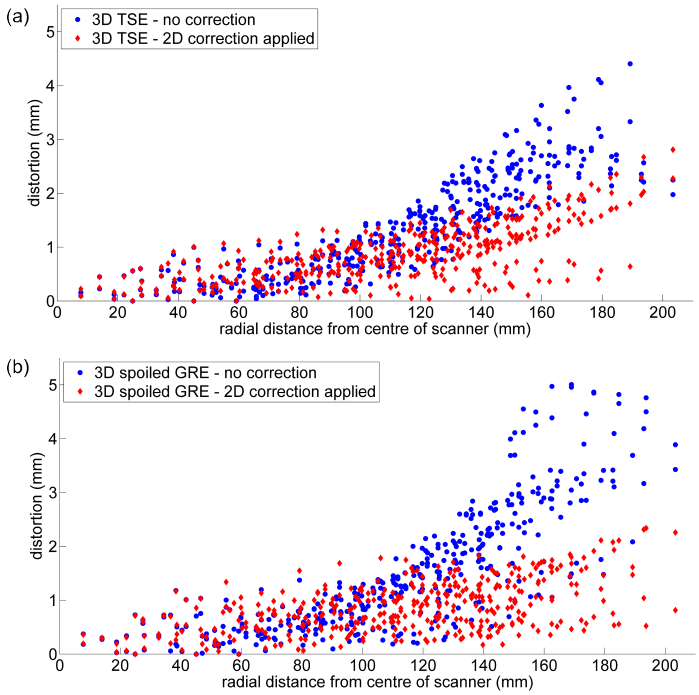

Figure 3.4: Comparison of the distortion distribution across the phantom area with and without the application of the 2D correction for a. 3D turbo spin echo sequence and; b. 3D spoiled gradient echo sequence.

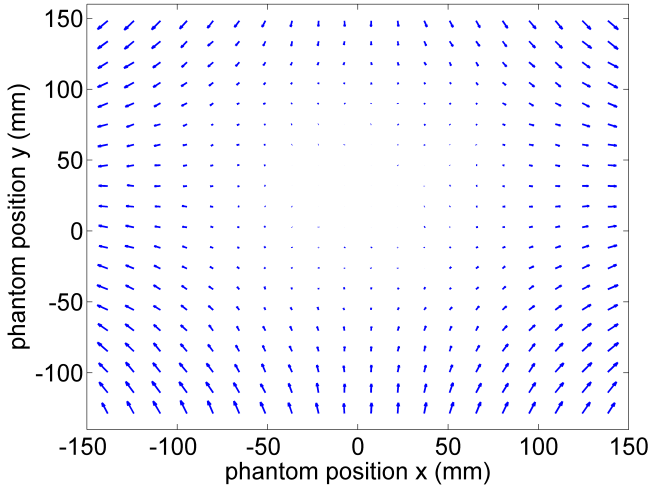

Figure 3.5: Difference between 2D distortion maps of a 2D spoiled gradient echo sequence on a Siemens Verio 3 T scanner with and without the 2D correction algorithm applied.

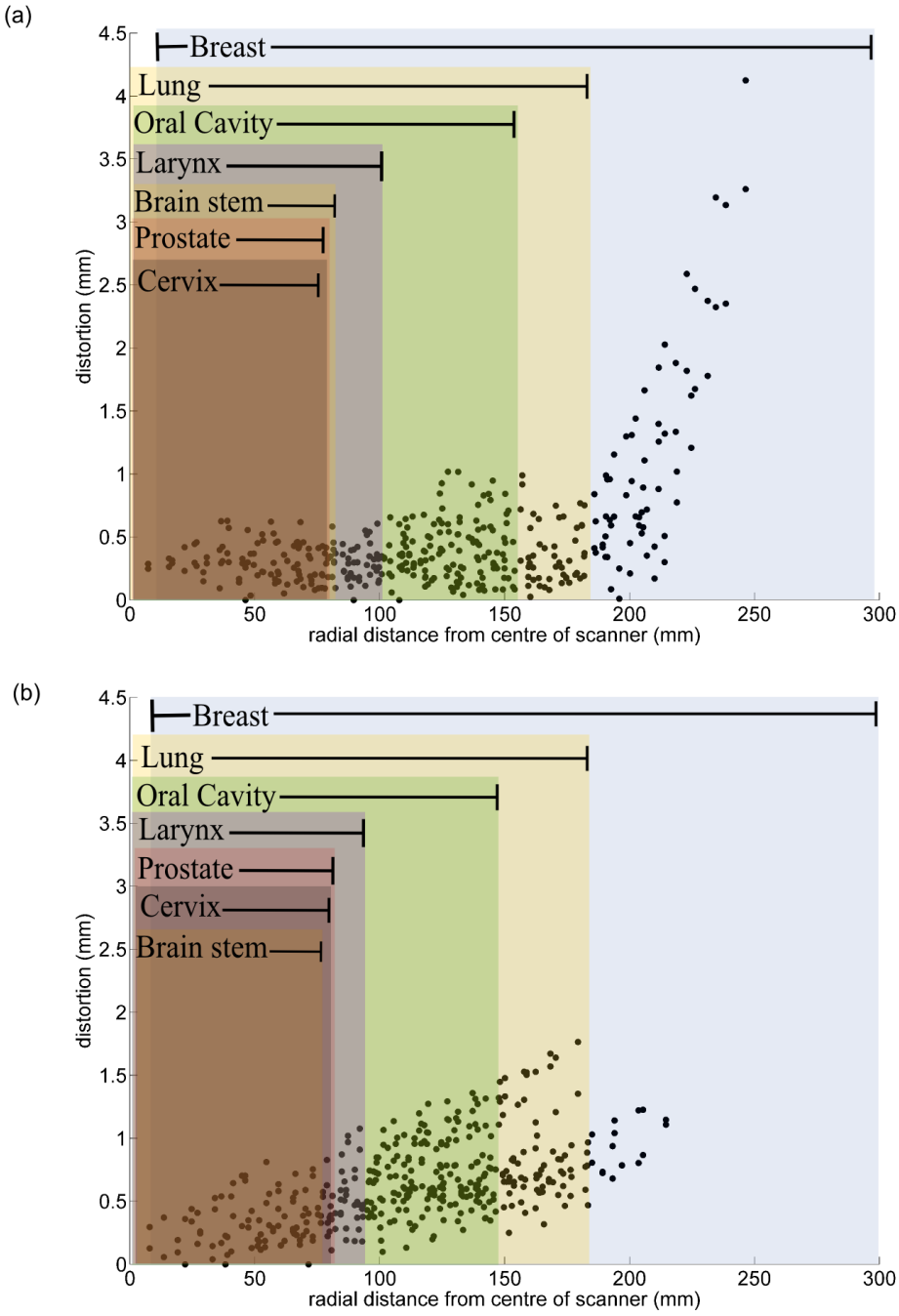

Figure 3.6: The distortion observed from the radial distance from the centre of a. the Philips 1.5 T 60 cm bore scanner with the TSE sequence and; b. the Siemens 3T 70 cm bore Verio scanner. The blocks indicate the corresponding position of anatomical sites within the scanner. Note the scale has been extended out to illustrate where the breast is situated, although distortion measurements were not made beyond a radial distance of 250 mm. NOTE: The height of each box is for display purposes only and does not reflect any information regarding the distortion values.

3.4 Discussion

Each MRI acquisition sequence was demonstrated to be subject to individual distortion patterns as shown in Figs. 3.2 and 3.3. Parameter selection impacts the amount of distortion in an image. Equivalent sequences conducted on different scanners have varying distortion patterns. This is due to the system hardware design specification variations between vendors.

MRI scanners are optimised to exhibit least distortion towards the centre of the scanner, with the homogeneity and gradient linearity deteriorating with increasing radial distance from the centre. In this study, the phantom extended closer to the edge of the bore for the 60 cm bore scanners than those with 70 cm bores, due to the size limitations and fixed couch height. This was one of the reasons for the variations seen in the maximum distortions observed between the 60 and 70 cm bore scanners, all of which are capable of imaging a 50 x 50 cm FOV. This set up was the same as that used for current radiotherapy treatment planning MRI scans.

Receiver bandwidth is one parameter that effects MR image distortion as shown in table 3.2 A tenfold increase in receiver bandwidth saw a reduction in average distortion of more than 1 mm, while maximum distortions were reduced by more than 3 mm. A tenfold increase in this bandwidth resulted in a reduction in SNR by a factor of 3.1. To overcome this reduction in SNR, the number of excitations during the image acquisition could to be increased. This may be a solution for phantom studies however applying this to the acquisition of patient images may not be practical with a resulting increase in total scan time and associated increase in motion artifacts. While smaller receiver bandwidth values result in better SNR, higher bandwidths result in less geometric distortion.

The homogeneity values obtained were based on the calculation method from Chen et al. [105]. The H_B value calculated of < 0.4 ppm across the scanner is consistent with the scanner specifications, which state the homogeneity across a 40 cm DSV is 0.4 ppm with a field stability of < 0.1 ppm/hour. One of the assumptions made in the calculations however, is that the gradients are linear, which is not the case particularly as the DSV increases.

For treatment planning purposes, vendor correction algorithms for gradient nonlinearities should be utilised on scanners with such capabilities in order to take advantage of their in-

built distortion reduction software. Figures 3.4 and 3.5 show the difference in distortion values for images acquired with and without the correction algorithms applied, across the phantom area. It can be observed that in some regions both the magnitude and direction of the distortion is altered with the application of the correction algorithm, though the distortions were not completely removed.

One of the limitations of this study was the phantom utilised due to its shape and size. Firstly, because of the square shape within the cylindrical bore, there was a large region of the scanner, where distortion information could not be assessed. Since some patient anatomy (e.g. breast) may lie beyond this point, the phantom was insufficient for complete distortion analysis for RTP purposes. Secondly, the 2D grid structure only allowed for distortion assessment in one imaging plane. On scanners with distortion correction capabilities, the 2D correction algorithm was applied. Due to the phantoms structure, application of a 3D correction algorithm provided no additional benefit in terms of distortion reduction within the imaging region. The phantom was not rotated within the scanner to obtain 2D distortion data within other imaging planes.

A phantom for testing geometric distortion and field homogeneity would ideally consist of a number of points isolated in known positions in all three image planes, extending out over the entire FOV. This would be more representative of the regions within which the overall patient outline and anatomical regions of interest for RTP would be located. Assessment of patient specific distortions (which have not been investigated in this study) would require the testing of additional anthropomorphic phantoms or patient data sets to determine the consequential variations in the local magnetic field values.

The variation in distortion distribution for clinical imaging sequences as observed in Figures 3.2 and 3.3, demonstrates the importance of knowing the scanner specifications and the protocols used in the imaging process for use in RTP. Considerations should be made as to the possible effect that this may have on contouring uncertainties and dosimetric variations. In a clinical setting, these acquisition parameters are readily changeable in order to obtain an image of required quality for the purposes of planning, however the trade-offs between SNR and distortion values need to be considered. It was assumed for each acquisition sequence, with the same setup that the distortion values were reproducible [107].

The distortion maps in Figures 3.2 and 3.3 can be compared to the position within which

various clinical sites lie with respect to the centre of the scanner (Figure 3.6). Since distortions are largest in the peripheral regions of the scanner, the impact on RTP may be of greater importance for anatomical structures situated in this region. Based on anatomical positioning within the scanner, treatment planning for the lung and breast clinical sites using MR images would have the largest distortion values to be considered. The distortions present in head and neck images would need to be considered, since the oral cavity may be a target volume or organ at risk. Patient contours are fundamental in the treatment planning process for the dose calculations. As such the extent of the patient within the scanner needs consideration. For breast patients, the breast contours also mark the extent of the patient contour. For the prostate and cervix, the overall patient contour can extend beyond a radial distance of 200 mm. For head and neck sites, the region of interest for the patient contour is reduced to below a radial distance of 150 mm from isocentre.

While MRI can be co-registered to the planning CT and incorporated in the RTP workflow [71], there is widespread interest in performing MR-only planning. MRI-only planning has the potential to decrease the ionising radiation exposure to the patient and, if both modalities are being utilised, the patient scan time. Additionally, CT-MRI registration may also introduce errors into the treatment planning process. Assessment of the geometric distortion is one important aspect to investigate when considering the use of MRI alone for planning, to ensure that the planning process and eventual treatment are accurate.

3.5 Conclusion

A baseline assessment of variations in magnitude and distribution of systematic distortions present in MR images was conducted. Differences between sequences and MRI scanners were observed, the largest variations occurring between scanners. These are due to the parameters utilised in the acquisition process (with the largest influences being from the receiver bandwidth selected and the application of vendor supplied correction algorithms) and the specific B_0 and gradient characteristics of each individual scanner. Differences in distortion patterns were observed between acquiring the images with the phase and frequency encoding directions, a observation that will be utilised in investigations discussed in Chapter 5. The selection of imaging protocols and parameters, as well as understanding the scanner geometric limitations is fundamental when considering the use of RTP planning with MRI alone. The magnitude of distortions varies across the imaging FOV such that depending on the clinical site of interest, site specific assessment of the possible clinical impact is important and off-line correction of these distortions investigated if required.

The AAPM report 100 [43] states that comprehensive distortion mapping of each system is recommended to determine the tolerances and constraints to minimise MRI distortion impact for RTP or provide data for a correction scheme where appropriate. While the MRI test 2D phantom utilised gave a good initial indication of the scanners geometric integrity and relative scanner performance, it was not adequate for full distortion assessment as recommended and was limited in the extent to which the distortion could accurately be measured across the whole FOV.

Chapter 4

Development of a 3D distortion phantom

4.1 Introduction

Phantom based measurements are a common method to quantify MRI geometric distortion by comparing the known location of features within the phantom to the apparent location in the MR image. Many commercially developed phantoms are designed to test multiple imaging parameters such as geometric distortion, uniformity, resolution, chemical shift, signal to noise (SNR) and ghosting. As a result, each phantom test element is relatively small. A number of distortion studies have been conducted with such phantoms [44, 45, 55, 108]. Such phantoms are often used for QA of diagnostic MRI scanners, as opposed to that of MRI-simulators used in radiotherapy treatment planning, where higher geometric precision is required. Limitations included the restricted FOV coverage and the number of control point locations at which the distortion can be determined. Several studies have developed their own distortion phantoms, tailored to specific applications [48, 58, 109–111]. It was not always necessary for these studies that a full distortion assessment be performed. For the purposes of RTP investigations many of these phantom designs were unsuitable, often being limited in size, shape and were often plagued by air bubbles and potential susceptibility artifacts where the liquid solution being used met the phantom housing structure.

Chapter 3 highlighted the limitations of a commercial phantom in terms of its ability to adequately determine distortion across all 3 imaging planes and the limited ability to cover

[1] Part of this chapter has been published:
Walker A, Liney G, Holloway L, Dowling J, Rivest-Henault D, Metcalfe P. Continuous table acquisition MRI for radiotherapy treatment planning: distortion assessment with a new extended 3D volumetric phantom. *Medical Physics* 2015; 42(2):1982-1991

the FOV required for imaging the region of the body required for RTP purposes. In such a case, full FOV distortion assessment would involve moving small phantoms around the scanner volume, introducing issues in reproducibility of placement and changes in field inhomogeneities with the changing phantom position. This chapter identifies key phantom characteristics when physically measuring MRI distortion for applications in radiotherapy. Numerous prototypes were investigated before the final phantom design was developed. The new 3D phantom is capable of characterising whole FOV distortions as required for RTP. The design presented is novel due to its extended length and the use of numerous offset vitamin E capsules, rather than rods for the assessment of through-plane distortion.

4.2 Prototype Development

4.2.1 Assessment Criteria

A number of ideas for assessing the geometric distortion in MR images were investigated, with the end result to design a phantom appropriate for the purposes of RTP. Prototypes were developed for this purpose. Each prototype was assessed based on the criteria in table 4.1. All of these ideal criteria needed to be met before the final phantom was developed.

Table 4.1: The criteria required for the phantom development and the associated method of assessment.

Criteria	**Method of Assessment**
MRI compatible	Initial condition was set that any design must be possible without the need for ferromagnetic materials
Grid points localised in 3 dimensions	The coordinates of the grid points needed to be readily defined in all 3 imaging planes in the design stage across the whole phantom area
Full FOV coverage	For radiotherapy, whole patient images usually acquired with x-y FOV 500 x 500 mm with a scan length > 250 mm. The phantom dimensions needed to be capable of such measurements

Table 4.1: The criteria required for the phantom development and the associated method of assessment.

Criteria	Method of Assessment
Practical design	The phantom had to be as lightweight as possible (accounting for the required size), with appropriate methods for handling. It was required to be readily transported between MR and CT for imaging with solid components to avoid any major leaks/spills in trying to contain fluids in the large quantity required
CT AND MRI visualisation	Acquisition of images on CT and/or MRI. Good contrast required on both imaging modalities

Initial prototypes were developed using ideas derived from the literature as well as commercial materials that were readily available in the department. Figure 4.1 shows the prototype development process in arriving at a design solution that met our needs, as specified by the predefined assessment criteria. The final phantom design was developed further based on the prototype designs that had met all of these specified criteria.

4.2.2 Prototypes

1. **Anthropomorphic phantom**

   The thorax and breast sections of an anthropomorphic phantom (CIRS female ATOM dosimetry phantom) (Figure 4.2) were used to investigate the feasibility of utilising a pre-existing radiotherapy department phantom. These phantom components had total cross section dimensions of 20 cm x 25 cm (including the breast attachments). The phantom design included removable plugs (5 mm diameter x 25 mm length) where, when removed, various types of dosimeters can be placed throughout. Gelatine, wax candles, lard, a radiotherapy bolus material and a gadolinium (Gd) solution were placed within these holes to determine if certain materials would be feasible and practical for examining distortion in MR images. These materials (excluding the solid wax candles) were placed into straws for containment and easier placement within the phantom (Figure 4.3).

2. **Lego®**

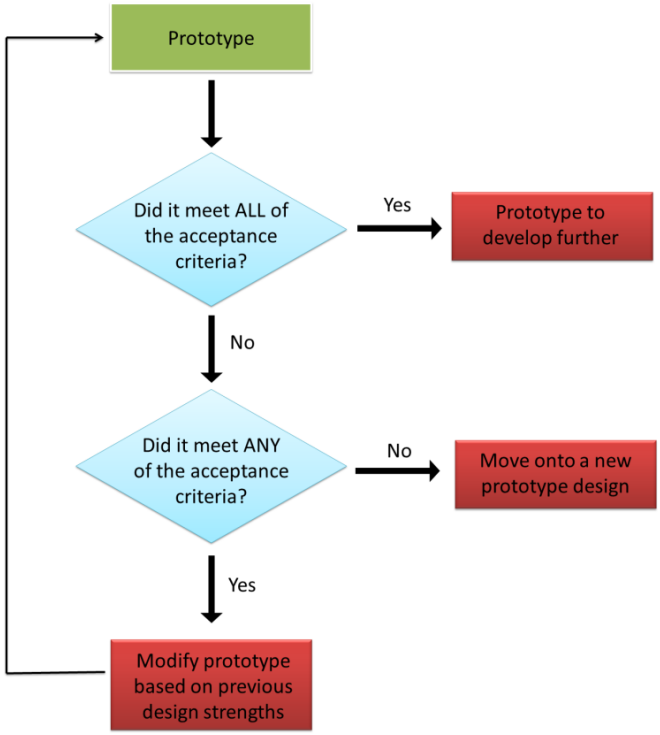

Figure 4.1: The development process of phantom prototypes. Progression was based on the conformity to the acceptance criteria.

Figure 4.2: Anthropomorphic phantom used (with breast attachments filled with signal producing materials).

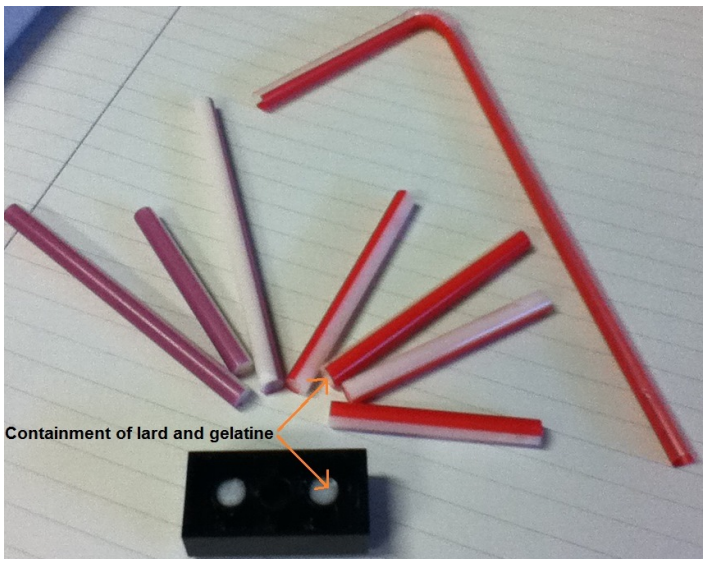

Figure 4.3: Lego and straws filled with lard and gelatine for containment and ease of placement within the anthropomorphic phantom.

The known geometry of Lego® blocks was utilised in the next prototype. Similar studies have conducted small scale investigations [110, 111]. Rather than immersing the Lego® blocks within a solution as previous studies had done, the cavities under blocks were filled with lard or gelatine as with the previous prototype (Figure 4.3), to investigate how these materials showed within this known geometric structure.

3. **Styrofoam and water**

   Dow Styrofoam (extruded polystyrene insulation) sheets were cut and inserted into a plastic container filled with water (Figure 4.4). Each foam insert (of 19 mm slice thickness) had small holes placed randomly throughout, allowing for the water to pass through. These material selections were made based on the variation between the density of each material (Styrofoam minimum density 0.02 g/cm^3; water 1 g/cm^3). The varying densities would see varying attenuation of each material on CT, giving different intensities in the image between the two materials. For visualisation on MRI, the Styrofoam structure does not contain loosely bound hydrogen and therefore would provide a negligible signal when imaging water.

4. **Styrofoam and vitamin E capsules**

   Six sheets of the aforementioned Styrofoam were milled into a shape designed to fill the bore of the scanner with maximum dimensions of 350 mm in height and 550 mm in width (Figure 4.5). The sheets were assembled together, giving the prototype a

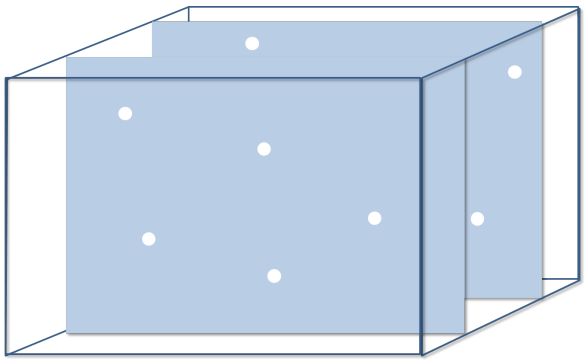

Figure 4.4: Schematic of the Styrofoam-water prototype. The blue represents the layers of foam, with the holes throughout. The rest of the container was filled with water.

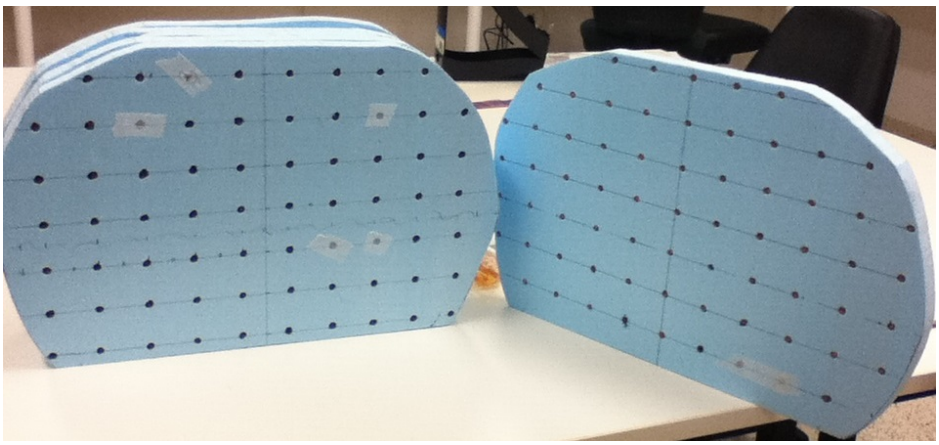

Figure 4.5: Foam-vitamin E prototype. Holes were systematically drilled in a grid pattern throughout the foam with the holes filled with vitamin E capsules.

length of 150 mm. Each slice contained holes drilled in a systematic grid pattern, defined in Cartesian coordinates. Each hole was approximately 8 mm in diameter to enable the insertion of Vitamin E capsules (19 mm length, 8 mm diameter) within each. The capsules were the source of signal for the MR images. Alternating foam layers had an offset grid pattern so each capsule could be distinguished between the layers and providing a means for determining through plane distortion, rather than only investigating the distortion in an axial plane.

5. **Styrofoam and MRI markers**

   A small scale prototype following the previous design was developed to test specific MRI markers as opposed to vitamin E capsules as the phantoms grid points. Each foam layer was milled into a baseless circular shape with a height of 160 mm and a width of 130 mm. Four layers of foam were assembled together, giving a length of

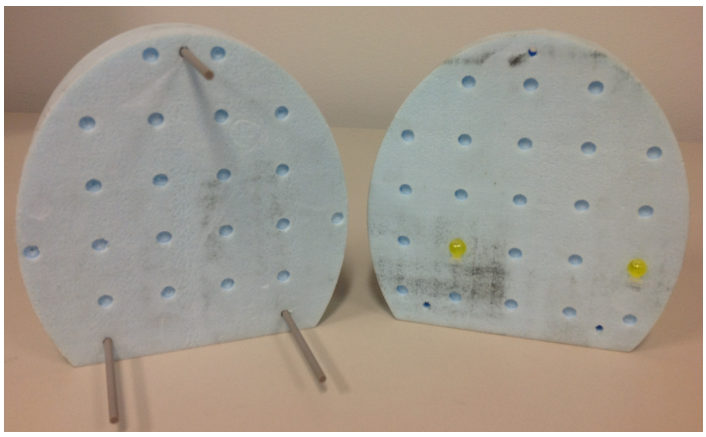

Figure 4.6: Styrofoam-marker prototype. The Styrofoam housing structure with small holes systematically drilled within to form two offset grid patterns. Two markers are shown placed in the phantom (yellow)

76 mm. Small indentations were systematically placed on each foam sheet to allow for the placement of Beekley PinPoint MRI markers (Figure 4.6). These commercial markers consisted of Radiance® liquid contained within a 6 mm plastic diameter. The offset grid pattern was included in this prototype.

6. **Uniboard and MRI markers**

   The next prototype saw the Styrofoam from the previous design replaced by layers of flat sheet panel polyethylene and polypropylene (Dotmar Uniboard Eco) (Figure 4.7). This material is marketed for construction purposes as a timber replacement material. It consisted of a combination of high density polyethylene and polypropylene to give a rigid structure whilst still maintaining a lighter weight than the same volume of liquid with a specific gravity of 0.7 g/cm^3. The phantom shape, offset grid pattern and placement of MRI makers was the same as the previous prototype. The thickness of this material was 15 mm, giving the prototype a length of 60 mm.

4.2.3 Prototype Performance

Table 4.2 summarises each prototypes performance in terms of the assessment criteria for a suitable phantom design. Most prototypes were initially built on a small scale to assess the feasibility. If it was determined that they did not meet some of the criteria and would therefore not be a feasible solution, then the design was not pursued any further (indicated in the table as *Not assessed*). For some prototypes, a larger size could have been feasible but

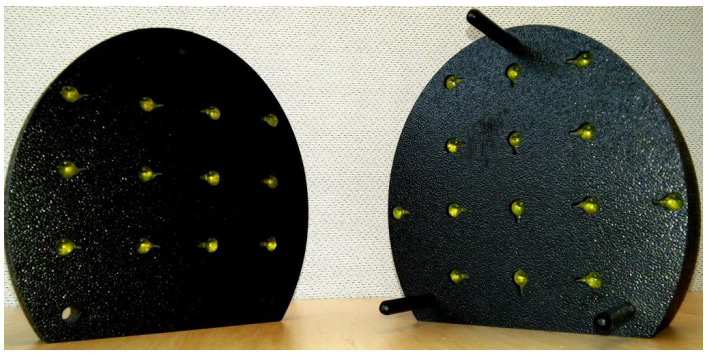

Figure 4.7: Uniboard-marker prototype. The Uniboard housing structure with the holes systematically drilled to form the offset grid pattern between layers within which the yellow MRI markers are placed.

Table 4.2: Comparison of the acceptance criteria performance for each prototype.

Prototype	*MRI compatible?*	*3D grid?*	*Practical?*	*Large FOV?*	*Visible?*
CIRS	✓	✓	✗	✗	Gd✓† Other✗†
Lego	✓	✓	✗	Not assessed	Not assessed
S'foam/Water	✓	✓	✗	Not assessed	✓
S'foam/capsule	✓	✓	✓*	✓	✓ †
S'foam/marker	✓	✓	✓*	Possible	Not assessed
Uniboard/marker	✓	✓	✓	Possible	✓ †

S'foam = styrofoam
* Limited long term use
†MRI required additional signal source (saline bags or additional phantoms)

was not specifically tested in that prototype having already been determined as possible in a previous design (indicated in the table as *Possible*). Since the development was for an MRI compatible phantom, all prototypes met this criterion with all design ideas excluding the use of any ferromagnetic materials. All MRI scans performed were acquired on 3T Siemens MRI systems. To reduce the effects of susceptibility artefacts, the pixel bandwidth was set to 440 Hz/pixel.

1. **Anthropomorphic phantom**

   The cylindrical dosimeter holes allowed for placement of the signal materials when the plugs were removed. However due to the grid pattern of the plugs, the same plug in 2 adjacent layers could not both be filled and still maintain the desired 3D grid point

Figure 4.8: Anthropomorphic phantom with selected dosimeter holes. Note the saline bags beside the phantom to produce enough signal for the MRI scanner to pick up.

structure. This limits the number of points available for use.

Filling such small, open ended volumes with the tested materials was not a practical solution. The gadolinium solution, while contained within straws and visible on MRI (with an additional signal source - see Figure 4.8), was not an ideal solution for use throughout the entire thorax region. To do this effectively, the straws needed to extend through multiple layers of the thorax and therefore this would inhibit the 3D grid structure in the z-direction (through the length of the scanner). For gadolinium, lard, gelatine and radiotherapy bolus material, air bubbles were present within each hole. Getting the materials in and out of the plug holes was a time consuming process. Because the phantom was for clinical dosimetry measurements it would need to be pulled apart after every MRI measurement and all of the signal producing materials removed.

The whole thorax region and breast inserts were small in size meaning that the FOV would not adequately be covered. The thorax region (without breast inserts) had dimensions of 20 x 25 cm (with variable length depending on the amount of phantom slices investigated). This does not cover a large enough volume required for full FOV distortion assessment for RTP.

CT images of the phantom revealed that the materials were difficult to differentiate between the phantom itself and therefore not providing a great gold standard to compare the grid point locations to. On MRI, the limited amount of material being tested in the prototype meant that additional signal was required to image the phantom (in the form of saline bags or additional MRI phantoms). Whilst the gadolinium solution showed up on both T1 and T2 weighted images, the lard, gelatine and bolus and wax did not. By the time this prototype was imaged on MRI the lard, gelatine and bolus had dried out, again reducing the amount of signal coming from each grid point location. The

molecular structure of the wax candles used was not useful for MR imaging.

2. **Lego®**

   The cavities under the Lego® blocks provided a 3D grid pattern. However, as with the anthropomorphic prototype, filling these cavities with the lard, gelatine and bolus materials was not a practical solution. Air bubbles were present in each cavity after each material had been inserted. Creating a larger grid structure out of the blocks and immersing in a liquid would still give air bubbles on the surface of the blocks and additionally, would be difficult to contain over the volume that was trying to be achieved. For this reason this prototype was only investigated on a small scale.

   CT images of the blocks showed the 3D grid points well, since comparing against surrounding air. The same signal issues with the materials investigated in the anthropomorphic phantom would have been present when imaging this prototype and hence MR imaging was not performed. With a more efficient way of removing air bubbles, Lego® may be a effective alternative. However, the weight would still be significant if filling a Lego® based structure with liquid or fill options over a large volume.

3. **Water and Styrofoam**

   The water filled holes in the Styrofoam enabled a good 3D grid pattern, able to determine the point location in an axial plane (x and y) and knowing its position along the length of the scanner (z) by the position of each foam board (Figure 4.9). This was nicely visualised on MRI. However, due to the continuous flow of water from one side of the board to the other through the hole, the grid was not ideal for assessing through plane distortion.

   The difference in density between the foam and water saw the foam float on top of the water unless secured to the sides of the container and the lid weighted down. The water phantom used to weigh down the lid also provided additional signal which enabled a prescan to be performed (for this and other prototypes where the signal volume was small). For a large FOV phantom following on from this design, the weight and containment of the liquid that would be required would be impractical for transportation and routine clinical distortion testing.

4. **Styrofoam and vitamin E capsules**

   The aim of this prototype was to overcome some of the issues observed in the previous design. Assembling the layers of Styrofoam and inserting the vitamin E capsules

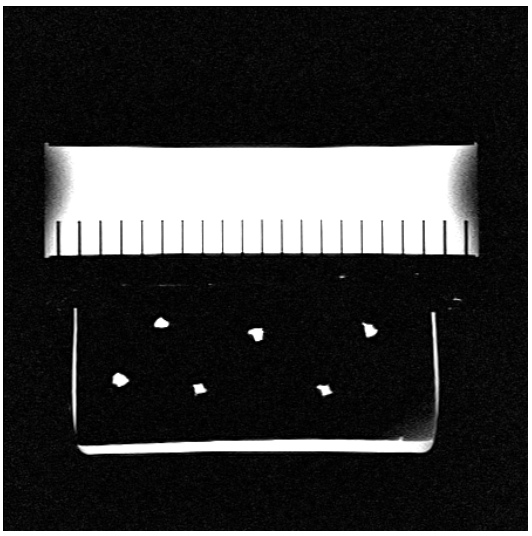

Figure 4.9: An MRI of the water and Styrofoam prototype. The holes in the Styrofoam can be clearly defined. Note the additional phantom placed on top on the prototype to enable enough signal for image acquisition.

within each layer meant each grid point was completely localised in all 3 imaging planes. The capsules were clearly visible in both CT and MR images (Figure 4.10). In the CT, the foam had minimal x-ray attenuation which allowed for the higher attenuating capsules to be well defined. The Styrofoam was not observable on the MR images and a comparison of the grid point locations between the 2 modalities could easily be made.

The lightweight material meant that the prototype could be easily designed on a larger scale, with the consideration of weight being reduced, particularly when compared to liquid filled phantoms. The prototype dimensions showed the required FOV was achievable in the axial plane, with the potential to increase the phantoms length (coverage in the z plane). The offset grid pattern was successful in distinguishing between capsules in adjacent layers whilst still making good use of the space available. While the capsules were large in length, this gave enough signal to be able to image that phantom. Also, since analysis would be undertaken looking at shifts in the overall structure of each capsule, the length was not found to inhibit the quantification of geometric distortions.

On making this larger sized prototype, it was determined that the Styrofoam was not an ideal long term solution. Concern was raised over its suitability as a geometrical test object, owing to the damage and deformation of the Styrofoam that resulted over a short period of time. Additionally, whilst the phantom was large, the number of

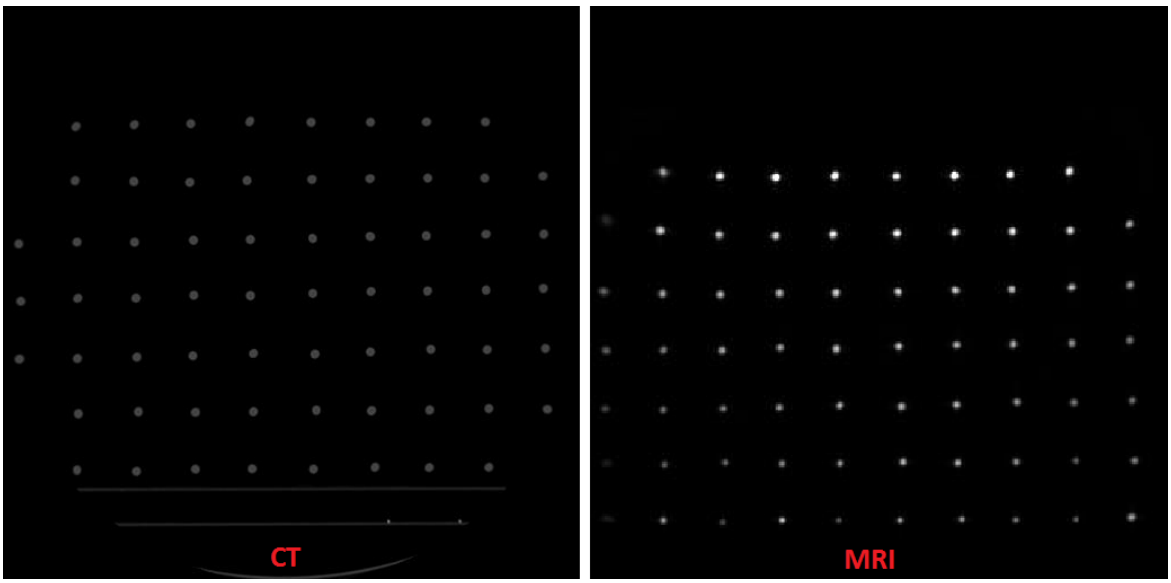

Figure 4.10: Axial images of the Styrofoam water phantom prototype on CT (left) and MRI (right).

capsules used for this prototype was small and additional signal was required in order to image the phantom. Since this was still a prototype design, the number of capsules would be increased and the spacing between them decreased in order to obtain greater signal and eliminate the need for an additional signal source during imaging.

5. **Styrofoam and MRI markers**

   This prototype was investigated at the same time as the following one. The capsules were found not to be a suitable option for large scale 3D distortion measurement (see below).

6. **Uniboard and MRI markers**

   The Uniboard housing provided a more rigid phantom structure that was deemed as more appropriate for long term use and any required transportation.

   The MRI markers were found not to be as effective at providing the 3D grid point signal. Each marker had a considerably large air bubble when compared to the overall marker volume which was clearly visible on both CT and MR images. The air bubbles would increase the susceptibility artifacts from the phantom itself and reduced the amount of signal available. The vitamin E capsules have a cylindrical shape which is better for minimising susceptibility effects [112].

   From this prototype it was determined that the Uniboard structure with the vitamin E

capsules provided the best fit to the assessment criteria and this was developed further for the construction of the final phantom.

4.3 Final Phantom Design

4.3.1 Design features

The final phantom (Figure 4.11) consisted of layers of flat sheet panel polyethylene and polypropylene (Dotmar Uniboard Eco) as the housing material. Vitamin E capsules were inserted throughout to provide the MRI signal. The phantom was cylindrical in shape with a flat bottom for stability giving a diameter of 500 mm and height of 375 mm. The length of the phantom was 513 mm, exceeding the limits of the standard imaging capabilities of the MRI scanner utilised, quoted as z = 450 mm.

Each Uniboard layer had a thickness of 19 mm. A total of 27 layers were used, 14 each layer containing 227 capsules and 13 layers each containing 204 capsules. This resulted in a total of 5830 capsules inserted into the phantom. Holes 8 mm in diameter were drilled through each layer to ensure tight fit of the vitamin E capsules to reduce any air gaps. The cylindrical capsule shape (diameter 8 mm; length 19 mm) was chosen to minimise susceptibility effects from the capsules themselves [112]. Each alternating layer had these holes drilled in an offset grid pattern (Figure 4.12), with this grid pattern being defined in polar coordinates. Polar coordinates were used to get the maximum number of grid points as possible within the phantom, following the circular nature of the phantom. This offset grid position enabled observation of through plane distortions (which would not be as achievable with capsules positioned back to back or with a rod structured phantom). In the central phantom compartment, 2 axially centralised capsules were removed from the phantom in order to enable localisation of the central phantom region within the acquired images.

The phantom material had a density of 0.7 g/cm^3 to reduce the overall weight, with the total phantom weight approximately 60 kg which, whilst is heavy, is lighter than a water based phantom of the same size would be. A base constructed of the same material (external dimensions of 800 mm x 500 mm) enabled steady transfer of the phantom between CT and MRI. A central section of the base tray (dimensions of 513 mm x 445 mm, corresponding to the phantom base) was pitted, leaving a thickness of 9 mm. Within this, the phantom

Figure 4.11: Photograph of the distortion phantom positioned in a 70 cm wide bore 3 T Siemens Skyra.

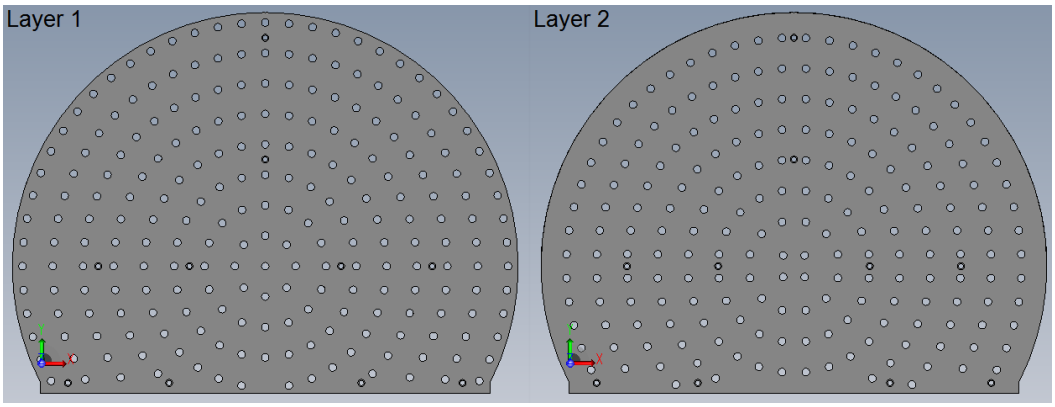

Figure 4.12: Alternating layers in the phantom. Note the offset grid pattern between each layer for 3D point localisation. This ensures distorted points don't overlap with capsules in adjacent layers, aiding in through plane distortion assessment.

body was placed and the base section held together rigidly. Ten plugs made from the same Uniboard material with length of 19 mm and a diameter of 5 mm were positioned between every layer to aid in holding the phantom together.

The layered structure of the phantom meant that transportation of the phantom to different centres is achievable. The layers also allow the removal or replacement of capsules, as may be required for analysis purposes and allows for different volumes of interest to be investigated by imaging a reduced number of layers.

4.3.2 Criteria testing

The assessment criteria were investigated after the construction of the final phantom. The design and manufacturing process ensured that there was no ferromagnetic materials within the phantom, ensuring the phantom would be safe for use in a strong magnetic field and additionally there would be no artifacts due to the presence of small traces of such materials. From a practical perspective, the phantoms tray and handles made transportation of the phantom achievable. The insertion of enclosed vitamin E capsules within the holes in the housing structure provided a nice clean way of obtaining the 3D grid points and without needing to contain a large body of water.

Imaging the phantom on both CT and MRI assessed the visualisation of 3D grid points, large FOV and the internal phantom structure on each modality. Since MR images are subject to distortion, a geometric "gold standard" of the phantom was required to determine the exact location of each grid point. Hence, as was done in Chapter 3, a CT scan of the phantom was obtained, providing a reference location for each capsule within the phantom that could then be compared to the MR images acquired.

Figure 4.13 shows axial images of the internal structure of the same section of the phantom as viewed on CT and MRI. The capsule locations are clearly defined, with enough intensity contrast between the capsules and the housing materials. This can be improved by thresholding the images to remove noise. Figure 4.14 shows 3D reconstructions of the phantom as visualised on both imaging modalities. Particularly in the MR image, it can be seen that the grid points are well defined in 3D space.

When assessing MRI distortion with phantom based measurements, the location of each in-

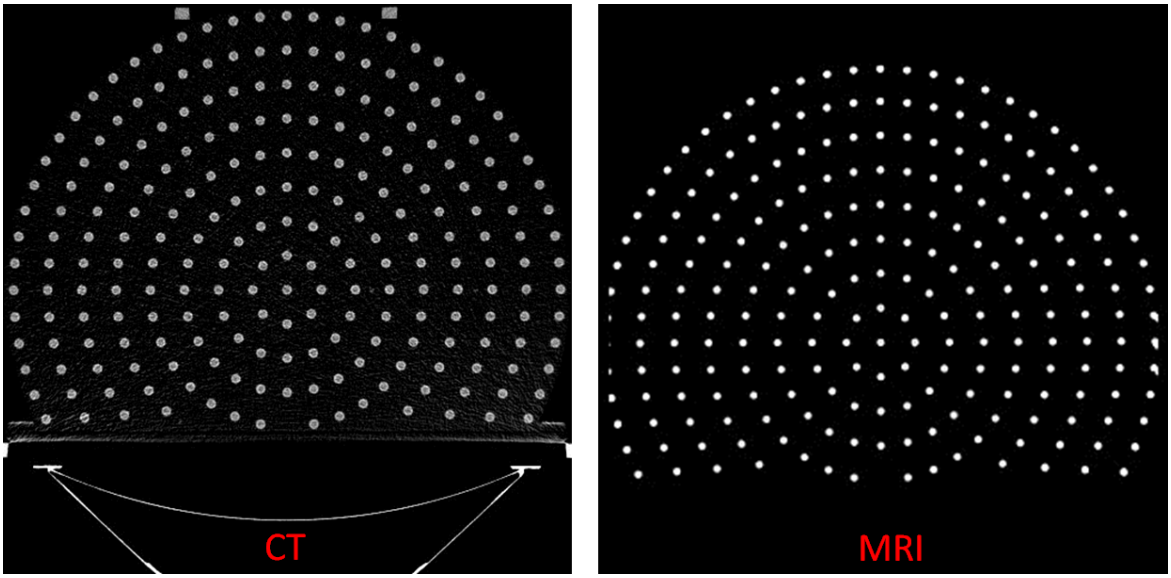

Figure 4.13: Axial images of the phantom on CT (left) and MRI (right).

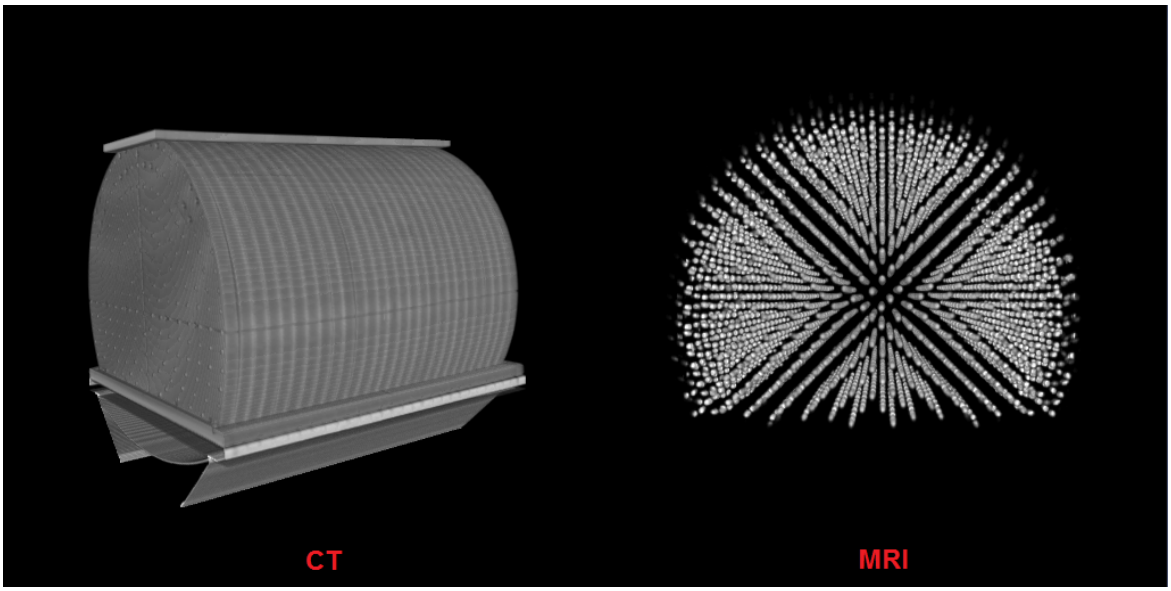

Figure 4.14: Rendered 3D volumes of the phantom visualised on CT (left) and MRI (right)

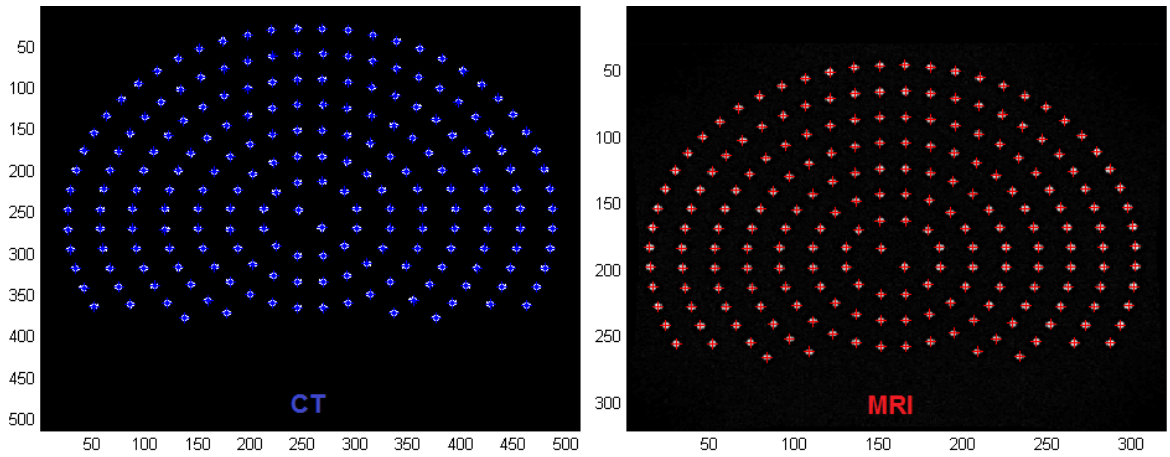

Figure 4.15: Centroid locations of each capsule at the centre of the phantom as determined by MATLAB for a thresholded CT (left) and a MR image (right).

dividual grid point must be determined on both imaging modality and compared to quantify the distortion. For initial testing, code was developed in MATLAB to determine the centroid position of each capsule within an axial plane. Figure 4.15 shows the result, with the calculated centroid locations overlaid on the corresponding CT and MR images.

The largest axial FOV possible on the Siemens 3 T Skyra closed bore MRI scanner (500 mm x 500 mm) was used to scan the phantom (Figures 4.13 and 4.15), highlighting the full FOV coverage of the phantom in this imaging plane. The phantom coverage through the length of the scanner (z) is highlighted in Figure 4.16, with the phantom extending beyond the standard imaging capabilities of the scanner. The image on the left shows the true position of each capsule as visualised on CT at a distance of 155 mm from phantom centre. The image on the right shows how the same section of the phantom is visualised on MRI when the phantom centre is set up at isocentre for image acquisition. Many closed bore scanners are quoted as having a FOV of 40-50 cm in all imaging planes for diagnostic purposes. The dimensions of this phantom are large enough to encompass this region for static MRI acquisition. Figure 4.16 highlights that the phantom is long enough to visualise regions within the scanner where distortions become so severe that the geometric integrity is severely compromised.

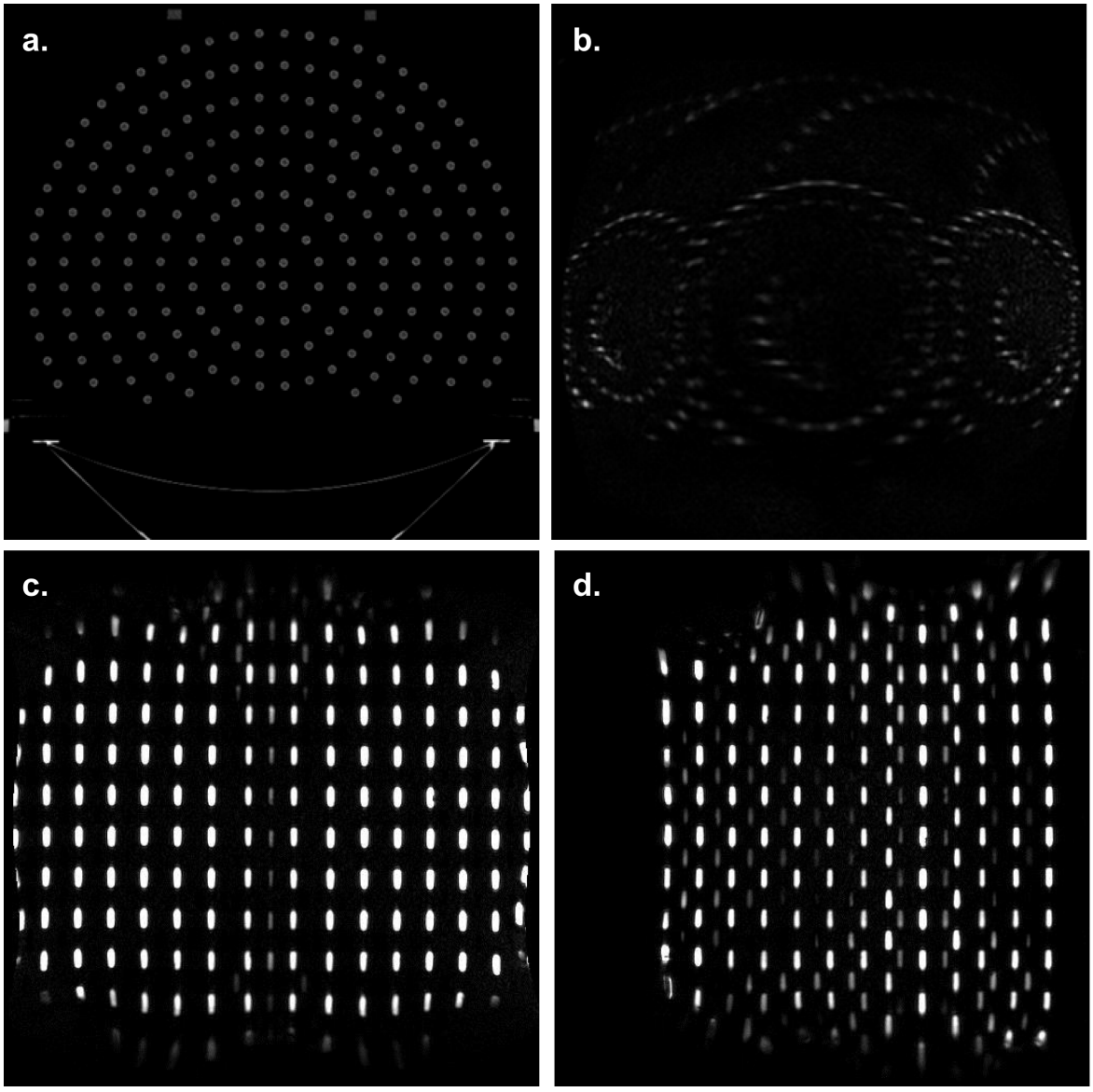

Figure 4.16: Phantom a) axial slice on CT, b) axial slice on MRI at -155 mm from the centre of the phantom, c) coronal slice on MRI and, d) sagittal slice on MRI.

4.3.3 Design limitations

The phantom was designed specifically for distortion assessment of a Siemens 3 T Skyra with a wide bore of 70 cm. Due to its size, it could potentially not fit into smaller bore systems. If the phantom did fit within a 60 cm bore scanner, imaging would be limited to acquisition using only the integrated body coil as there would not be adequate space to place surface coils over the top. The shape was also designed specifically for the scanner. This phantom design therefore may also not fit into other scanner configurations such as open bore systems where there could be greater restrictions for the vertical dimensions.

The structure of the housing material created some practical issues in the analysis process. While the overall material has a density of 0.7 g/cm^3, the density changes throughout the thickness of the board (Figure 4.17). The outer edges of the board is more compact, providing a strong exterior. The inner core is more foam in structure, designed to reduce the overall weight. While this variation is beneficial for structure and weight considerations, it creates an issue when imaging with CT. Figure 4.18 shows how this density variation manifests in the CT images. In the central region of each layer (indicated in yellow), the attenuation variation between the capsules and the housing material vary enough for the capsule locations to be properly distinguished. The edges of each layer (indicated in red) show that the higher density region results in increased beam attenuation, similar to that of the capsules resulting in difficulties accurately defining each capsule location. Figure 4.19 shows how this correlates to CT numbers in Hounsfield units (HU), as measured on the acquired CT images in the Pinnacle treatment planning system. For the purposes of analysis these high density regions, as visualised on CT were masked out of the image by way of image thresholding, to ensure that the capsule locations could be accurately determined. Since the material does not show on MRI, this density variation does not have any visual effect here.

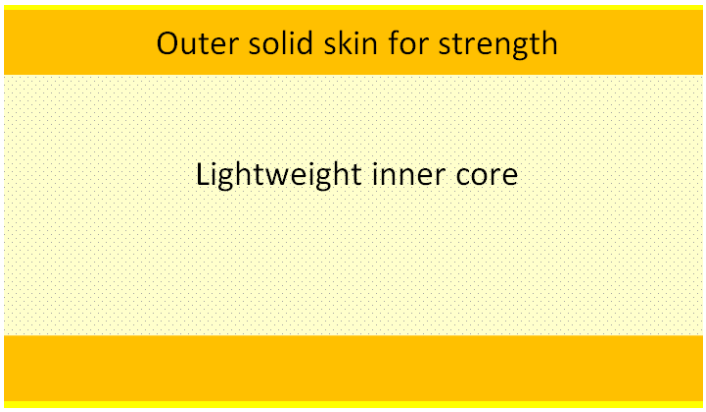

Figure 4.17: The internal structure of the Uniboard material.

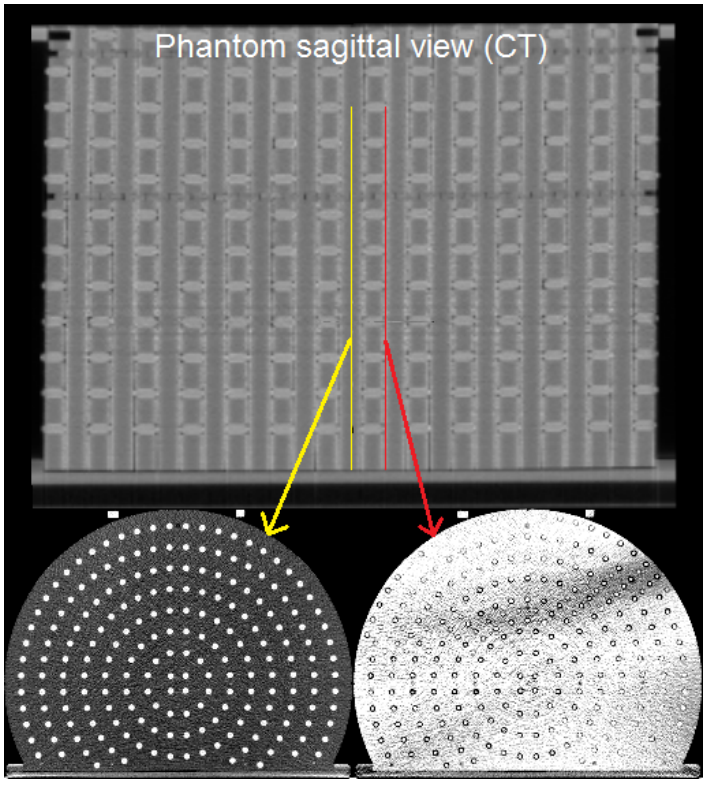

Figure 4.18: Density variation through the Uniboard layers visualised on CT. Top: sagittal CT of the phantom. Bottom: axial image of the phantom corresponding to the middle(yellow) and edge (red) of each layer.

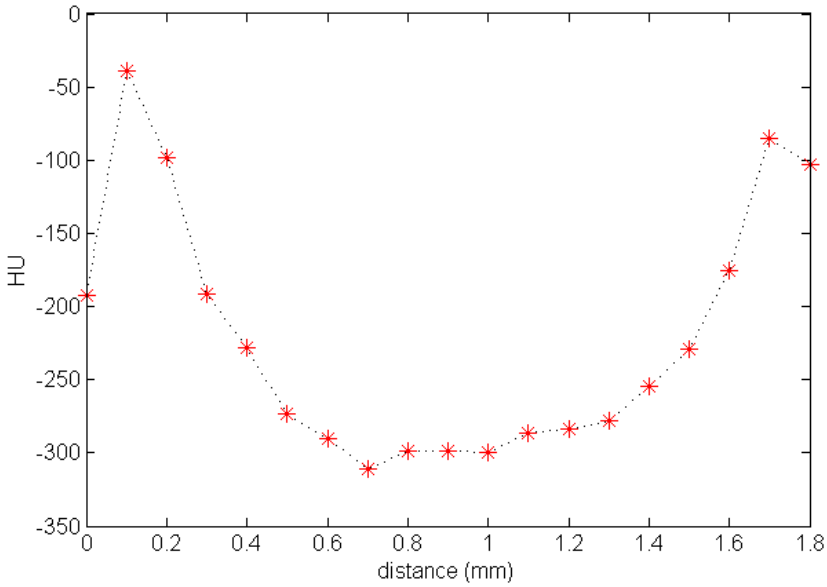

Figure 4.19: Average CT numbers across the thickness of the Uniboard layers.

4.4 Conclusion

The novel phantom developed permits mapping of MRI geometrical accuracy across the full imaging FOV as required for RTP. The axial size of the phantom encompasses the size of patients undergoing MR scanning, whilst still allowing for the placement of surface coils over the phantom. The length makes it suitable for imaging over various scan lengths without the need for physical relocation and re-scanning. This phantom allowed for full 3D quantification of a radiotherapy based MRI scanner (Chapter 5), with these measurements then utilised in determining the dosimetric impact of geometric distortions for whole breast radiotherapy (Chapter 6).

Chapter 5

3D distortion quantification for a dedicated radiotherapy MRI scanner

5.1 Introduction

The RTP process requires accurate patient geometry. It is fundamental for ensuring the dose planned is delivered to the tumour region whilst limiting dose to organs at risk (OAR). With an increase in the use of MRI for RTP purposes [96], assessing geometric accuracy is important, particularly when considering the potential for MRI-only planning.

System related geometric distortions in MRI are created by non-uniformity of the main magnetic field (B_0) and nonlinearities in the gradient fields. Distortions in MR images have decreased in magnitude with improvements in technology. Most modern scanners allow for shimming and on or off line application of vendor correction algorithms to decrease the gradient nonlinearity and some B_0 field inhomogeneity effects. While vendor supplied correction algorithms provide a reduction, residual distortions still remain in various regions of the scanner [Chapter 3] [38, 39].

Clinical MRI scanner performance is optimised around the isocentre of the scanner, with gradient linearity and B_0 field homogeneity decreasing with increased distance from isocentre. Distortion magnitude therefore increases radially outwards, even with the application

[1]Part of this chapter has been published:
Walker A, Liney G, Holloway L, Dowling J, Rivest-Henault D, Metcalfe P. Continuous table acquisition MRI for radiotherapy treatment planning: distortion assessment with a new extended 3D volumetric phantom. *Medical Physics* 2015; 42(2):1982-1991

of correction algorithms [Chapter 3]. Improvements in scanner and coil technology has resulted in the ability to image anatomy in regions at larger distances from isocentre than previously achievable, where distortion considerations become more imperative. The maximum diagnostic imaging field of view (FOV) is typically 40-50 cm in all imaging planes. For RTP, the loss in geometric accuracy with increasing distance from isocentre is likely to considerably reduce the maximum FOV. Geometric accuracy of within 2 mm is required for RTP imaging and treatment QA [54], with MRI distortions greater than this requiring consideration.

When utilising MRI for RTP, the required imaged anatomy depends on its application, whether acquired for use in conjunction with CT or for the purposes of MR-only planning. In some cases, registering MRI to CT may warrant smaller FOV coverage (e.g. prostate). In such cases images may only need to encompass the anatomy of interest for contouring and registration purposes. Other treatments (such as head and neck) may require a longer FOV which covers a large longitudinal extent of target and avoidance tissues. If considering MR-only planning, a larger axial FOV coverage would be required to ensure the patient skin surface is included for the required dosimetric calculations. For the purposes of RTP, the geometrical accuracy requirement over the scan length (x, y and z coverage) is more stringent than that required for routine diagnostic imaging. Spatial distortion assessment is a vital part of MRI quality assurance (QA) for RTP in addition to other specific QA required for RTP (e.g. surface coil intensity correction [68], laser alignment).

Modern clinical MRI scanners have moved towards wider and shorter bore designs to improve patient comfort. Magnetic field strength may also be increased from 1.5 T to 3.0 T, allowing faster imaging with improved imaging quality [3]. These features can make the optimisation of scanners more challenging, consequently increasing the geometric distortions. More scanners have moved away from spherically optimised to cylindrically optimised magnets to account for these features and to ensure the optimisation is more suited to the shape of the patients. All of these scanner designs have characteristic uniformity and linearity distortions. The AAPM report 100 for MR QA [43] recommends the geometric accuracy of clinical MRI scanners should be determined. A number of studies have investigated this on MRI scanners for the purposes of RTP [39, 49, 103, 104]. Comprehensive distortion mapping of each system is recommended to determine the tolerances and constraints to minimise MRI distortion impact for RTP or provide data for a correction scheme where appropriate.

On short bore systems, image acquisition with a moving table is one approach to increase the scan length in the z direction. This allows images to be acquired close to the scanner isocentre, where B_0 and gradient performance is optimised. Potentially, this could reduce the severe distortion effects at the edge of scans and improve the usable imaging range superiorly and inferiorly for RTP. Images can be acquired close to the isocentre at different table positions over a limited scan stitched together [113, 114]. A more recent approach involved image acquisition with the table moving continuously through the scanner at a constant velocity (sliding multislice (SMS)) [115–117]. Moving-table acquisitions have been investigated in detail in magnetic resonance angiography (MRA) and whole body MRI [116, 117], as well as for screening and staging in oncology [113, 118]. Investigations into its utilisation in radiotherapy is limited [114]. While the SMS technique can reduce the magnitude of distortions present in an image for a larger scan length, it does not completely remove distortions. The technique is designed to reduce the distortion components from the z axis with no additional benefit in the axial plane. One angiography study using SMS [119] demonstrated additional distortion effects and blurring in all 3 imaging planes when utilising this acquisition technique.

In this chapter, the developed 3D-phantom in Chapter 4 was utilised to quantify the geometric distortions on a dedicated MRI-simulator. Investigations were made to assess the performance of a moving table image acquisition option to determine potential benefit of this technique for RTP. Comparisons were made to conventional static table 2D and 3D image acquisition sequences. A sound understanding of the geometrical limitations for static and moving table acquisitions is essential for investigations into MRI acquisition techniques for utilisation in RTP. This chapter investigates the distortions from systematic factors and the variation in these with different acquisition techniques. Other distortion considerations including patient effects (susceptibility and chemical shift) on distortion as well as the impact of geometric distortion on inhomogeneity in MR images are presented elsewhere in the literature 2, 11, 29-31.

5.2 Method

5.2.1 Phantom

The phantom designed and built in Chapter 4 was used to measure distortions as required for this section of work. To validate the geometry and determine the location of the capsules within the phantom, a CT image provided the baseline geometric 'gold standard'. The phantom was scanned on an 85 cm bore, Brilliance CT big bore oncology CT scanner (Philips Healthcare). All CT images were acquired with a FOV of 500 mm x 500 mm (512 x 512 image resolution) with a scan length greater than 514 mm to ensure the whole phantom volume was imaged. Scans were acquired with a slice thickness of 1 mm so that the CT images could be used as a reference to analyse MR images of any slice thickness larger than 1 mm.

5.2.2 Phantom MRI scanning

MRI scans of the phantom were performed on a Siemens 70 cm bore Magnetom Skyra 3.0 T (Siemens Healthcare) (Figure 4.11). The manufacturer quotes the gradient linearity as an average deviation equal to 0.2, 0.3, 0.2 % (x, y, z %) over 30 cm and 0.4, 0.5, 0.3 % over 50 cm. The magnet is cylindrically optimised, designed to achieve a homogeneous volume 1.5 times that of an ellipsoid system. Guaranteed homogeneity of the magnet over a 50 cm x 50 cm x 45 cm is quoted as less than 4 parts per million (ppm). All scans performed underwent standard tune-up B_0 shimming localised to the imaging volume. For this study, 3 different acquisition methods were investigated:

1. Standard 2D image acquisition
2. 3D volume image acquisition
3. Continuously moving table acquisition: Total Imaging Matrix, Continuous Table (TimCT)

For each image acquisition sequence, 2 images of the phantom were obtained. The frequency encode directions between these 2 datasets were rotated by 180^o to enable separation of B_0 and gradient distortion components during the image analysis process [51, 65]. A bandwidth of at least 440 Hz/pixel was implemented for each sequence as would be used for RT planning protocols [3] to minimise susceptibility and chemical shift. Vendor 2D or 3D

Table 5.1: Acquisition parameters of standard imaging sequences.

Sequence	*Slice thickness (mm)*	*TE/TR (ms)*	*Scan length (mm)*	*Pixel BW (Hz/pix)*	*Resolution (pixels)*
SE	2	12/2760	252	445	320 x 320
SE	3	12/2760	368	445	320 x 320
CISS	2	3.15/6.84	353	460	320 x 320

correction algorithms were applied during image acquisition as available. Scanner gradient nonlinearities are stored in the system as spherical harmonic coefficients, enabling the gradient field to be derived at any location within the magnet. The coefficients are used to calculate the ideal gradient values for the scanner which are then applied to correct each voxel position and signal intensity accordingly throughout the imaged volume. The 2D correction provides only an in-plane correction to the distortion while the 3D correction accounts for through-plane distortion as well. These correction algorithms provide reproducible results within 0.5 mm. Distortions were reported at the centre of each capsule as visualised on each slice within each dataset. Based on acceptance criteria for RTP imaging and treatment QA [54], distortion values larger than 2 mm were considered to be significant.

5.2.3 2D and 3D acquisition sequences

The imaging parameters for the static 2D and 3D image acquisitions are outlined in table 5.1. For the 2D image acquisition, a standard spin echo (SE) sequence was used. A steady state gradient echo sequence (CISS - constructive interface in steady state) provided the best image quality for the 3D acquisition of the phantom and was consequently investigated. The maximum scan lengths achievable for the given slice thickness and coil capabilities for each sequence was acquired. The phantom centre was aligned to the scanner isocentre. For these scans 2D correction was available as part of the imaging protocol whereas 3D correction was performed retrospectively on the scanner console.

5.2.4 TimCT - extended FOV

The phantom was placed on the scanner and covered with two 18 channel body coils for imaging the whole phantom volume with TimCT. The table was then moved into the scanner

Table 5.2: Acquisition parameters of the TimCT sequence and the corresponding sequence without the TimCT option utilised.

Sequence	*TE/TR (ms)*	*Scan length (mm)*	*Pixel BW (Hz/pix)*	*Resolution (pixels)*	*Table speed (mm/s)*	*Slab length (mm)*
Spoiled GRE (TimCT)	1.47/190	540.3	610	512 x 512	1.1	60
Spoiled GRE (TimCT)	1.47/190	550.5	610	512 x 512	2	110
Spoiled GRE (Non TimCT)	1.47/452	365	610	512 x 512	0	365

so that one end of the phantom was located at the scanner isocentre and the whole phantom could then be moved through the bore. All images were T1 in-phase Dixon spoiled GRE sequences acquired with 5 mm slice thickness. Table 2 shows the imaging parameters for different table speeds. The slab length refers to the scan length being imaged as the table moved and was dependent on the table speed selected. After images were acquired with the TimCT option selected, the phantom was setup with the phantom centre aligned to the scanner isocentre. The same sequence was then acquired with static table acquisition for comparison. These scans were all acquired with the vendor 3D correction algorithm applied.

5.2.5 Distortion assessment

5.2.5.1 Image registration

Three dimensional quantification of the geometric distortion was obtained by rigid and deformable registration between the CT and MR images. Two programs were required for the registration process:

- MILXView is a 3D medical imaging tool developed by the Australian E-health Research Centre with the Commonwealth Scientific and Industrial Research Organisation define CSIRO allowing the visualisation and processing of 3D medical images.
- NiftyReg is an open-source software tool enabling the implementation of non-rigid and deformable registration between images. Version 1.3.9 of this software was utilised for this work.

A robust inverse-consistent registration algorithm was used to rigidly align the CT and MR images within MILXView [120]. The algorithm handled the position and orientation information contained in the image header and provided a fully automatic result. All MR images acquired were rigidly registered to the CT with 1 mm slice thickness, ensuring all datasets were in the same frame of reference. The MR images then matched the 0.98 x 0.98 x 1 mm voxel resolution of the CT dataset. Performance of the rigid registration was visually assessed before continuing. After rigid registration, each resulting MRI dataset was non-rigidly registered to the CT dataset. The deformable registration method was based on a cubic B-spline free-deformation model using a normalised mutual information metric from the non-commercial open source software (NiftyReg version 1.3.9) [121]. The registration was performed in 4 iterations with final grid spacing of 25 mm. In this implementation, all control points were optimised and interpolation performed in 3D across the whole image at each step. The accuracy of the registration algorithm was within half a pixel (MRI pixels: 1.6 mm x 1.6 mm).

MATLAB code was written to determine the centroid position of each vitamin E capsules on each CT slice. Distortion information was pulled out of the deformation fields obtained corresponding to these points so the distortion values were reported at the centroid position of each capsule. In doing this, the distortion was reported in regions where there is information provided by signals in both the CT and MR images and not in between capsules where distortion values are interpolated in regions of no signal.

5.2.5.2 Gradient and B_0 distortion components

Non-rigid image registration resulted in the determination of the total geometric distortion (dist_total). Following a previously reported method [51, 65] image acquisition was repeated with the frequency encode direction reversed. The frequency encoding direction (y) is subject to geometric errors from both B0 inhomogenity and gradient nonlinearity whilst the phase encoding direction (x) is only subject to distortions from gradient nonlinearities:

$$y_1 = y + \frac{\Delta B_0(x,y,z)}{G_{\mathrm{y}}} + \frac{\Delta B_{\mathrm{G_y}}(x,y,z)}{G_{\mathrm{y}}} \tag{5.1}$$

$$x_1 = x + \frac{\Delta B_{\mathrm{G_x}}(x,y,z)}{G_{\mathrm{x}}} \tag{5.2}$$

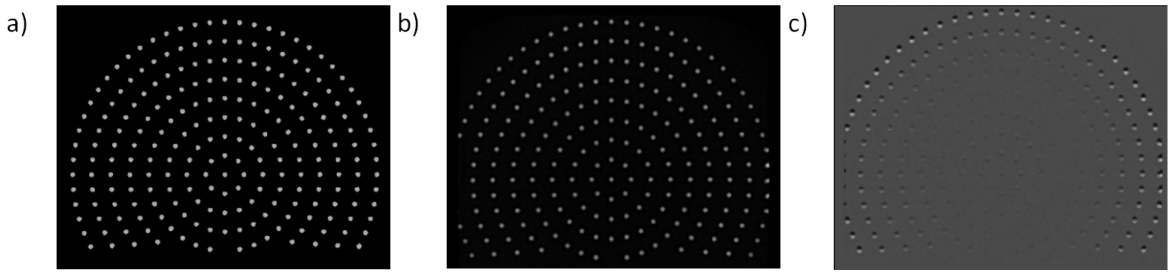

Figure 5.1: Phantom images a) CT, b) MRI with anterior (ant)-posterior (post) frequency direction and, c) subtraction of two MR images with frequency encode direction reversed.

where y_1 and x_1 are the distorted locations, y and x are the true position, ΔB_0 is the distortion contribution from B_0 inhomogeneity, G_y is the frequency encoding strength, G_x is the phase encoding strength ΔB_{G_y} is the distortion contributions from gradient nonlinearities in the frequency encoding direction and ΔB_{G_x} is the distortion contributions from gradient nonlinearities in the phase encoding direction. Analysis on images with reversed frequency encoding directions can separate these components. In reversing the gradients the direction of the ΔB_{G_y} term in equation 5.1 is reversed. Substituting the resulting equation into equation 5.1 gives:

$$y_1 = y + \frac{\Delta B_{\mathrm{G_y}}(x, y, z)}{G_{\mathrm{y}}} \tag{5.3}$$

Hence the difference in images of reversed frequency encode direction allows for the determination of the B_0 inhomogeneity effects.

In this study, a deformation field was obtained by registering the MR images of opposing frequency encode directions. The result was halved to give the component distortion due to B_0 inhomogeneity (dist_B_0) since the true position of objects lies halfway between its location in each image [65]. The B_0 distortion component was then subtracted from the total deformation field obtained in the MR-CT registration, giving the residual distortions due to the gradient nonlinearities (dist_Grad) (Figure 5.1). Subtraction of deformation fields was conducted using a Simple Medical Imaging Library Interface SMILI program.

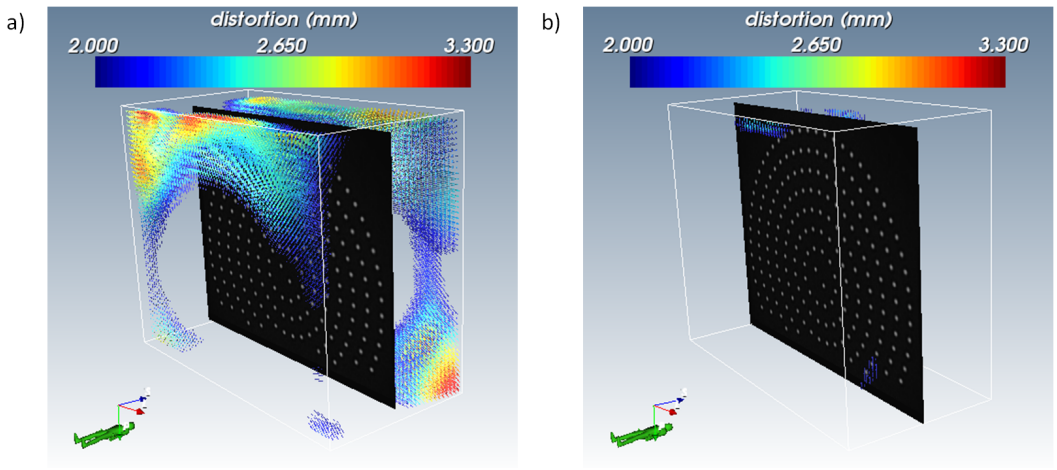

Figure 5.2: Vector maps indicating regions of distortion $\geq$ 2 mm for the a) dist_Grad and b) dist_B_0 components of distortion for the standard 2D SE acquisition sequence with 2 mm slice thickness with the 3D correction algorithm applied.

5.3 Results

5.3.1 Standard static acquisition sequences

Distortions due to residual gradient nonlinearities and B_0 inhomogeneities are separated in Figure 5.2 for the standard SE sequence acquired with 2 mm slice thickness (3D correction algorithm applied). The vector fields are thresholded to highlight regions within the imaging FOV where distortions were greater than 2 mm. The vectors indicate the total distortion in all directions (x, y and z). Distortions resulting from residual gradient nonlinearities are greater than those due to the B0 inhomogeneity. The dist_Grad were greatest at the superior and inferior regions of the image with dist_B_0 largest at the extreme regions of the axial FOV.

Table 5.3 indicates the overall geometric performance of each sequence (dist_total), accounting for variations in scan length due to sequence capabilities. The table includes results for 2D and 3D corrected images, the percentage of the phantom length scanned and differences in the image length acquired per second, based on the acquisition time of each sequence. Images with the retrospective 3D correction applied had an improved geometrical performance.

Figure 5.3 shows the variations in the frequency distribution of distortion magnitude across

the 3 sequences acquired, with 2D vendor correction algorithm applied compared to when the 3D correction algorithm is selected. Table 5.4 breaks down the mean, median and maximum distortion values for each scan.

The convergence region of the registration algorithm is defined as the region where the accuracy of the registration algorithm is better than 1 pixel. This region was found to be within a length of $\pm$ 119 mm and an axial radial distance of r = 180 mm from the centre of the scanner. The magnitude of distortion was accurately measured within this region, even when the spatial displacement greatly exceeded the 2 mm tolerance limit. Beyond this volume, extreme distortion resulted in some capsules no longer being visible in the image. As such, distortion measurements beyond this region could not be reliably measured but can be assumed to be much greater than 2 mm. Black rings began appearing beyond this point in the images with the 3D correction algorithm applied in regions of severe distortion or where capsules were not observable in the 2D corrected images.

5.3.2 TimCT

Vector field maps for the total distortion observed for the spoiled GRE sequence acquired with a static table and TimCT with table speeds of 1.1 mm/s and 2 mm/s are shown in Figure 5.4. The longer scan length imaged with TimCT is evident when compared to the static table acquisition. Distortion patterns for TimCT scans were more consistent through the phantom volume compared to the static table where a large reduction in geometric integrity was observed at the edge of the field where the through plane distortion was worse.

Table 5.5 highlights the mean, median and maximum distortion values (dist_total) for the different couch speed acquisitions. Figure 5.5 shows the variations in the frequency distribution of distortion magnitude across the 3 acquisition speeds.

Figure 5.7 shows the percentage of points within a defined phantom volume where distortions were observed to be greater than 2 mm for the static table, TimCT 1.1 mm/s and TimCT 2 mm/s scans on the left, and the 2 mm SE, 3 mm SE and 3D CISS on the right. The volumes were defined from the centre of the phantom, with varying through plane lengths ($\pm$ z) and radial distances in the axial plane (r) (Figure 5.6). All measurements were reported with respect to the phantom centre as opposed to scanner isocentre since this provided a consistent reference point for static and moving table acquisitions. The maximum distortion

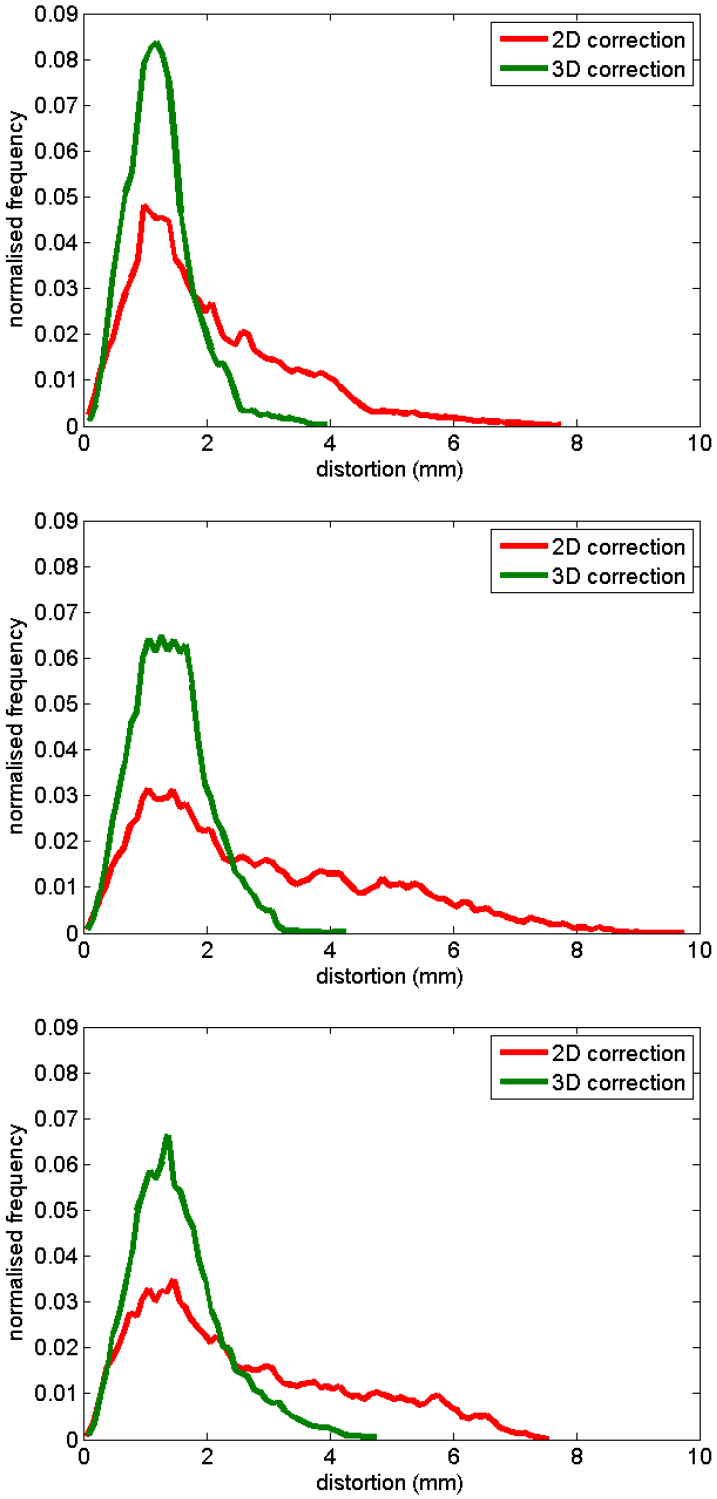

Figure 5.3: Comparison of the frequency distribution of distortion when applying the vendor 2D correction compared to 3D correction for the 2 mm SE (top), 3 mm SE (middle) and 2 mm CISS (bottom) acquisitions.

Table 5.3: Geometric performance of the standard acquisition sequences.

Sequence	*% phantom imaged*	*Distance from isocentre where distortion* $\geq$ *2 mm*	*% phantom with distortion* < *2 mm*	*Nominal acquisition time*[*] *(minutes : seconds)*
2 mm SE	49			29:56
- 2D corrected		98 mm	29	
- 3D corrected		152 mm	44	
3 mm SE	72			20:22
- 2D corrected		82 mm	30	
-3D corrected		154 mm	54	
CISS	69			13:30
- 2D corrected		93 mm	32	
- 3D corrected		148 mm	51	
Spoiled GRE (NonTimCT)	71	147 mm	47	2:41
Spoiled GRE (1.1 mm/s)	100	140 mm	87	9:30
Spoiled GRE (2 mm/s)	100	55 mm	61	5:26

* Nominal acquisition time = time required to image whole phantom

Table 5.4: Distortion comparison between 2D and 3D corrected images.

Sequence	*Mean*	*Median*	*Maximum*
2 mm SE			
2D corrected	2.07	1.69	7.88
3D corrected	1.25	1.19	4308
3 mm SE			
2D corrected	2.90	2.40	9.81
3D corrected	1.42	1.38	4.37
2 mm CISS			
2D corrected	2.64	2.16	7.62
3D corrected	1.56	1.43	4.89

Table 5.5: Distortion comparison between static Vs TimCT images.

Sequence	*Mean*	*Median*	*Maximum*
Spoiled GRE 0 mm/s*	1.60	1.46	6.07
Spoiled GRE 1.1 mm/s	1.33	1.23	4.42
Spoiled GRE 2 mm/s	1.78	1.65	5.80

* 71% phantom imaged

observed is reduced when TimCT is utilised. Table 5.3 compares the spoiled GRE sequence investigated for TimCT purposes to the standard static acquisition sequences.

Figure 5.8 compares the geometric performance of the spoiled GRE without TimCT compared to TimCT with a table speed of 1.1 mm/s over different radial distances and scan lengths from the scanner centre. It shows the volume percentage comparison in which distortions are less than 2 mm within the volume in question. Values greater than 1 indicate the TimCT sequence performed better geometrically.

As was found for the standard static sequence acquisitions, beyond the convergence region of a length of $\pm$ 119 mm and radial distance of r = 180 mm from the phantom centre on the static spoiled GRE, grid points were either not visible in the image or the distortions were too great for the registration algorithm to perform accurately beyond this point. The registration algorithm was not found to fail for the TimCT images.

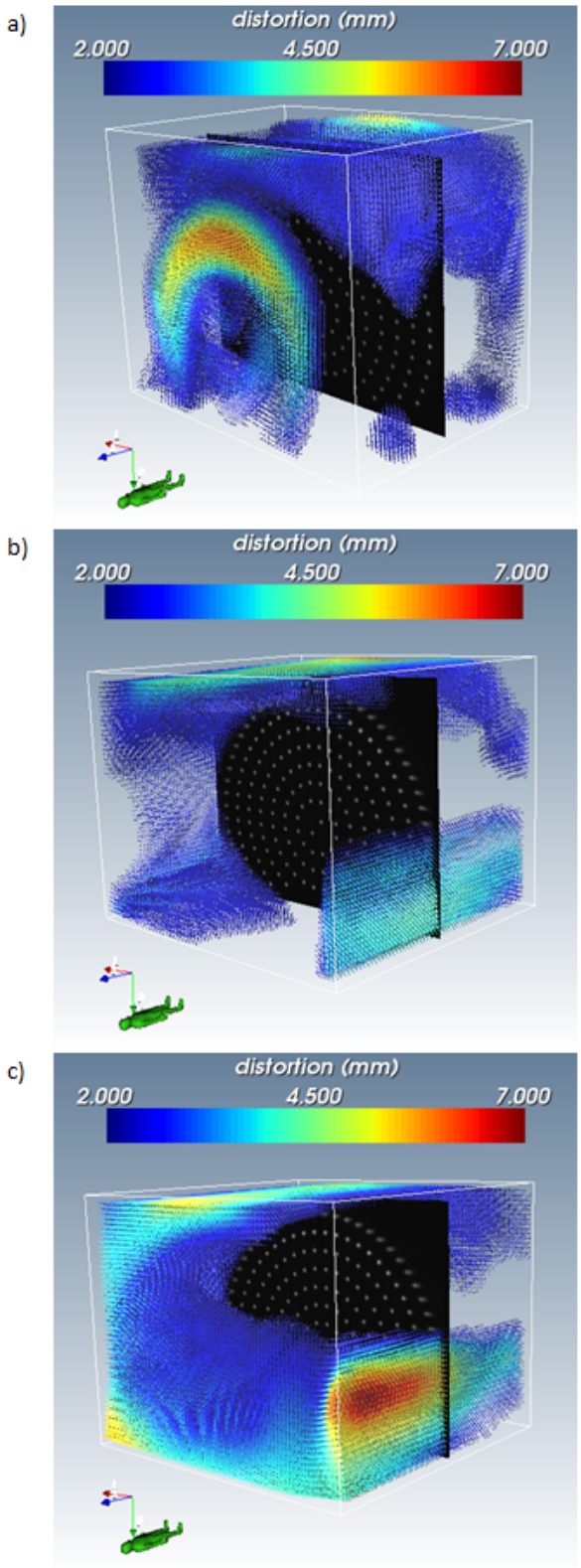

Figure 5.4: Vector maps indicating regions where total distortion $\geq$ 2 mm for the spoiled GRE sequence acquired with table speeds of a) 0 mm/s, b) 1.1 mm/s and c) 2 mm/s

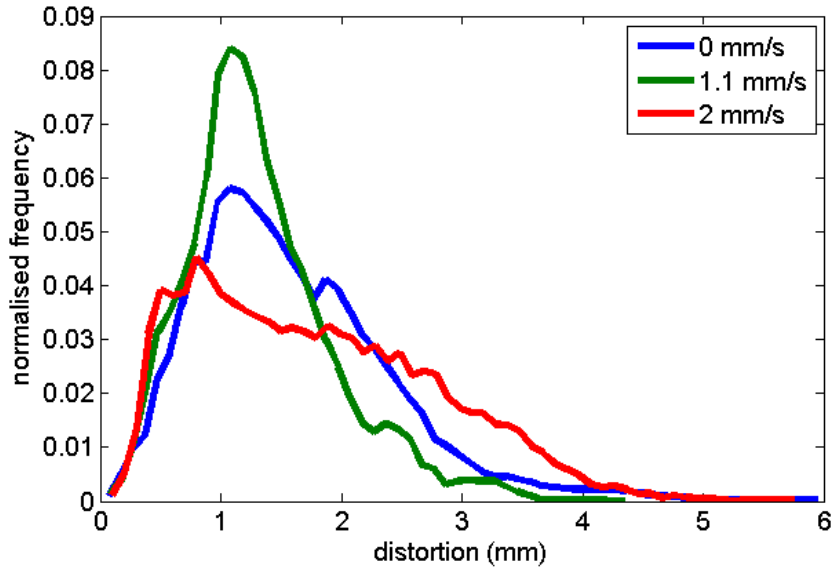

Figure 5.5: Comparison of the frequency distribution of distortion between acquiring images at the 3 different table speeds.

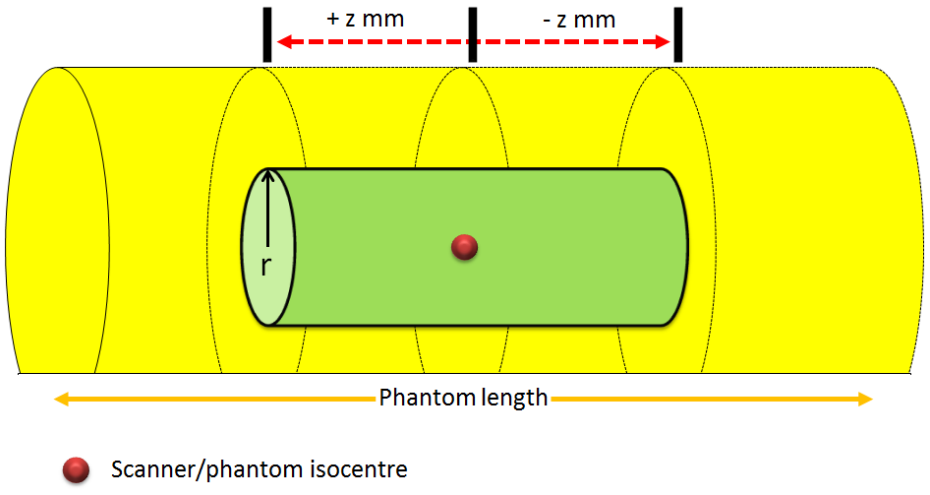

Figure 5.6: Schematic defining the volume variations for distortion analysis. All measurements were performed within a given distance from the centre of the phantom in the through plane ($\pm$ z) and axial (r) directions.

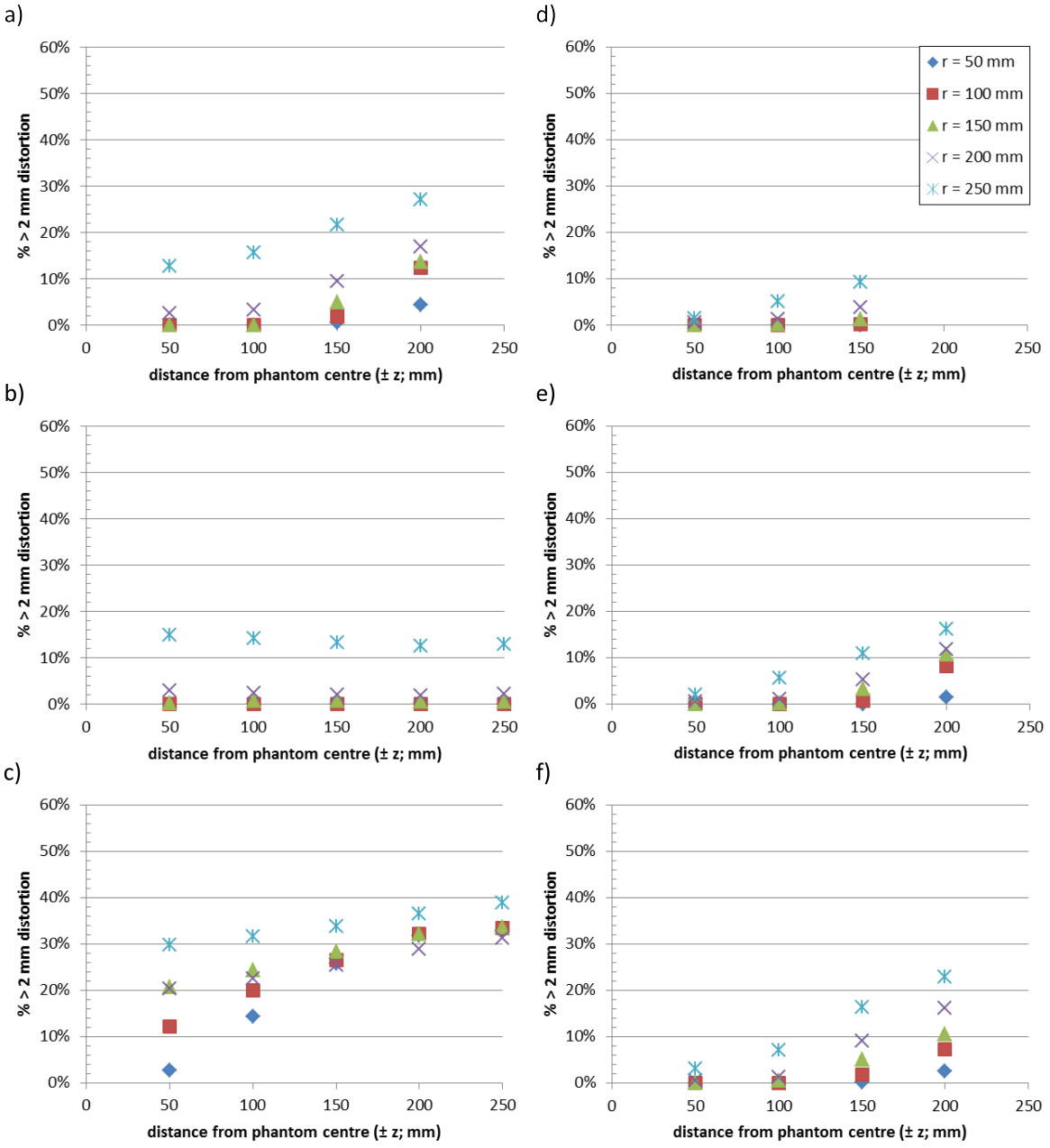

Figure 5.7: Normalised percentage of points within the imaged volume at a given distance from the centre of the phantom ($\pm$ z) for a given axial radial distance from the centre of the scanner (r) where the distortion is greater than or equal to 2 mm for the a) spoiled GRE Non TimCT, b) spoiled GRE TimCT at 1.1 mm/s table speed, c) spoiled GRE TimCT at 2 mm/s table speed, d) standard 2 mm SE, e) standard 3 mm SE and, f) 2 mm CISS sequences.

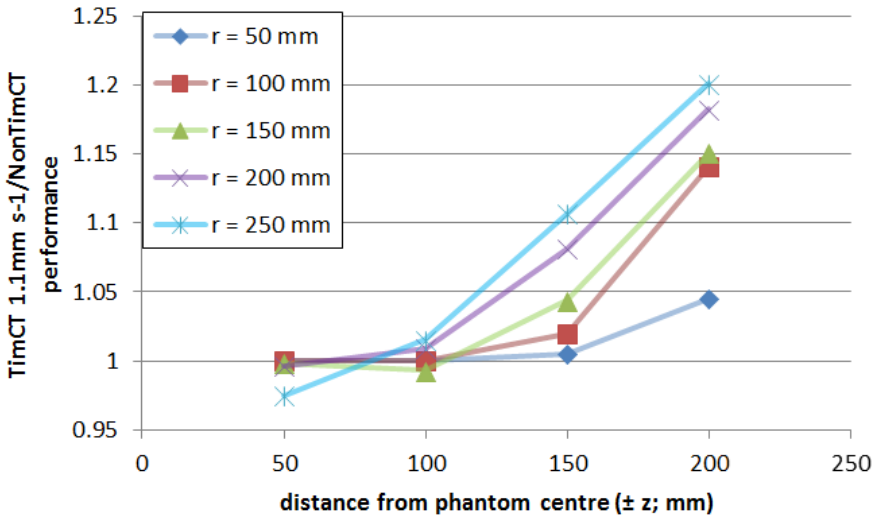

Figure 5.8: Ratio of the spoiled GRE regions where distortion < 2 mm for images acquired with TimCT at 1.1 mm/s and with a static table (TimCT/Non-TimCT). Values greater than 1 indicate the TimCT sequence performed better geometrically

5.4 Discussion

The distortion distributions observed in Figure 5.2 highlight the optimisation characteristics of the scanner utilised. When looking at the gradient component of distortion, the distortion magnitude is worse at the superior-inferior edges of the FOV where the gradient field linearity declines due to the short bore size. The B_0 field components show that this effect is worse axially around the bore edges as opposed to the through plane edges. This highlights the cylindrical nature of the magnet used in this new scanner and emphasises the need for QA on each specific system. It should be noted that B_0 inhomogeneity is a more crucial component when imaging certain patient anatomy (e.g. sinuses within the head), creating regional variations on top of the system effects described here. In clinical acquisitions appropriate steps should be taken to address this including further increasing the bandwidth, more localised volumetric shimming and even considering B_0 correction. Choice of appropriate MRI protocols [3, 81] within a department is an important part of this process.

Comparison of the static image acquisitions in table 5.3 highlights the difference in 2D and 3D vendor correction algorithm application. During image acquisition, the SE and CISS sequences only permitted 2D correction application while the 3D correction could be applied to the spoiled GRE. For the SE and CISS sequences, retrospective 3D correction could be

performed. This highlights a practical limitation that may be encountered during imaging as well as emphasising the importance of knowing the capabilities of each system, both on and offline. Since the 2D correction algorithm does not consider the slice selection direction, through plane distortions are not taken into account. As expected, the geometric performance of sequences acquired with the 2D algorithm applied was poorer than the 3D corrected images in which distortion is considered in all 3 axes. This resulted in an improvement of the percentage of the phantom volume where distortions were within 2 mm of 15%, 24% and 19% (absolute percentage coverage) for the 2 mm SE, 3 mm SE and CISS sequences respectively. Distortions greater than 2 mm were not observed within a radial distance of 148 mm from isocentre. For radiotherapy purposes, the highest order correction algorithm available should be applied. Restrictions in scanner and sequence capabilities in applying these corrections indicate more potential improvements could be made towards MRI scanning options for the purposes of RTP.

The moving table option offered with TimCT acquisition provided a significant increase to the field length that can be imaged compared to static table acquisition (table 5.3; Figures 5.4 and 5.7). The vendor quotes the TimCT option allows for imaging with field lengths of 205 cm. It was tested to 50 cm in this study which encompassed the length of the phantom and exceeded the maximum scan length limits of static table acquisition.

Of the sequences investigated, TimCT acquisition with a table speed of 1.1 mm/s performed the best geometrically. However this came at the cost of time. Acquisition time for the TimCT 1.1 mm/s was 9 minutes, 30 seconds, 3.5 times greater than that of the static table acquisition for the same spoiled GRE sequence (2 minutes, 41 seconds to image the whole phantom). While that resulted in increased image scan length and distortion improvement at superior and inferior regions of the image, the additional scan time could lead to increased patient movement and associated artifacts within the image, potentially reducing its benefit for RTP. Time variations are also subject to the desired imaging sequence. For example, TimCT at 1.1 mm/s with the spoiled GRE resulted in an improved acquisition time when compared to the static table SE sequences (14 minutes, 40 seconds), the latter with scan lengths of only 47-68% that of the spoiled TimCT GRE.

However with TimCT, an additional source of error is introduced with the through plane table movement. This is evident when comparing the 1.1 mm/s and 2 mm/s table speeds (Figure 5.4 b, c; Figure 5.7 b, c). Through plane movement results in blurring of the capsules

and an increase in the severity of the gradient nonlinearity distortions across all 3 imaging planes. This effect worsens with increasing distance from the isocentre of the scanner due to the increased gradient nonlinearities, as discussed for blood vessel imaging in MRA by Polzin et al. [119].

Table movement amplifies the system distortions and manifests as blurring within the image. Since these distortions are larger at the outer edges of the FOV, blurring is worse in these regions with the effect minimal in the central FOV. With TimCT acquired at 1.1 mm/s, blurring resulted in an increase in apparent capsule volume of 43 $\pm$ 5 % ($\pm$ 2 standard deviations) at r = 225 mm from scanner centre and 95 $\pm$ 8 % at r = 240 mm. Blurring increased with table speed with the 2 mm/s TimCT average capsule volume increasing by 93 $\pm$ 1 % and 170 $\pm$ 5 % at r = 225 and r = 240 mm, respectively. Increasing the table speed from 1.1 mm/s to 2 mm/s resulted in a 26% increase in the percentage of grid points experiencing distortions greater than 2 mm. While TimCT at 2mm/s permitted a reduction in maximum distortion and a more regular distortion pattern compared to the static table acquisitions, it performed worst in the distance from isocentre where distortions greater than 2 mm became observable. Distortions became greater than 2 mm beyond a radial distance of 55 mm from phantom centre. This corresponded to the maximum distance from scanner isocentre that an image could be acquired at that speed.

Figure 5.8 indicated regions for the best geometric performance between the static and 1.1 mm/s TimCT image acquisitions. When imaging within a small radius from isocentre with a short scan length, the two techniques perform similarly, with the Non TimCT acquisition performing slightly better for a larger scan length. As the scan length increased beyond $\pm$ 100 mm from phantom centre, the TimCT sequence was found to perform best for all radial distances investigated. This is dependent on the table speed. When the table speed was increased to 2 mm/s, the static sequence performed geometrically better, though it was not able to image the whole phantom. This information is useful when determining what acquisition technique to use for the purposes of RTP, given the anatomy of interest, the FOV required and the role of the MRI data. For example for centrally located anatomy, such as brain, head & neck or when deliberately using a small FOV (e.g. prostate) to subsequently register to CT, static acquisition may be sufficient. As indicated in Figure 5.7, if imaging over a distance of $\pm$ 100 mm from the phantom centre, the static image and TimCT at 1 mm/s perform very similarly, with distortions greater than 2 mm increasing beyond a radial distance of 200 mm from the scanner centre. In other instances where extended z

coverage is warranted or anatomically suited (e.g. peripheral sites, lung etc.) then a moving table strategy may be important. Figure 5.7 highlights the potential use of TimCT for this purpose. At 1 mm/s, the percentage of points experiencing more than 2 mm distortion remaining constant over the whole phantom volume, compared to the static case where the whole volume could not be imaged and the distortion increased with increasing distance from the phantom centre. Although TimCT is currently a vendor specific implementation, this work has shown advantages in repositioning anatomy rather than simply extending the image volume which should be considered on other systems using stepping table variations. This paper served to highlight the geometrical variations that these techniques manifest and emphasises the importance of understanding the limitations of MRI acquisitions.

TimCT scans acquired with table speeds greater than 2 mm/s were investigated. These were not analysed however, with capsules towards the outer edge of the phantom in axial slices becoming severely blurred and displaced. Some of these points were no longer observable in the image and the analysis process would not have been able to account for the loss of information. Increasing the table speed was done at the expense of the slab length imaged as the table moved through the scanner. Faster table speeds were therefore susceptible to additional blurring due to the movement as well as increased gradient nonlinearity effects due to an imaging area extending further from isocentre.

One of the limitations of the study was the performance of the registration algorithm at high distortion regions at the FOV edges in the static acquisitions. The registration performed well in central regions of the phantom where no grid point information was lost. Outside the convergence region of the registration algorithm, the image contrast is not sufficient and thus the algorithm merely extrapolates the transformation. This was apparent from visual inspection. Distortion values greater than 2 mm were assumed for regions of the phantom that could not be imaged with static acquisitions and the regions in which the registration algorithm failed. Because the distortion patterns were more regular throughout the whole imaging volume for the TimCT scans and there was no field limitations resulting in a loss of capsule visualisation, the registration algorithm was not found to fail for these images.

The ability to change imaging parameters from the default sequence setting for TimCT was more restricted than the static spoiled GRE acquisition option. Of particular note for this study were the slice thickness options available and the restrictions this put on table speed options. As a result, the slice thickness of 5 mm investigated for this sequence was larger

than the 2 mm generally used for treatment planning on CT. TimCT was also limited to 2 acquisition sequences, the spoiled GRE and a single shot turbo spin echo (TSE) sequence. The TSE sequence was scanned during preliminary data collection however the SNR on the phantom images was too low for the purposes of image analysis.

Static or moving table MRI acquisition for RTP would need to be assessed based on the application. Both techniques could be useful in providing supplementary information to planning CTs. Static images can provide the geometric information required, particularly over anatomical regions extending over a shorter scan length. In some cases, TimCT would be required to ensure adequate scan length coverage, particularly if dealing with long OARs or target volumes. The same argument could be used for their application in MR-only planning.

5.5 Conclusion

The capability of the designed phantom to be imaged over a large FOV is highlighted in this chapter. Measurements made with both static and moving table acquisitions demonstrated variations in the achievable geometric accuracy with each technique. The moving table technique (TimCT) was shown to extend the distortion free volume of the phantom by continuously acquiring data from a small section around the scanner isocentre. There are a number of limitations to this procedure including choice of available pulse sequence and effects of increasing table speed. However, this work illustrates the nature of MRI distortions, demonstrating geometric variations that can occur between image acquisition techniques (as opposed to sequence variations alone) which is not well known in the RT community. It is important to fully characterise an individual MRI system and use this knowledge to select the most suitable imaging protocol for radiotherapy treatment planning.

Chapter 6

Distortion implications for whole breast IMRT

6.1 Introduction

With the growing interest in the utilisation of magnetic resonance imaging (MRI) for radiotherapy treatment planning [92, 96], the geometric distortions associated with MRI require consideration [3]. Distortions due to nonlinearities in the gradient coils and inhomogeneities in the B_0 field increase in magnitude with increasing distance from the MRI isocentre [Chapter 5]. The patient introduces additional effects such as chemical shift and susceptibility due to the variations in magnetic properties of different tissues. Although the implementation of vendor supplied distortion correction algorithms can reduce the system related distortions, they are not completely removed [Chapter 3]. Several methods can be utilised to correct for patient-specific distortions including acquiring two images with reversed gradient direction [101] and B_0 mapping [122], however clinical implementation of these can be challenging and is not routinely implemented [3]. Acquiring images with a high imaging bandwidth (BW) can be used to minimise the distortions due to chemical shift and magnetic susceptibility. However increasing the imaging BW creates a reduction in the signal-to-noise ratio (SNR) and increasing the BW required to remove these effects completely from the images are detrimental to the image quality and the usefulness of the images [65].

[1]Part of this chapter has been submitted for publication:
Walker A, Metcalfe P, Liney G, Batumalai V, Dundas K, Glide-Hurst C, Delaney G, Boxer M, Yap ML, Dowling J, Rivest-Henault D, Pogson E, Holloway L. MRI geometric distortion: Impact on tangential whole breast IMRT. *Journal of Applied Clinical Medical Physics*, **(In Submission)**

Investigations into the dosimetric impact of MRI geometric distortions on the radiotherapy treatment planning (RTP) process have been conducted for brain and prostate patients. Brain studies focus on a small field of view (FOV) at the centre of the scanner where distortions are minimal [32, 97]. The prostate studies were conducted on low magnetic field strength scanners [73, 98], or on phantom geometry [77]. Prott et al. [100] suggested that these effects may be of major relevance to breast cancer treatment, where the anatomy extends out into regions of higher geometrical inaccuracies.

It is estimated that 83% of breast cancer patients should undergo radiotherapy as part of their treatment [123]. A number of techniques are available for treating breast cancer with external beam radiotherapy. These include Three-Dimensional Conformal Radiotherapy (3D-CRT), Intensity Modulated Radiation Therapy (IMRT) [124], hybrid methods combining 3D-CRT and IMRT techniques [125], and Intensity Modulated Arc Therapy (IMAT) [126]. Whole breast radiotherapy sees the whole breast volume irradiated after breast conserving surgery. Partial Breast Irradiation (PBI) involves only the tumour or lumpectomy cavity being irradiated, in order to spare surrounding healthy tissues.

The aim of the current study was to investigate the effect of MRI geometric distortions on the dose distribution on tangential whole breast IMRT. The impact of residual system distortions alone was compared for two different scanners with different field strengths and configurations. The influence of the combined distortion arising from the system and the patient was also investigated on the higher field strength system.

6.2 Methods

6.2.1 Phantom data

System distortion maps were obtained from two separate MRI scanners with different configurations and field strengths using specific phantoms.

The novel 3D phantom developed in Chapter 4 was was scanned on a closed, wide-bore 3 T Siemens Magnetom Skyra (Siemens Medical Systems, Erlangen, Germany). A 2D T2 spin echo sequence (voxel size 1.56 x 1.56 x 2 mm^3, 500 x 500 x 252 mm^3 FOV, 445 Hz/pixel, TE/TR/flip angle 12 ms/2760 ms/90^o was used with a vendor supplied 2D correction algo-

rithm applied. A corresponding CT of this phantom was acquired to provide the undistorted geometry of the phantom.

For the 1.0 T Panorama high-field open vertical-bore system (Philips Medical Systems, Best, The Netherlands), a vendor-supplied 3D distortion phantom consisting of docusate sodium capsules within a foam structure [70] was scanned using a 3D T1 spoiled gradient echo sequence (voxel size 0.938 x 0.938 x 2 mm^3, 450 x 450 x 400 mm^3 FOV, 385 Hz/pixel, TE/TR/flip angle: 3.77/30 ms/60^o, 3D correction algorithm applied). A corresponding CT of this phantom was acquired.

6.2.1.1 Quantification of residual systematic distortions: phantom study

To quantify systematic distortions, the CT and MR phantom images from each scanner were registered. A robust rigid registration method [120] was applied to compensate for changes in position between modalities, then a deformable multi-scale (4 levels) B-spline registration algorithm [121] was used to account for non-linear MRI deformations. To promote smoothness, the spacing of the final B-spline control point grid was adjusted by selecting the largest value that would allow accurate alignment of the phantom markers post-registration, as determined by visual assessment. We identified 25 mm and 10 mm as the best spacing parameters for the Skyra and the Panorama images, respectively. The registration results were manually validated by verifying that the phantom markers were accurately aligned [Chapter 5].

6.2.2 Patient data

Datasets for 18 patients who underwent whole breast external beam radiotherapy (12 right sided, 6 left sided) were obtained. Patients were positioned on both CT and MRI using the same treatment simulation set-up on a flat table and in a head first supine position. Non-contrast CT images were acquired on a Philips Brilliance Big Bore scanner (Philips Health Care, Cleveland, OH) (voxel size 0.98 x 0.98 x 2 mm^3, 500 x 500 mm^2 FOV). The MRI was acquired on the aforementioned 3T MRI scanner for comparison with the acquired phantom images. A 2D T2 TSE was acquired with 2 mm slice thickness and an axial square pixel size ranging from 0.52-0.59 mm^2. The FOV ranged from 400 x400 mm^2 to 450 x 450 mm^2 (depending on patient size) with TE/TR/flip angle: 88 ms/5840 ms/167^o. Images were prospectively corrected using the vendor-supplied 2D gradient distortion correction

algorithm. In order to investigate the effects of BW, patients were acquired with either a pixel BW of 230 Hz/pixel or 450 Hz/pixel.

Clinical target volume (CTV) and seroma volumes for each patient were contoured by an experienced radiation oncologist based on the CT images. Lung, heart, contralateral breast and external patient volumes were contoured by an experienced senior planner.

6.2.2.1 Quantification of residual systematic and patient-induced distortions: patient study

Distortion maps representing the combined residual systematic and patient-induced distortions were estimated by registering the patient CT images with the corresponding patient MRI (Skyra only). The registration process used for the phantoms image was also used for the patient data, but with a final control point grid spacing of 15 mm, which was found to give adequate accuracy at a realistic smoothness level. Each registered image was visually assessed for accuracy, with particular focus around the breast and chest wall regions.

6.2.3 Image distortion

To investigate the impact of MRI geometric distortion, each patient CT (and the corresponding contours) was distorted in 3 ways using the phantom-computed distortion maps (Skyra and Panorama) and using the combined systematic and patient-induced distortion maps (Skyra only) (Figure 6.1). The phantom data allowed investigations on the potential dosimetric variations between MRI scanners of different configurations in whole breast RTP without the added complexity of patient-induced effects. With the 3T, using both phantom and patient based distortion maps allowed for a comparison between the system-related only and combined system and patient-related effects.

In all cases, contour variation was assessed for CTV, seroma, contralateral breast, combined lung and heart volumes. The Dice similarity coefficient (DSC) was obtained between original and distorted contours to investigate their overlap (equation 6.1):

$$DSC = 2 \times \frac{\text{intersection volume}}{(\text{original contour volume} + \text{distorted contour volume})} \tag{6.1}$$

Original and deformed contour sizes were also computed.

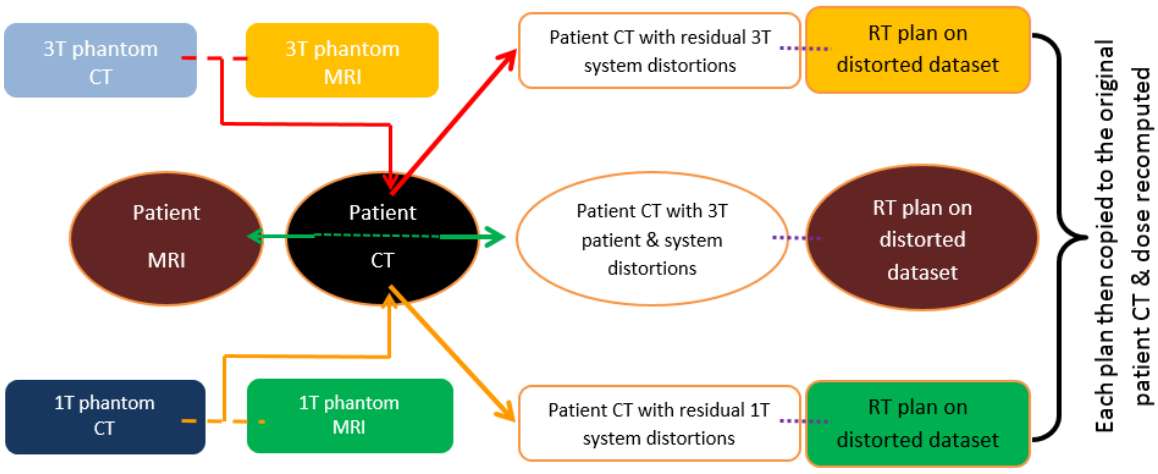

Figure 6.1: Methodology schematic showing the image distortion processes and the resulting images.

6.2.4 Treatment planning

After registration, four different CT datasets were considered (Figure 6.1):

1. The original CT,
2. A CT dataset deformed by the Skyra residual system distortions (phantom measured),
3. A CT dataset deformed by the Panorama residual system distortions (phantom measured) and,
4. A CT dataset non-rigidly registered to the patient geometry on the Skyra.

For each of the simulated CT datasets, tangential whole breast plans were generated to a prescription of 50 Gy in 25 fractions in accordance with standard clinical protocols. Inverse planned IMRT plans were created using an automated script in Pinnacle Version 9.6 (Philips Radiation Oncology Systems, Milpitas, CA), which established a gantry angle and determined field size and beam modulation. Beam angles with an isocentre located at the centre of the Planning Target Volume (PTV) (defined as an expansion of the Clinical Target Volume (CTV) of 1cm superior-inferior, 0.5 cm left-right and 0.5cm anterior-posterior) were automatically determined based on the location of the lungs, PTV and contralateral breast contours. Beam angle was manually adjusted until it was deemed to be ideal for the shape of a particular patient. After completion of the script, each plan was individually optimised

Table 6.1: The DVH criteria for plan evaluation (Based on RTOG guidelines and clinical experience).

Target/OAR structure	*Ideal criteria*	*Acceptable criteria*
PTV	> 95% receives > 47.5 Gy	$\geq$ 95% receives $\geq$ 45 Gy
	Maximal 1 cc $\leq$ 53.5 Gy	Maximal 1 cc $\leq$ 55 Gy
Seroma	> 99% receives > 47.5 Gy	> 99% receives > 46 Gy
	Maximal 1 cc < 55 Gy	Maximal 1 cc < 57.5 Gy
Combined Lung	< 10% receives 10 Gy	< 10% receives 10 Gy
	Mean dose < 10 Gy	Mean dose < 10 Gy
Ipsilateral Lung	< 15% receives > 20 Gy	< 20% receives > 20 Gy
Heart	Mean < 4 Gy	Mean < 5 Gy
Contralateral breast	Maximal 1 cc < 1.86 Gy	Maximal 1 cc < 3.10 Gy

by altering the appropriate IMRT optimisation parameters to achieve clinically acceptable Dose Volume Histogram DVH criteria [127] (table 6.1) and visual acceptance by an experienced senior planner. Qualitative visual assessment was conducted to confirm homogeneity of the dose distribution within the PTV, as well as ensuring high dose levels did not occur outside the PTV and that the maximum dose occurred within the PTV. After final optimisation, multi-leaf collimator (MLC) banks were shifted on appropriate beam control points, so that around 80% of the dose was planned to be delivered with 2 cm anterior overshoot.

6.2.5 Dosimetric evaluation

Once plans were optimised on each distorted dataset, the beams from these plans were exported and then imported onto the original CT image (Figure 6.2) with the beam isocentre placed at the centre of the undistorted PTV, simulating a treatment set-up position. Monitor units (MU), beam weights and dose grid resolution were kept consistent and recomputed on each distorted dataset, then the dose criteria were tabulated. Each of these plans was then assessed and given a pass or fail based on its ability to meet both DVH and visual acceptance criteria. Plans meeting the DVH and visual assessment criteria were generated on all 18 original (undistorted) CT images. This provided a baseline from which the distortion impact could be tested.

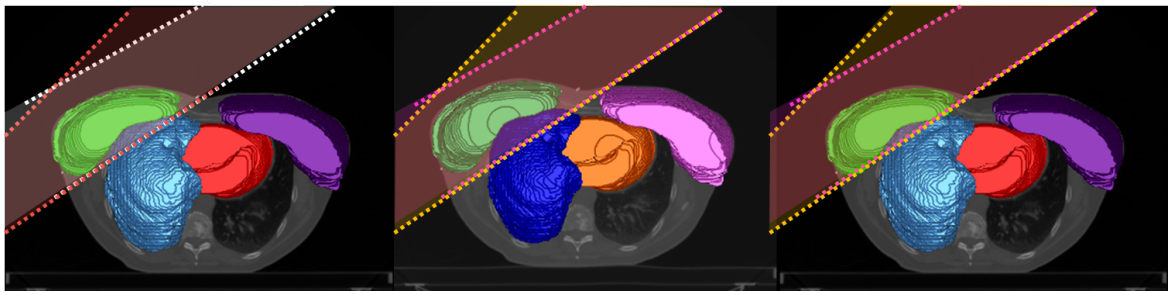

Figure 6.2: Workflow for the assessment of the geometric distortion on the planning process. Left: Plan optimised on original CT dataset; Centre: Plan optimised on distorted CT dataset; Right: Plan optimised on distorted CT dataset copied and recomputed on the original CT dataset.

6.3 Results

6.3.1 Scanner distortions

The maximum distortion on the Skyra was measured at 7.88 mm (mean = 2.07 mm; 95% of volume experienced distortions below 4.67 mm) over a 500 x 500 x 254 mm^3 FOV, with distortion on the Panorama reaching 11.87 mm (mean = 1.71 mm; 95% of volume experienced distortions below 4.56 mm) over a 475 x 380 x 420 mm^3 FOV. The largest distortions were observed at the FOV edges.

6.3.2 Contour deformation

The average size of contoured volumes is displayed in Table 6.2. The maximum distortion observed in each contour and the DSC overlap between distorted and undistorted contours is presented for each distortion type, averaged across all patients. Distortions observed in the patient distorted images were larger in magnitude than from the phantom alone measurements, as expected with the addition of susceptibility and chemical shift artefacts, setup and patient movement discrepancies. Distortion vector fields displaying where distortions $\geq$ 2 mm are shown in Figure 6.3 for all three deformations, relative to the contour locations. Maximum distortions for the patient measurements (Figure 6.3.b) were larger than the residual system distortions alone (Figure 6.3.a).

Table 6.2: Variations in the contour volumes and overlap comparisons between original and distorted contour volumes. Phantom data consists of systematic distortions while patient scans also include patient-specific distortions and setup uncertainties.

Scanner	*Contour*	*Mean undistorted volume ± 2σ (cm^3)*	*Mean maximum distortion ± 2σ (mm) within contour*	*Mean DSC ± 2σ for each contour*
Skyra	CTV (R)	796.0 ± 737.7	2.99 ± 1.18	0.972 ± 0.007
phantom	(L)	485.8 ± 641.3	2.60 ± 0.75	0.966 ± 0.009
	Seroma (R)	28.0 ± 87.2	1.03 ± 1.10	0.958 ± 0.081
	(L)	11.0 ± 16.0	1.21 ± 0.39	0.914 ± 0.119
	CB (R)	974.9 ± 774.6	3.73 ± 1.48	0.967 ± 0.006
	(L)	585.0 ± 515.5	2.90 ± 0.61	0.969 ± 0.006
	Combined Lung	2462 ± 1220	2.96 ± 1.34	0.981 ± 0.004
	Heart	477.6 ± 134.4	1.37 ± 0.60	0.990 ± 0.006
Pamorama	CTV (R)		2.87 ± 0.53	0.966 ± 0.011
phantom	(L)		2.45 ± 1.37	0.952 ± 0.021
	Seroma (R)		2.31 ± 0.45	0.964 ± 0.100
	(L)		2.01 ± 0.42	0.904 ± 0.069
	CB (R)		3.43 ± 1.18	0.957 ± 0.014
	(L)		2.80 ± 0.49	0.959 ± 0.018
	Combined Lung		4.87 ± 1.71	0.968 ± 0.007
	Heart	As above	2.01 ± 0.21	0.980 ± 0.009
Skyra	CTV (R)		5.90 ± 4.64	0.942 ± 0.023
patient	(L)		6.63 ± 6.90	0.914 ± 0.063
	Seroma (R)		3.70 ± 3.97	0.818 ± 0.192
	(L)		4.55 ± 4.20	0.744 ± 0.157
	CB (R)		6.44 ± 3.10	0.942 ± 0.023
	(L)		7.02 ± 4.38	0.914 ± 0.063
	Combined Lung		11.33 ± 8.63	0.929 ± 0.038
	Heart		9.12 ± 7.06	0.922 ± 0.054

Abbreviations: CB = Contralateral Breast; R = Right sided patient; L = Left sided patient; σ = standard deviation; DSC = Dice similarity coefficient

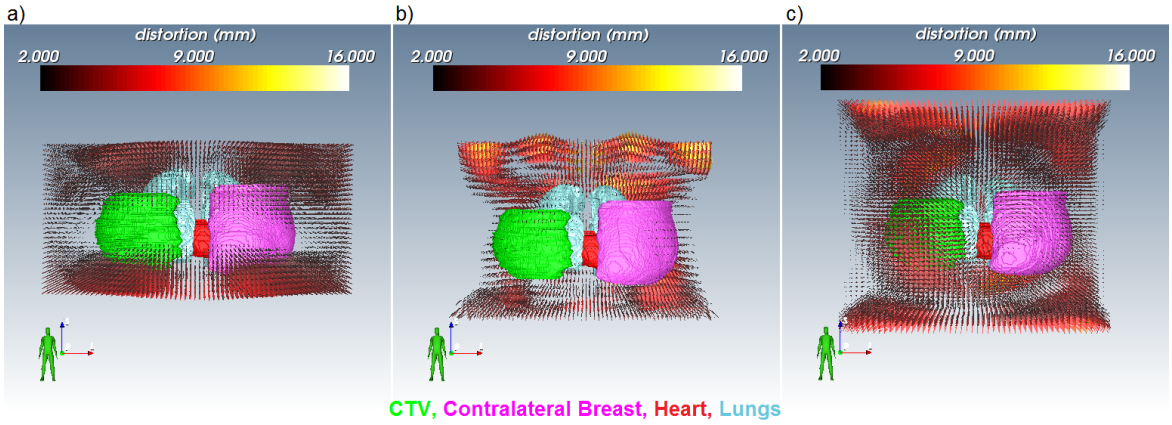

Figure 6.3: Coronal comparison of the CTV (green), contralateral breast (pink), lung (blue) and heart (red) volumes relative to distortions $\geq$ 2 mm for a) the Skyra phantom, b) an example Skyra patient dataset (incorporating patient and system related distortions as well as set-up uncertainties) and c) the Panorama phantom. Scales set relative to maximum distortion in b). Visualisation by http://smili-project.sourceforge.net/

6.3.3 Dosimetric impact

Mean variations in DVH criteria between distorted plans optimised on the distorted dataset compared to that of the distorted plan recomputed on the original datasets are shown in table 6.3. All plans optimised on both the Skyra and Panorama phantom distorted datasets passed both the DVH and visual assessment when recomputed on the original CT dataset. Of the 18 plans optimised on the CT datasets non-rigidly registered to the Skyra patient images, 4 right sided and 4 left sided patients failed the clinical tolerances when recomputed on the original dataset (2 failed DVH, 4 failed visual, 2 failed DVH and visual assessments). Three of the eight patients imaged at the higher BW resulted in plans with large dosimetric variations when recomputed on the original CT, rendering them clinically unacceptable. Figure 6.4 compares DVHs for two patient datasets for the combined Skyra distortions (with 1 passing and one failing), Skyra systematic and Panorama systematic distortions. Both patient images were acquired with a pixel BW of 450 Hz/pixel.

Table 6.3: Quantitative assessment of the DVH parameters and the clinical plan acceptance. All numbers were computed based on dose optimised on distorted datasets less dose when recomputed on undistorted dataset.

Dose criteria		*Mean difference ± 2 σ (Skyra phantom)*	*Mean difference ± 2 σ (Panorama phantom)*	*Mean difference ± 2 σ (Skyra patient)*
Right				
PTV	$V_{47.5\ Gy}$	0.17 ± 1.18 %	0.46 ± 1.77 %	0.32 ± 2.51 %
	Max 1 cc	-0.15 ± 0.25 Gy	0.00 ± 0.40 Gy	0.18 ± 0.70 Gy
Seroma	$V_{47.5\ Gy}$	0.08 ± 0.81 %	-0.09 ± 0.49 %	0.20 ± 1.72 Gy
	Max 1 cc	0.05 ± 0.23 Gy	0.21 ± 0.35 Gy	0.13 ± 0.84 Gy
Ipsilateral lung	$V_{20\ Gy}$	-0.13 ± 0.38 %	-0.48 ± 0.86 %	0.77 ± 2.72 %
Heart	Mean	0.03 ± 0.27 Gy	-0.02 ± 0.14 Gy	-0.01 ± 0.28 Gy
CB	Max 1 cc	-0.03 ± 0.10 Gy	-0.06 ± 0.30 Gy	0.10 ± 0.57 Gy
Left				
PTV	$V_{47.5\ Gy}$	-0.82 ± 1.16 %	0.28 ± 1.43 %	-0.73 ± 1.93 %
	Max 1 cc	-0.02 ± 0.08 Gy	0.03 ± 0.15 Gy	0.45 ± 0.99 Gy
Seroma	$V_{47.5\ Gy}$	-0.50 ± 1.56 %	-0.47 ± 2.00 %	-0.35 ± 1.68 %
	Max 1 cc	-0.18 ± 0.61 Gy	-0.02 ± 0.23 Gy	0.20 ± 0.87 Gy
Ipsilateral lung	$V_{20\ Gy}$	-0.18 ± 0.53 %	0.25 ± 0.58 %	-0.30 ± 1.81 %
Heart	Mean	0.13 ± 1.34 Gy	-0.08 ± 0.20 Gy	-0.38 ± 0.85 Gy
CB	Max 1 cc	-0.03 ± 0.10 Gy	-0.1 ± 0.20 Gy	0.33 ± 2.36 Gy
Combined lung	$V_{20\ Gy}$	-0.06 ± 0.23 %	-0.14 ± 0.43 %	-0.09 ± 0.68 %
Plan pass/fail	Overall	18 ✓ / 0 ✗	18 ✓ / 0 ✗	10 ✓ / 8 ✗

Abbreviations: CB = Contralateral Breast; ✓ plan met acceptance criteria, ✗ plan did not meet acceptance criteria

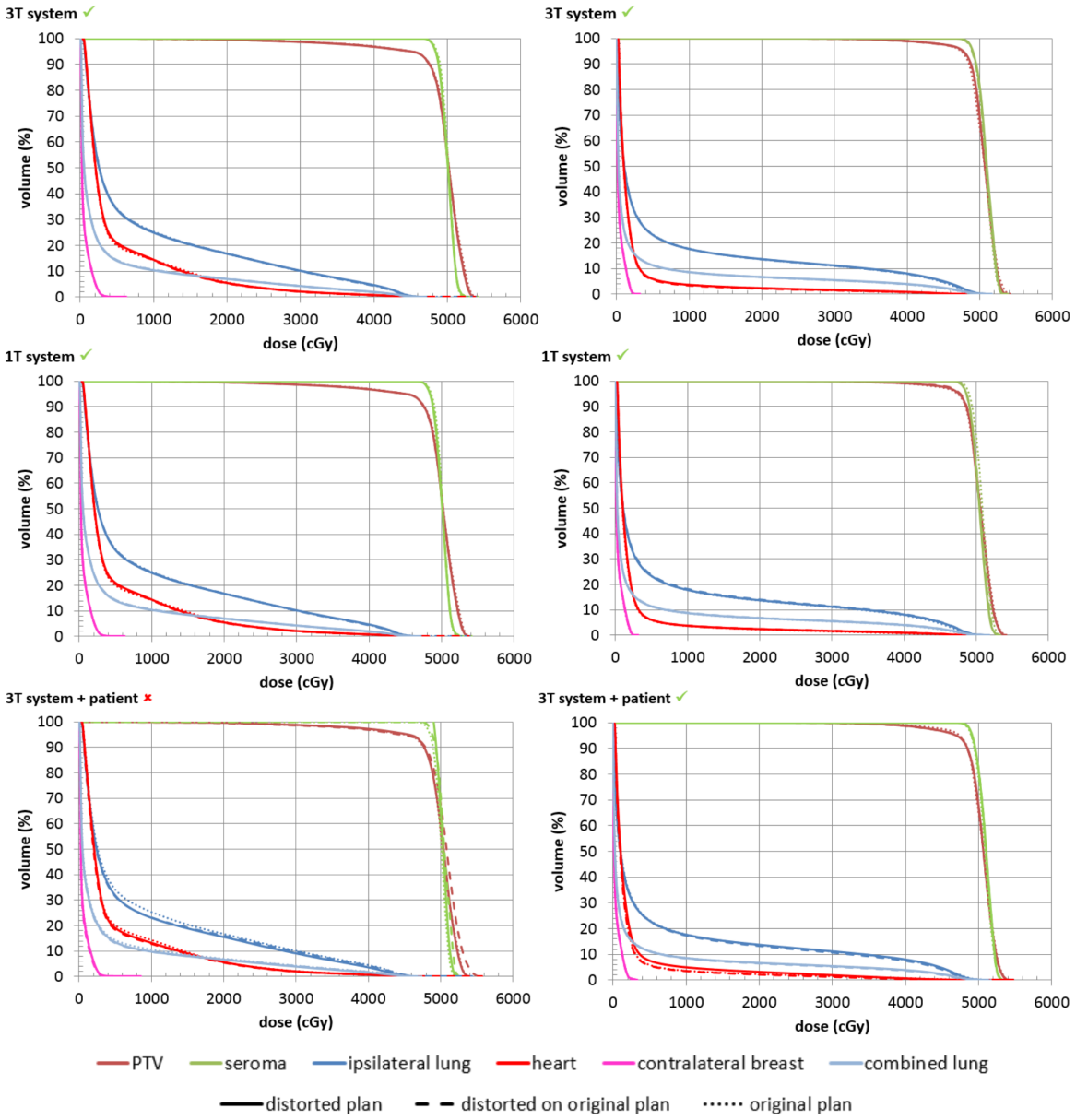

Figure 6.4: DVHs for 2 patients showing the variation in dose coverage between the different distortions assessed. ✓ plan met acceptance criteria, ✗ plan did not meet acceptance criteria.

6.4 Discussion

The assessment of the dosimetric impact of geometric distortion in this study (Figure 6.1) considers the following:

1. How are plans currently being generated? (Plan optimisation on correct CT geometry)
2. What would happen if we were to plan on MRI geometry? (Plan optimisation based on incorrect geometry)
3. How does this translate into what is actually being treated? (Incorrect geometry optimisation recomputed on the correct geometry)

In distorting the CT datasets to match the MRI geometry as measured by both phantoms and patients, it was possible to assess the distortion impact from system related distortions and patient effects without the added question of the impact of the assignment of electron density to various tissue types.

Systematic geometric distortions remaining after the application of vendor supplied correction algorithms differ between MRI scanners. Results have shown that residual system distortions can vary greatly between two different scanners, both utilised for RTP simulation. However, the effect of these distortions alone was found to have minimal impact on photon dosimetry. Residual systematic distortions combined with patient related distortions (including patient set-up) potentially have a larger impact on dosimetric variation, requiring consideration if utilising patient geometry as observed on MRI in the radiotherapy planning process.

Most modern scanners come with the option to apply geometric correction algorithms to account for the gradient nonlinearities in 2D and/or 3D. Though distortions may not be completely removed, a reduction in systematic distortions is visible when applying the 2D correction over no correction [Chapter 3], and when applying the 3D correction over the 2D correction [Chapter 5]. Patient MRIs were acquired with a vendor supplied 2D correction algorithm as the 3D correction was unavailable at commencement of patient imaging. Maximum distortions on the Skyra with the 3D correction algorithm applied are reduced from 7.88 mm to 4.08 mm. However, images corrected using the 2D algorithm provide a

"worst case" scenario and the dosimetric impact from application of the 3D correction can be expected to be smaller.

Both the wide, closed bore 3.0 T Skyra and the vertical, open bore 1.0 T Panorama performed similarly in terms of dosimetric impact when looking at the residual system distortions as determined by phantom measurements. Despite the known increase in gradient nonlinearity distortions with increased distance from isocentre, residual distortions of laterally positioned breasts did not adversely impact dosimetry. Maximum distortion values observed within contoured regions for the Skyra patient distorted datasets were on average 3.8 times greater than those corresponding to the phantom data alone, indicating that the patient-induced distortions (and associated set-up errors) were larger than that of the residual system distortions.

Datasets incorporating both patient and system related distortions were found to have greater dosimetric impact than the residual system distortions alone. On average, plans generated on patient distorted images were more inhomogeneous with increased hot and cold regions when recomputed on the original CT geometry. The probability of a distorted plan passing or failing did not correlate with laterality, extent of contour distortion, patient size or pixel bandwidth. Placing a patient within the magnetic field leads to geometric distortions arising from chemical shift and susceptibility artefacts. These effects are the result of variations in the magnetic properties of tissues within the body. This is an issue for breast imaging where there are interfaces between glandular tissue, fatty tissue, muscle, ribs and lungs. The chemical shift due to difference in water and fat signals is 440 Hz at 3 T (220 Hz at 1.5 T), resulting in field perturbations of 3.5 parts per million (ppm). Field perturbations due to susceptibility between different tissues can be as large as 6 ppm [3]. Increasing the BW further could have benefit in reducing the susceptibility effects, though this would come at the expense of the SNR which may limit clinical utility.

These findings vary from investigations on the prostate and brain, where system and patient distortions were not found to have a significant impact on dosimetry [73, 98, 99]. However, these studies were conducted on scanners of lower field strengths. Additionally, these sites generally have smaller air-tissue interface regions near the target. The combined distortion effects were investigated on a 3.0 T magnet for this study, which has higher susceptibility variations than lower strength systems [128]. Differences may also be due to the peripheral location of the breast, resulting in less complicated treatment beams and organs requiring

sparing.

While vendor supplied distortion corrections are essential to minimise the dosimetric impact of system related distortions, our results suggest that patient correction methods may play a role in reducing the dosimetric impact of geometric distortions on the planning process. Techniques such as B_0 mapping [122] or the acquisition of 2 images of reversed frequency encode direction [65] that could reduce patient susceptibility effects will be investigated in future work.

Due to the retrospective dataset utilised for this study, there was no way to separate the errors due to the patient distortion and those from setup variations. As such, a number of techniques were utilised to minimise the impact of any setup errors on this study. MRI and CT images were acquired on the same day to reduce variations due to changing patient anatomy over time. The patient CT and MRIs were rigidly registered prior to deformable registration to reduce setup errors to within the tolerance values to minimise dosimetric variations. Systematic and random setup errors for whole breast radiotherapy have been reported as 1-2 mm and 2-3 mm respectively [129]. Harron et al. reported that for translational shifts of 5 mm would result in a less than 5% variation in the target volume receiving 95% and 107% of the prescribed dose [130]. DVH variations across all three datasets within our study were less than these reported setup values. The hybrid IMRT technique utilised for this study (80% dose through open beams, 20% dose through IMRT beams) has also been found to the most be robust treatment technique when dealing with setup errors for whole breast radiotherapy [129, 131].

The image registration presents another potential study limitation since the plans are being generated on manipulated images and structures. The registration accuracy was within a voxel size within the chest region of interest. When registering the patient CT and MRIs, there were some differences around the patients' arms due to slight positional variations. Since these were well out of the dose calculation region, these variations were not considered. Image registration is also a point of consideration when utilising both CT and MRIs in the planning process [92].

The automatic beam angles generated on the distorted datasets were the same between the original plan and the Skyra residual distortion plans. The beam angle varied from the original in 7 of the patient distorted plans and 4 of the Panorama distorted plans by 1-4^o. Of the

patient distorted plans with varied beam angles, only one resulted in a plan which was not considered clinically acceptable once recomputed on the original, resulting in a hotter plan with more lateral dose.

The isocentre of all beams corresponded to the centre of the PTV. Matching the beams isocentre to the centre of the PTV represents a likely clinical scenario. While the presence of distortion changes the location of the centre of PTV and consequently the beam isocentre shifts relative to an undistorted geometry. If MRI-only planning was being utilised then this represents what would happen between the planning and treatment stages due to the variations in geometry.

Distortion mitigation must be addressed if moving towards MRI-only planning where a patient CT would not be available for reference. Although our results showed the influence of the scanners alone had minimal impact, it is important to quantify the geometric accuracy of each system. This is especially important for future MRI-linac treatment units where magnet and gradient specifications will be worse, as well as on higher field strength systems where the patient effects may be more problematic.

These results are specific to whole breast IMRT treatments. While breast treatment volumes extend into FOV regions where geometric distortions are largest, the dosimetric impact from residual system distortions alone appear small. Since breast is a relatively homogeneous tissue structure, the photon interactions may be more forgiving of these geometric variations. In anatomical sites with multiple structures, the dosimetric impact of residual distortions may be larger due to more complex planning methods and tissue variations. A similar investigation looking at partial breast radiotherapy would provide a good comparison to the whole breast scenario. In a partial breast treatment, the dosimetric impact may be increased with smaller treatment volumes and more targeted fields. Investigation into the combined effects of patient and systematic distortions require further investigation on the 1.0T Panorama open-bore.

6.5 Conclusion

Combined MRI systematic and patient related distortions can result in unacceptable dosimetric variations for whole breast IMRT if considering MRI-only radiotherapy treatment

planning. Residual system distortions alone had minimal impact on the dosimetry variations for 2 different scanners of differing configurations and field strengths. Improved methods to account for patient specific distortion may be beneficial to minimise dosimetric variations if using MRI alone in the treatment planning process.

Chapter 7

Summary and future work

The use of MRI for radiotherapy treatment planning is increasing. MR images have superior soft tissue contrast compared to CT and provide substantial benefits in radiotherapy: for staging, tumour delineation, image guidance and treatment response. This thesis presents a study into the geometric distortions on clinical MRI scanners to be used for RTP and the implications for whole breast radiotherapy treatment planning.

7.1 Quantifying MRI geometric distortion utilising a 2D phantom

Chapter 3 quantified the geometric distortions on four different diagnostic MRI scanners using a diagnostic 2D QA phantom. The results showed varying geometric distortions on each scanner, with the distortion increasing in magnitude further out from the isocentre of the magnet. On each scanner, the distortion distribution varied slightly between spin echo and gradient echo image acquisitions.

Research questions:

What are the variations in geometric distortion when scanning with and without the application of a vendor supplied 2D correction algorithm?

The application of vendor supplied 2-dimensional correction algorithms reduces the

magnitude of geometric distortions. While the maximum and mean distortion values were reduced, they were not completely removed. For a 3D turbo spin echo sequence, the maximum distortion observed beyond a radial distance of 100 mm from the isocentre was reduced from 4.4 mm to 2.8 mm. However, the maximum distortion was greater for the image with the correction algorithm applied within a 100 mm radial distance (i.e. the correction algorithm provided no benefit within this region). Similarly, the mean distortion within 100 mm from isocentre increased by 10% with the correction algorithm applied.

The correction algorithms applied in this section only work to correct for distortions in a 2D imaging plane. The third imaging plane, corresponding to the determination of individual image slices were not corrected for.

What is the magnitude of geometric distortions corresponding to the location of common radiotherapy anatomical sites within the scanner?

The largest distortions were observed in the peripheral regions within the scanner where the lung and breast are likely to lie. Additionally, the patient contour should also be considered in these regions too, which is important when considering the dosimetric impact. In central axial slices of the scanner, systematic geometric distortions within the brain stem, cervix, prostate and larynx are likely to be below 1 mm.

What are the limitations when using a 2 dimensional diagnostic imaging phantom for measuring distortion for radiotherapy treatment planning purposes?

The phantom dimensions were a limiting factor in being able to quantify the MRI distortions across a large field of view, as would be required for the purposes of RTP. The size of the grid component within the studied phantom was only 277 mm x 277 mm x 25 mm, limiting the capability of the phantom to encompass a large FOV. The 2D grid pattern meant that distortions could only be quantified at one location at a time and any phantom movement would be manual.

7.2 Design & construction of a full field of view 3D MRI distortion phantom

In Chapter 4, potential designs for a 3D MRI phantom for quantifying system related geometric distortions were investigated. A number of prototypes were developed and tested before the final phantom was designed.

Research questions:

What specifications are required for a full field of view phantom for MRI distortion assessment for radiotherapy planning?

The ideal specifications identified for a MRI distortion phantom, appropriate for determining system related distortions for the purposes of radiotherapy were:

(i) An MRI compatible design

(ii) Grid points localised in all 3 imaging planes

(iii) Capable of quantifying geometric distortions across a large FOV

(iv) Practical design

(v) Visualisation of the 3D grid points both CT and MRI for the purpose of image analysis and distortion quantification.

Is the designed phantom appropriate for measuring distortion for RTP?

The phantom developed in this study met the ideal phantom specifications. By design, the materials utilised were all MRI compatible. The offset locations of the vitamin E capsules between adjacent phantom layers provided an environment in which 3D grid points could be readily defined. While the capsules are longer in length (19 mm) than they are in diameter (8 mm), they could still be localised in all 3 imaging planes and this dimension ratio minimised the susceptibility artifacts from the capsules

themselves. The overall phantom had a diameter of 500 mm, height of 350 mm and a length of 513 mm, encompassing the entire imaging FOV on a 70 cm closed bore scanner. This made it adequate for quantifying geometric distortions across the full imaging FOV as required for RTP. While the phantom weighed approximately 60 kg, a grid phantom of similar dimensions and filled with liquid encased in a perspex box would have weighed at least 100 kg. The phantom layers and associated tray made transportation between departments as well as scanners quite achievable and there are no issues with phantom leakage (which is a potential issue for large, liquid filled grid phantoms). The vitamin E capsules could be visualised on both CT and MRI and hence comparison of capsule locations between the two modalities makes the quantification of geometric distortions achievable.

7.3 Geometric distortions on a 3 T MRI-simulator

In Chapter 5, the distortions on a MRI scanner, dedicated to MRI-simulation for radiotherapy were examined. Images were acquired with the 2D and 3D vendor-supplied correction algorithms to compare the differences in distortion distribution between the two. Differences in geometric distortions between image acquisitions with a conventional static table and a continuously moving table (TimCT) acquisitions were also measured.

Research questions:

What is the geometric performance of the MRI scanner with conventional acquisition sequences?

On the Siemens 3T Skyra, the maximum distortion observed with a conventional acquisition spin echo sequence over a FOV of 500 mm x 500 mm x 368 mm was 9.81 mm with a vendor supplied 2D correction algorithm applied during image acquisition. This was reduced to 4.37 mm when the 3D correction algorithm was applied. The mean distortion across the whole volume was halved when comparing the 3D corrected results to the 2D corrected results. This reduction in the magnitude of distortions observed is expected since the 3D correction algorithm corrects for gradient non-linearities in the slice selection direction as well as the phase and frequency direc-

tions. The 2D correction only corrects in the phase and frequency encoding directions. Hence, 3D correction algorithms should be utilised (when available on the scanner). This can be achieved during acquisition as well as retrospectively. With the 3D correction applied, distortions greater than 2 mm were not observed within a radial distance of 150 mm from the isocentre of the scanner.

How do the distortion patterns obtained with a continuously moving couch compare to static couch acquisitions?

The maximum distortions observed were reduced for the TimCT images when compared to the conventional acquisition sequences. For a spoiled gradient echo sequence with standard image acquisition (table speed = 0 mm/s), the maximum distortion observed was 6.07 mm and only encompassed 71% of the phantom volume. For the TimCT image acquisition with a table speed of 1.1 mm/s, the maximum distortion reduced to 4.42 mm over the entire phantom volume, with the largest distortions observed at the axial edges of the phantom. Whilst increasing the table speed by a factor of 2 reduced the acquisition time, the magnitude of the distortions observed increased and blurring was introduced as a result of the table movement, particularly at the peripheral regions of the axial FOV. TimCT would be a useful imaging technique for anatomical sites which require large imaging lengths with a smaller axial FOV (within a 200 mm radial distance from scanner isocentre). In cases where short image lengths are required, the conventional static acquisition sequences may provide the geometric accuracy required. The acquisition technique should be assessed on a case by case basis. The increased geometric accuracy and coverage obtained when imaging with TimCT needs to be traded-off for an increased scan time (by a factor of 3.5 for TimCT at 1.1 mm/s). Longer acquisition time could lead to increased patient movement, resulting in artefacts in the images, reducing the usefulness of the images for the purposes of RTP.

7.4 Impact of geometric distortion on whole breast radiotherapy

Chapter 6 investigated the implication of uncorrected geometric distortions on whole breast radiotherapy treatment planning with intensity modulated radiotherapy in a retrospective study over a patient cohort of 18. Phantom measurements quantified the residual systematic distortions (after application of vendor supplied correction algorithms) on a wide, closed-bore scanner (3 T Skyra) as well as a vertical open-bore scanner (1 T Panorama). The distortion maps obtained from these measurements were used to quantify the impact of systematic distortions alone. The phantom was not intended to be able to quantify patient induced distortions. A comparison between patient CT and MR images enabled the effects of combined systematic and patient induced distortions to be examined (Skyra only). The maximum distortion on the Skyra was measured at 7.88 mm (mean = 2.07 mm; 95% of volume experienced distortions below 4.67 mm) over a 500 x 500 x 254 mm^3 FOV. Maximum distortion on the Panorama was measured at 11.87 mm (mean = 1.71 mm; 95% of volume experienced distortions below 4.56 mm) over a 475 x 380 x 420 mm^3 FOV.

Research questions:

How do systematic distortions on different MRI systems impact the dose distribution for whole breast RTP?

Differences in geometric distortion were observed between the two scanners investigated. The residual systematic distortions observed on each scanner (after application of the vendor supplied correction algorithms on each system) were found to have negligible impact on dose distribution for tangential whole breast IMRT plans. All plans generated on distorted CT data matching the systematic geometric distortions from each MRI scanner met the DVH and visual acceptance criteria when recomputed on the original CT image for both scanners. The mean difference in PTV $V_{47.5\,Gy}$ was 0.17 $\pm$ 1.18% and 0.32 $\pm$ 2.51% for the Skyra and Panorama scanners respectively. Combined effects of the residual systematic and patient induced distortions were found to have a more significant impact on dose with eight of the 18 patients investigated having plans generated on the distorted image dataset fail the acceptable criteria when recomputed on the correct CT geometry. Two datasets failed the DVH criteria, four

patients were observed to fail the clinical visual plan criteria, and for two patients plans failed both the DVH and visual assessments.

How do patient specific distortions impact whole breast radiotherapy?

By isolating and quantifying system distortions with a good phantom design, it was possible to compare the relative magnitudes of systematic and patient related geometric distortions. The patient induced effects are larger than those introduced by the system, particularly at higher field strengths. On the 3T skyra, the mean maximum distortion observed over the CTV volumes from residual system distortions alone was 2.80 ± 0.97 mm. This increased to 6.25 ± 5.68 mm for the CTV volumes combining residual systematic distortions, patient induced inaccuracies and set-up uncertainties. This is due to the fact that the susceptibility variations are high in the breast with the variations in tissue types (lung, muscles, bone and glandular tissue).

7.5 Future work

At the conclusion of the work covered in this thesis, there are a number of studies which warrant further investigation. These include determining the impact of systematic and patient related distortions for other anatomical sites, quantifying MRI distortions on scanners to be used for radiotherapy across Australia, better accounting for patient induced distortions and to investigate the implications of geometric distortions for MRI-linac systems.

7.5.1 Determining the impact of distortions for other anatomical sites

Investigations into the impact of systematic and patient induced distortions for other clinical sites would be useful for the radiotherapy community. The methodology utilised in Chapter 6 could be adapted for head and neck, cervix and lung. This would give further indication into where the impact of these distortions is likely to be most pronounced. The impact of distortion will depend on whether they can be addressed on a relative or absolute scale. For breast the absolute distortions may be large compared to the centre of the scanner, however in radiotherapy treatment planning, the

treatment volume is set-up to the centre of the breast. Therefore the distortion measurements are relative to the distortion experienced at the centre of the breast. For other sites (e.g. lung), the treatment may be set up to a more central region in the scanner and the absolute distortions would require consideration to determine how the dose distribution is affected by a potentially distorted beam, compared to the geometry at the centre of the image.

7.5.2 Survey of MRI distortions for RTP in radiation oncology departments across Australia

With the use of MRI increasing in radiation oncology, quantification of the geometric distortions is crucial. As departments across Australia start utilising this modality further, adequate methods for quantifying these distortions should be in place. The 3D phantom developed for this study could potentially be utilised to survey the MRI scanners which may potentially be utilised in some capacity for imaging patients for radiotherapy. This information would be beneficial to all departments in determining the potential impact that the geometric distortions specific to their scanner may have on their RTP procedures. Additionally, a correction method could be developed from this work and applied where required to reduce larger geometric distortions.

7.5.3 Implications of geometric distortions on MRI-linac systems

Hybrid systems (such as the Australian MRI-linac) are designed to combine a linear accelerator and magnetic field. Based on the physics of how each of these systems work, both require modification in order to be able to function together in the same room. Consequently, both the uniformity and linearity are significantly worse and hence require careful assessment since this poses potential issues for planning and image guidance throughout treatment. Methods for quantifying and correcting distortions will need to be in place in order for these systems to achieve the required geometric performance.

7.5.4 Accounting for patient-related distortions

Patient related distortions will play a significant part in accounting for MRI distortions in the future. While correcting for these techniques was not discussed in this work, correcting for these by B_0 mapping [122] or reverse gradient image acquisition [101] should be investigated further. Integrating these into the radiotherapy workflow would minimise the impact of patient related geometric distortions for radiotherapy treatment planning. Ideally, a radiotherapy workflow should include methods for quantifying both systematic and patient related distortions. Systematic quantification would be less frequent, tested over time to ensure the consistency of the geometric performance of the system. Quantification of patient distortions would require individual assessment for situations where a high imaging bandwidth was undesirable or unable to resolve the distortion problems.

7.6 Summary

This work has developed an MRI distortion phantom adequate for quantifying systematic distortions on clinical radiotherapy scanners with a number image acquisition techniques, as well as determining the impact of patient and systematic distortions on tangential whole breast IMRT plans. Vendor supplied correction algorithms should always be utilised where possible in order to reduce the magnitude of systematic distortions to a more manageable level. Even with these corrections, geometric inaccuracies will still be present, with the largest distortions being found at the edges of the imaging FOV. Combined patient and systematic effects can impact the dosimetry of whole breast radiotherapy plans.

These advances in reducing geometric distortions, combined with widespread solutions to generating electron density maps, will potentially lead to accurate MR-only planning. While considered unlikely a few years ago, examples in the literature [26, 132] suggest that we are on the threshold of MR-only planning for various treatment sites. A truly exciting paradigm for radiotherapy treatment planning moving into the future.

References

[1] P. Dirix, K. Haustermans, and V. Vandecaveye, "The value of magnetic resonance imaging for radiotherapy planning," in *Seminars in Radiation Oncology*, vol. 24, pp. 151–159, Elsevier.

[2] V. S. Khoo, D. P. Dearnaley, D. J. Finnigan, A. Padhani, S. F. Tanner, and M. O. Leach, "Magnetic resonance imaging (MRI): considerations and applications in radiotherapy treatment planning," *Radiotherapy and Oncology*, vol. 42, no. 1, pp. 1–15, 1997.

[3] G. P. Liney and M. A. Moerland, "Magnetic resonance imaging acquisition techniques for radiotherapy planning," *Seminars in Radiation Oncology*, vol. 24, no. 3, pp. 160–168, 2014.

[4] M. B. Barton, S. Jacob, J. Shafiq, K. Wong, S. R. Thompson, T. P. Hanna, and G. P. Delaney, "Estimating the demand for radiotherapy from the evidence: A review of changes from 2003 to 2012," *Radiotherapy and Oncology*, vol. 112, no. 1, pp. 140–144, 2014.

[5] G. N. Hounsfield, "Computerized transverse axial scanning (tomography): Part 1. description of system," *The British Journal of Radiology*, vol. 46, no. 552, pp. 1016–1022, 1973.

[6] G. S. Payne, E. Charles-Edwards, and C. P. South, "Applications of computed tomography, magnetic resonance imaging and magnetic resonance spectroscopy for planning external beam radiotherapy," *Current Medical Imaging Reviews*, vol. 4, no. 4, pp. 236–249, 2008.

[7] R. A. Geise and E. C. McCullough, "The use of CT scanners in megavoltage photon-beam therapy planning," *Radiology*, vol. 124, no. 1, pp. 133–141, 1977.

[8] T. R. Mackie, J. W. Scrimger, and J. J. Battista, "A convolution method of calculating dose for 15âĂŘMV x rays," *Medical Physics*, vol. 12, no. 2, pp. 188–196, 1985.

[9] S. Hissoiny, B. Ozell, H. Bouchard, and P. Després, "GPUMCD: A new GPU-oriented monte carlo dose calculation platform," *Medical Physics*, vol. 38, no. 2, pp. 754–764, 2011.

[10] R. L. Siddon, "Fast calculation of the exact radiological path for a threeâĂŘdimensional CT array," *Medical Physics*, vol. 12, no. 2, pp. 252–255, 1985.

[11] L. L. Subak, H. Hricak, C. B. Powell, L. Azizi, and J. L. Stern, "Cervical carcinoma: computed tomography and magnetic resonance imaging for preoperative staging," *Obstetrics & Gynecology*, vol. 86, no. 1, pp. 43–50, 1995.

[12] N. Chung, L. Ting, W. Hsu, L. T. Lui, and P. Wang, "Impact of magnetic resonance imaging versus ct on nasopharyngeal carcinoma: primary tumor target delineation for radiotherapy," *Head & neck*, vol. 26, no. 3, pp. 241–246, 2004.

[13] "Diagnostic accuracy of preoperative magnetic resonance imaging in predicting curative resection of rectal cancer: prospective observational study," vol. 333, p. 779, 2006.

[14] C. Rasch, I. Barillot, P. Remeijer, A. Touw, M. van Herk, and J. V. Lebesque, "Definition of the prostate in CT and MRI: a multi-observer study," *International Journal of Radiation Oncology*Biology*Physics*, vol. 43, no. 1, pp. 57–66, 1999.

[15] C. Weltens, J. Menten, M. Feron, E. Bellon, P. Demaerel, F. Maes, W. Van den Bogaert, and E. van der Schueren, "Interobserver variations in gross tumor volume delineation of brain tumors on computed tomography and impact of magnetic resonance imaging," *Radiotherapy and Oncology*, vol. 60, no. 1, pp. 49–59, 2001.

[16] J. C. A. Dimopoulos, G. Schard, D. Berger, S. Lang, G. Goldner, T. Helbich, and R. Pötter, "Systematic evaluation of MRI findings in different stages of treatment of cervical cancer: Potential of MRI on delineation of target, pathoanatomic structures, and organs at risk," *International Journal of Radiation Oncology*Biology*Physics*, vol. 64, no. 5, pp. 1380–1388, 2006.

[17] M. Debois, R. Oyen, F. Maes, G. Verswijvel, G. Gatti, H. Bosmans, M. Feron, E. Bellon, G. Kutcher, H. Van Poppel, and L. Vanuytsel, "The contribution of magnetic resonance imaging to the three-dimensional treatment planning of localized prostate cancer," *International Journal of Radiation Oncology*Biology*Physics*, vol. 45, no. 4, pp. 857–865, 1999.

[18] H. Aoyama, H. Shirato, T. Nishioka, S. Hashimoto, K. Tsuchiya, K. Kagei, R. Onimaru, Y. Watanabe, and K. Miyasaka, "Magnetic resonance imaging system for three-dimensional conformal radiotherapy and its impact on gross tumor volume delineation of central nervous system tumors," *International Journal of Radiation Oncology*Biology*Physics*, vol. 50, no. 3, pp. 821–827, 2001.

[19] B. Emami, A. Sethi, and G. J. Petruzzelli, "Influence of MRI on target volume delineation and IMRT planning in nasopharyngeal carcinoma," *International Journal of Radiation Oncology*Biology*Physics*, vol. 57, no. 2, pp. 481–488, 2003.

[20] V. S. Khoo and D. L. Joon, "New developments in MRI for target volume delineation in radiotherapy," *British Journal of Radiology*, vol. 79, no. Special Issue 1, pp. S2–S15, 2006.

[21] D. A. Jaffray, M. C. Carlone, M. F. Milosevic, S. L. Breen, T. Stanescu, A. Rink, H. Alasti, A. Simeonov, M. C. Sweitzer, and J. D. Winter, "A facility for magnetic resonance-guided radiation therapy," vol. 24, pp. 193–195, 2014.

[22] S. Mutic and J. F. Dempsey, "The viewray system: Magnetic resonanceâĂŞguided and controlled radiotherapy," 2014.

[23] B. G. Fallone, "The rotating biplanar linac-magnetic resonance imaging system," vol. 24, pp. 200–202, 2014.

[24] P. J. Keall, M. Barton, and S. Crozier, "The australian magnetic resonance imagingâĂŞlinac program," in *Seminars in radiation oncology*, vol. 24, pp. 203–206, Elsevier.

[25] J. J. Lagendijk, B. W. Raaymakers, and M. van Vulpen, "The magnetic resonance imaging-linac system," vol. 24, pp. 207–209, 2014.

[26] J. J. W. Lagendijk, B. W. Raaymakers, C. A. T. V. d. Berg, M. A. Moerland, M. E. Philippens, and M. v. Vulpen, "MR guidance in radiotherapy," *Physics in Medicine and Biology*, vol. 59, no. 21, p. R349, 2014.

[27] D. A. Jaffray, "Image-guided radiotherapy: from current concept to future perspectives," *Nature Reviews. Clinical Oncology*, vol. 9, no. 12, pp. 688–99, 2012.

[28] N. A. Mayr, V. A. Magnotta, J. C. Ehrhardt, J. A. Wheeler, J. I. Sorosky, B. C. Wen, C. S. Davis, R. E. Pelsang, B. Anderson, J. F. Doornbos, D. H. Hussey, and W. T. C. Yuh, "Usefulness of tumor volumetry by magnetic resonance imaging in assessing response to radiation therapy in carcinoma of the uterine cervix," *International Journal of Radiation Oncology*Biology*Physics*, vol. 35, no. 5, pp. 915–924, 1996.

[29] M. Lambrecht, V. Vandecaveye, F. De Keyzer, S. Roels, F. Penninckx, E. Van Cutsem, F. Claus, and K. Haustermans, "Value of diffusion-weighted magnetic resonance imaging for prediction and early assessment of response to neoadjuvant radiochemotherapy in rectal cancer: Preliminary results," *International Journal of Radiation Oncology*Biology*Physics*, vol. 82, no. 2, pp. 863–870, 2012.

[30] B. Barbaro, R. Vitale, V. Valentini, S. Illuminati, F. M. Vecchio, G. Rizzo, M. A. Gambacorta, C. Coco, A. Crucitti, R. Persiani, L. Sofo, and L. Bonomo, "Diffusion-weighted magnetic resonance imaging in monitoring rectal cancer response to neoadjuvant chemoradiotherapy," *International Journal of Radiation Oncology*Biology*Physics*, vol. 83, no. 2, pp. 594–599, 2012.

[31] C. Tsien, Y. Cao, and T. Chenevert, "Clinical applications for diffusion magnetic resonance imaging in radiotherapy," *Seminars in Radiation Oncology*, vol. 24, no. 3, pp. 218–226, 2014.

[32] R. Prabhakar, P. K. Julka, T. Ganesh, A. Munshi, R. C. Joshi, and G. K. Rath, "Feasibility of using MRI alone for 3D radiation treatment planning in brain tumors," *Japanese Journal of Clinical Oncology*, vol. 37, no. 6, pp. 405–411, 2007.

[33] J. T. Bushberg, A. J. Seibert, E. M. J. Leidholdt, and J. M. Boone, *The Essential Physics of Medical Imaging*. Philadelphia: Lippincott Williams & Wilkins, second ed., 2002.

[34] P. C. Lauterbur, "Image formation by induced local interactions: Examples employing nuclear magnetic resonance," *Nature*, vol. 242, no. 5394, pp. 190–191, 1973.

[35] A. Fransson, P. Andreo, and R. Pötter, "Aspects of mr image distortions in radiotherapy treatment planning," *Strahlentherapie und Onkologie*, vol. 177, no. 2, pp. 59–73, 2001.

[36] P. Jezzard and S. Clare, "Sources of distortion in functional MRI data," *Human Brain Mapping*, vol. 8, no. 2-3, pp. 80–85, 1999.

[37] P. Jezzard, *The physical basis of spatial distortions in magnetic resonance images*, book section 29, pp. 499–514. Elsevier, second ed., 2009.

[38] D. Wang, W. Strugnell, G. Cowin, D. M. Doddrell, and R. Slaughter, "Geometric distortion in clinical MRI systems: Part I: evaluation using a 3D phantom," *Magnetic Resonance Imaging*, vol. 22, no. 9, pp. 1211–1221, 2004.

[39] D. Mah, M. Steckner, E. Palacio, R. Mitra, T. Richardson, and G. E. Hanks, "Characteristics and quality assurance of a dedicated open 0.23 T mri for radiation therapy simulation," *Medical Physics*, vol. 29, no. 11, pp. 2541–2547, 2002.

[40] L. N. Baldwin, K. Wachowicz, S. D. Thomas, R. Rivest, and B. G. Fallone, "Characterization, prediction, and correction of geometric distortion in 3 T MR images," *Medical Physics*, vol. 34, no. 2, pp. 388–399, 2007.

[41] Siemens Healthcare, "Trueform magnet and gradient design," Germany, 2011.

[42] J. F. Schenck, "The role of magnetic susceptibility in magnetic resonance imaging: MRI magnetic compatibility of the first and second kinds," *Medical Physics*, vol. 23, no. 6, pp. 815–850, 1996.

[43] AAPM, "Acceptance testing and quality assurance procedures for magnetic resonance imaging facilities," Report 100, American Association of Physicists in Medicine, December 2010.

[44] J. L. Gunter, M. A. Bernstein, B. J. Borowski, C. P. Ward, P. J. Britson, J. P. Felmlee, N. Schuff, M. Weiner, and C. R. Jack, "Measurement of MRI scanner performance with the ADNI phantom," *Medical Physics*, vol. 36, no. 6, pp. 2193–2205, 2009.

[45] B. Zhang, D. MacFadden, A. Z. Damyanovich, M. Rieker, J. Stainsby, M. Bernstein, D. A. Jaffray, D. Mikulis, and C. Menard, "Development of a geometrically accurate imaging protocol at 3 Tesla MRI for stereotactic radiosurgery treatment planning," *Physics in Medicine and Biology*, vol. 55, no. 1, pp. 6601–6615, 2010.

[46] C. J. G. Bakker, M. A. Moerland, R. Bhawandien, and R. Beersma, "Analysis of machine-dependent and object-induced geometric distortion in 2DFT MR imaging," *Magnetic Resonance Imaging*, vol. 10, no. 4, pp. 597–608, 1992.

[47] C. P. Karger, A. Höss, R. Bendl, V. Canda, and L. Schad, "Accuracy of device-specific 2D and 3D image distortion correction algorithms for magnetic resonance imaging of the head provided by a manufacturer," *Physics in Medicine and Biology*, vol. 51, no. 12, p. N253, 2006.

[48] S. F. Tanner, D. J. Finnigan, V. S. Khoo, P. Mayles, D. P. Dearnaley, and M. O. Leach, "Radiotherapy planning of the pelvis using distortion corrected MR images: the removal of system distortions," *Physics in Medicine and Biology*, vol. 45, no. 8, pp. 2117–32, 2000.

[49] S. Crijns, B. Raaymakers, and J. Lagendijk, "Real-time correction of magnetic field inhomogeneity-induced image distortions for MRI-guided conventional and proton radiotherapy," *Physics in Medicine and Biology*, vol. 56, no. 1, pp. 289–297, 2011.

[50] D. Wang, D. M. Doddrell, and G. Cowin, "A novel phantom and method for comprehensive 3-dimensional measurement and correction of geometric distortion in magnetic resonance imaging," *Magnetic Resonance Imaging*, vol. 22, no. 4, pp. 529–542, 2004.

[51] L. N. Baldwin, K. Wachowicz, and B. G. Fallone, "A two-step scheme for distortion rectification of magnetic resonance images," *Medical Physics*, vol. 36, no. 9, pp. 3917–3926, 2009.

[52] T. Mizowaki, Y. Nagata, K. Okajima, M. Kokubo, Y. Negoro, N. Araki, and M. Hiraoka, "Reproducibility of geometric distortion in magnetic resonance imaging based on phantom studies," *Radiotherapy and Oncology*, vol. 57, no. 2, pp. 237–242, 2000.

[53] R. Viard, S. Mordon, N. Betrouni, M. Vermandel, M. Vanhoutte, and J. Rousseau, "Correction of images in an open-configuration MR imaging system for radiation therapy planning and interventional MRI," *International Journal of Computer Assisted Radiology and Surgery*, vol. 3, no. 3-4, pp. 283–289, 2008.

[54] G. J. Kutcher, L. Coia, M. Gillin, W. F. Hanson, S. Leibel, R. J. Morton, J. R. Palta, J. A. Purdy, L. E. Reinstein, G. K. Svensson, and et al., "Comprehensive QA for radiation oncology: report of AAPM Radiation Therapy Committee Task Group 40," *Medical Physics*, vol. 21, no. 4, pp. 581–618, 1994.

[55] A. Janke, H. Zhao, G. J. Cowin, G. J. Galloway, and D. M. Doddrell, "Use of spherical harmonic deconvolution methods to compensate for nonlinear gradient effects on MRI images," *Magnetic Resonance in Medicine*, vol. 52, no. 1, pp. 115–122, 2004.

[56] M. M. Breeuwer, M. Holden, and W. Zylka, "Detection and correction of geometric distortion in 3D MR images," vol. 4322, pp. 1110–1120.

[57] J. Jovicich, S. Czanner, D. Greve, E. Haley, A. van der Kouwe, R. Gollub, D. Kennedy, F. Schmitt, G. Brown, J. MacFall, B. Fischl, and A. Dale, "Reliability in multi-site structural MRI studies: Effects of gradient non-linearity correction on phantom and human data," *NeuroImage*, vol. 30, no. 2, 2006.

[58] S. J. Doran, L. Charles-Edwards, S. A. Reinsberg, and M. O. Leach, "A complete distortion correction for MR images: I. gradient warp correction," *Physics in Medicine and Biology*, vol. 50, no. 7, p. 1343, 2005.

[59] D. Wang, W. Strugnell, G. Cowin, D. M. Doddrell, and R. Slaughter, "Geometric distortion in clinical MRI systems: Part II: correction using a 3D phantom," *Magnetic Resonance Imaging*, vol. 22, no. 9, pp. 1223–1232, 2004.

[60] T. Stanescu, H. S. Jans, K. Wachowicz, and B. G. Fallone, "Investigation of a 3D system distortion correction method for MR images," *Journal of Applied Clinical Medical Physics*, vol. 11, no. 1, p. 2961, 2010.

[61] N. Maikusa, F. Yamashita, K. Tanaka, O. Abe, A. Kawaguchi, H. Kabasawa, S. Chiba, A. Kasahara, N. Kobayashi, T. Yuasa, N. Sato, H. Matsuda, and T. Iwatsubo, "Improved volumetric measurement of brain structure with a distortion correction procedure using an ADNI phantom," *Medical Physics*, vol. 40, no. 6, pp. 062303:1–10, 2013.

[62] T. Tadic, D. A. Jaffray, and T. Stanescu, "Harmonic analysis for the characterization and correction of geometric distortion in MRI," *Medical Physics*, vol. 41, no. 11, p. 112303, 2014.

[63] H. Wang, J. Balter, and Y. Cao, "Patient-induced susceptibility effect on geometric distortion of clinical brain MRI for radiation treatment planning on a 3T scanner," *Physics in Medicine and Biology*, vol. 58, no. 3, p. 465, 2013.

[64] S. P. M. Crijns, C. J. G. Bakker, P. R. Seevinck, H. d. Leeuw, J. J. W. Lagendijk, and B. W. Raaymakers, "Towards inherently distortion-free MR images for image-guided radiotherapy on an MRI accelerator," *Physics in Medicine and Biology*, vol. 57, no. 5, p. 1349, 2012.

[65] M. A. Moerland, R. Beersma, R. Bhagwandien, H. K. Wijrdeman, and C. J. G. Bakker, "Analysis and correction of geometric distortions in 1.5 T magnetic resonance images for use in radiotherapy treatment planning," *Physics in Medicine and Biology*, vol. 40, no. 10, p. 1651, 1995.

[66] Y. Okamoto, K. Imanaka, T. Sakaguchi, T. Kushima, and M. Kono, "Fundamental study on development of MRI simulation system for radiotherapy planning," *International Journal of Radiation Oncology*Biology*Physics*, vol. 27, Supplement 1, p. 303, 1993.

[67] R. C. Krempien, K. Schubert, D. Zierhut, M. C. Steckner, M. Treiber, W. Harms, U. Mende, D. Latz, M. Wannenmacher, and F. Wenz, "Open low-field magnetic resonance imaging in radiation therapy treatment planning," *International Journal of Radiation Oncology*Biology*Physics*, vol. 53, no. 5, pp. 1350–1360, 2002.

[68] G. P. Liney, S. C. Owen, A. K. E. Beaumont, V. R. Lazar, D. J. Manton, and A. W. Beavis, "Commissioning of a new wide-bore MRI scanner for radiotherapy planning of head and neck cancer," *The British Journal of Radiology*, vol. 86, no. 1027, pp. 1–9, 2013.

[69] G. Liney, R. Rai, L. Holloway, and S. Vinod, "A dedicated MRI scanner for radiotherapy planning: Early experiences," *MAGNETOM Flash*, 2014.

[70] C. K. Glide-Hurst, N. Wen, D. Hearshen, J. Kim, M. Pantelic, B. Zhao, T. Mancell, K. Levin, B. Movsas, I. J. Chetty, and M. S. Siddiqui, "Initial clinical experience with a radiation oncology dedicated open 1.0T MR-simulation," *Journal of Applied Clinical Medical Physics*, vol. 16, no. 2.

[71] S. Devic, "MRI simulation for radiotherapy treatment planning," *Medical Physics*, vol. 39, no. 11, pp. 6701–11, 2012.

[72] L. Chen, R. A. Price Jr, T. B. Nguyen, L. Wang, J. S. Li, L. Qin, M. Ding, E. Palacio, C. M. Ma, and A. Pollack, "Dosimetric evaluation of MRI-based treatment planning for prostate cancer," *Physics in Medicine and Biology*, vol. 49, no. 22, pp. 5157–5170, 2004.

[73] B. Petersch, J. Bogner, A. Fransson, T. Lorang, and R. Pötter, "Effects of geometric distortion in 0.2 T MRI on radiotherapy treatment planning of prostate cancer," *Radiotherapy and Oncology*, vol. 71, no. 1, pp. 55–64, 2004.

[74] J. Balter, Y. Cao, H. Wang, K. Huang, S.-H. Hsu, M. Requardt, and S. M. Shea, "Optimizing MRI for radiation oncology: Initial investigations," *MAGNETOM Flash*, pp. 45–49, 2013.

[75] M. Karlsson, M. G. Karlsson, T. Nyholm, C. Amies, and B. Zackrisson, "Dedicated magnetic resonance imaging in the radiotherapy clinic," *International Journal of Radiation Oncology*Biology*Physics*, vol. 74, no. 2, pp. 644–651, 2009.

[76] T. Stanescu, J. Hans-Sonke, P. Stavrev, and G. B. Fallone, "3T MR-based treatment planning for radiotherapy of brain lesions," *Radiology and Oncology*, vol. 40, no. 2, pp. 125–132, 2006.

[77] J. Sun, J. Dowling, P. Pichler, F. Menk, D. Rivest-Henault, J. Lambert, J. Parker, J. Arm, L. Best, J. Martin, J. W. Denham, and P. B. Greer, "MRI simulation: End-to-end testing for prostate radiation therapy using geometric pelvic MRI phantoms," *Physics in Medicine and Biology*, vol. 60, no. 8, p. 3097, 2015.

[78] K. K. Brock and L. A. Dawson, "Point: Principles of magnetic resonance imaging integration in a computed tomography-based radiotherapy workflow," vol. 24, pp. 169–174, 2014.

[79] M. L. Kessler, "Image registration and data fusion in radiation therapy," *British Journal of Radiology*, vol. 79, no. special issue 1, pp. S99–S108, 2006.

[80] C. J. Dean, J. R. Sykes, R. A. Cooper, P. Hatfield, B. Carey, S. Swift, S. E. Bacon, D. Thwaites, D. Sebag-Montefiore, and A. M. Morgan, "An evaluation of four ct-mri co-registration techniques for radiotherapy treatment planning of prone rectal cancer patients," *The British Journal of Radiology*, vol. 85, no. 1009, pp. 61–68, 2012.

[81] J. N. H. Brunt, "Computed tomography-magnetic resonance image registration in radiotherapy treatment planning," *Clinical Oncology*, vol. 22, no. 8, pp. 688–697, 2010.

[82] S. Ghose, L. Holloway, K. Lim, P. Chan, J. Veera, S. K. Vinod, G. Liney, P. B. Greer, and J. Dowling, "A review of segmentation and deformable registration methods applied to adaptive cervical cancer radiation therapy treatment planning," *Artificial Intelligence in Medicine*, vol. 64, no. 2, pp. 75–87, 2015.

[83] E. S. Paulson, B. Erickson, C. Schultz, and X. Allen Li, "Comprehensive MRI simulation methodology using a dedicated MRI scanner in radiation oncology for external beam radiation treatment planning," *Medical Physics*, vol. 42, no. 1, pp. 28–39, 2015.

[84] A. L. Chin, A. Lin, S. Anamalayil, and B.-K. K. Teo, "Feasibility and limitations of bulk density assignment in mri for head and neck imrt treatment planning."

[85] S. J. Hoogcarspel, J. M. V. d. Velden, J. J. W. Lagendijk, M. v. Vulpen, and B. W. Raaymakers, "The feasibility of utilizing pseudo CT-data for online MRI based treatment plan adaptation for a stereotactic radiotherapy treatment of spinal bone metastases," *Physics in Medicine and Biology*, vol. 59, no. 23, p. 7383, 2014.

[86] J. Lambert, P. B. Greer, F. Menk, J. Patterson, J. Parker, K. Dahl, S. Gupta, A. Capp, C. Wratten, and C. Tang, "MRI-guided prostate radiation therapy planning: Investigation of dosimetric accuracy of MRI-based dose planning," *Radiotherapy and Oncology*, vol. 98, no. 3, pp. 330–334, 2011.

[87] J. Jonsson, M. Karlsson, M. Karlsson, and T. Nyholm, "Treatment planning using MRI data: an analysis of the dose calculation accuracy for different treatment regions," *Radiation Oncology*, vol. 5, no. 1, p. 62, 2010.

[88] Y. K. Lee, M. Bollet, G. Charles-Edwards, M. A. Flower, M. O. Leach, H. McNair, E. Moore, C. Rowbottom, and S. Webb, "Radiotherapy treatment planning of prostate cancer using magnetic resonance imaging alone," *Radiotherapy and Oncology*, vol. 66, no. 2, pp. 203–216, 2003.

[89] J. A. Dowling, J. Lambert, J. Parker, O. Salvado, J. Fripp, A. Capp, C. Wratten, J. W. Denham, and P. B. Greer, "An atlas-based electron density mapping method for magnetic resonance imaging (MRI)-alone treatment planning and adaptive MRI-based prostate radiation therapy," *International Journal of Radiation Oncology*Biology*Physics*, vol. 83, no. 1, pp. e5–e11, 2012.

[90] S.-H. Hsu, Y. Cao, K. Huang, M. Feng, and J. M. Balter, "Investigation of a method for generating synthetic CT models from MRI scans of the head and neck for radiation therapy," *Physics in Medicine and Biology*, vol. 58, no. 23, p. 8419, 2013.

[91] M. S. R. Gudur, W. Hara, Q.-T. Le, L. Wang, L. Xing, and R. Li, "A unifying probabilistic bayesian approach to derive electron density from MRI for radiation therapy treatment planning," *Physics in Medicine and Biology*, vol. 59, no. 21, p. 6595, 2014.

[92] T. Nyholm, M. Nyberg, M. G. Karlsson, and M. Karlsson, "Systematisation of spatial uncertainties for comparison between a MR and a CT-based radiotherapy workflow for prostate treatments," *Radiation Oncology*, vol. 4, p. 54, 2009.

[93] T. Stanescu, H.-S. Jans, N. Pervez, P. Stavrev, and B. G. Fallone, "A study on the magnetic resonance imaging (MRI)-based radiation treatment planning of intrecranial lesions," *Physics in Medicine and Biology*, vol. 53, no. 13, pp. 3579–3593, 2008.

[94] J. J. W. Lagendijk, B. W. Raaymakers, A. J. E. Raaijmakers, J. Overweg, K. J. Brown, E. M. Kerkhof, R. W. van der Put, B. HÃěrdemark, M. van Vulpen, and U. A. van der Heide, "MRI/linac integration," *Radiotherapy and Oncology*, vol. 86, no. 1, pp. 25–29, 2008.

[95] B. G. Fallone, B. Murray, S. Rathee, T. Stanescu, S. Steciw, S. Vidakovic, E. Blosser, and D. Tymofichuk, "First MR images obtained during megavoltage photon irradiation from a prototype integrated linac-MR system," *Medical Physics*, vol. 36, no. 6, pp. 2084–2088, 2009.

[96] P. Metcalfe, G. P. Liney, L. Holloway, A. Walker, M. Barton, G. P. Delaney, S. Vinod, and W. Tomé, "The potential for an enhanced role for MRI in radiation-therapy treatment planning," *Technology in Cancer Research & Treatment*, vol. 12, no. 5, pp. 429–446, 2013.

[97] A. Beavis, P. Gibbs, R. Dealey, and V. Whitton, "Radiotherapy treatment planning of brain tumours using MRI alone," *The British Journal of Radiology*, vol. 71, no. 845, pp. 544–548, 1998.

[98] L. Chen, J. R. A. Price, L. Wang, J. Li, L. Qin, S. McNeeley, C. M. C. Ma, G. M. Freedman, and A. Pollack, "MRI-based treatment planning for radiotherapy: Dosimetric verification for prostate IMRT," *International Journal of Radiation Oncology*Biology*Physics*, vol. 60, no. 2, pp. 636–647, 2004.

[99] D. Pasquier, N. Betrouni, M. Vermandel, T. Lacornerie, E. Lartigau, and J. Rousseau, "MRI alone simulation for conformal radiation therapy of prostate cancer: technical aspects," in *Engineering in Medicine and Biology Society, 28th Annual International Conference of the IEEE*, pp. 160–163, IEEE.

[100] F.-J. Prott, U. Haverkamp, H. Eich, A. Resch, O. Micke, A.-R. Fischedick, N. Willich, and R. Pötter, "Effect of distortions and asymmetry in MR images on radiotherapeutic treatment planning," *International Journal of Cancer*, vol. 90, no. 1, pp. 46–50, 2000.

[101] H. Chang and J. M. Fitzpatrick, "A technique for accurate magnetic resonance imaging in the presence of field inhomogeneities," *IEEE Transactions on Medical Imaging*, vol. 11, no. 3, pp. 319–329, 1992.

[102] J. A. Antolak and I. I. Rosen, "Planning target volumes for radiotherapy: how much margin is needed?," *International Journal of Radiation Oncology*Biology*Physics*, vol. 44, no. 5, pp. 1165–70, 1999.

[103] A. Landi, R. Marina, C. DeGrandi, A. Crespi, G. Montanari, E. P. Sganzerla, and S. M. Gaini, "Accuracy of stereotactic localisation with magnetic resonance compared to CT scan: Experimental findings," *Acta Neurochirurgica*, vol. 143, no. 6, pp. 593–601, 2001.

[104] F. J. Prott, U. Haverkamp, N. Willich, A. Resch, U. Stöber, and R. Pötter, "Comparison of imaging accuracy at different MRI units based on phantom measurements," *Radiotherapy and Oncology*, vol. 37, no. 3, pp. 221–224, 1995.

[105] H.-H. Chen, R. D. Boykin, G. D. Clarke, J.-H. T. Gao, and J. W. R. III, "Routine testing of magnetic field homogeneity on clinical MRI systems," *Medical Physics*, vol. 33, no. 11, pp. 4299–4306, 2006.

[106] AAPM, "Quality assurance methods and phantoms for magnetic resonance imaging: Report of AAPM nuclear magnetic resonance task group no. 1," *Medical Physics*, vol. 17, no. 2, pp. 287–295, 1990.

[107] M. A. Moerland, *Magnetic Resonance Imaging in Radiotherapy Treatment Planning*. Thesis, 1996.

[108] P. Dammann, O. Kraff, S. Maderwald, E. R. Gizewski, M. Ladd, T. Gasser, and U. Sure, "Evaluation of geometrical distortion in a head-sized phantom at ultra-high-field MRI (7 Tesla) for image guided applications in neurosurgery," March 25-27 2010 2010.

[109] R. C. Orth, P. Sinha, E. L. Madsen, G. Frank, F. R. Korosec, T. R. Mackie, and M. Mehta, "Development of a unique phantom to assess the geometric accuracy of magnetic resonance imaging for stereotactic localization," *Neurosurgery*, vol. 45, no. 6, 1999.

[110] Z. Caramanos, V. S. Fonov, S. J. Francis, S. Narayanan, G. B. Pike, D. L. Collins, and D. L. Arnold, "Gradient distortions in MRI: Characterizing and correcting for

their effects on SIENA-generated measures of brain volume change," *NeuroImage*, vol. 49, no. 2, pp. 1601–1611, 2010.

[111] V. S. Fonov, A. Janke, Z. Caramanos, D. L. Arnold, S. Narayanan, G. B. Pike, and D. L. Collins, "Improved precision in the measurement of longitudinal global and regional volumetric changes via a novel MRI gradient distortion characterization and correction technique," *Medical Imaging and Augmented Reality*, pp. 324–333, 2010.

[112] R. Bhagwandien, M. A. Moerland, C. J. G. Bakker, R. Beersma, and J. J. W. Lagendijk, "Numerical analysis of the magnetic field for arbitrary magnetic susceptibility distributions in 3D," *Magnetic Resonance Imaging*, vol. 12, no. 1, pp. 101–107, 1994.

[113] K. Engelhard, H. P. Hollenbach, K. Wohlfart, E. Imhoff, and F. A. Fellner, "Comparison of whole-body MRI with automatic moving table technique and bone scintigraphy for screening for bone metastases in patients with breast cancer," *European Radiology*, vol. 14, no. 1, pp. 99–105, 2004.

[114] E. Paulson, R. Prost, and X. Li, ""step and shoot MRI:" a simple acquisition method to reduce gradient nonlinearity-induced geometric distortions for radiation treatment planning," *Medical Physics*, vol. 38, no. 6, pp. 3770–3770, 2011.

[115] H. P. Fautz and S. A. R. Kannengiesser, "Sliding multislice (SMS): A new technique for minimum FOV usage in axial continuously moving-table acquisitions," *Magnetic Resonance in Medicine*, vol. 55, no. 2, pp. 363–370, 2006.

[116] D. G. Kruger, S. J. Riederer, R. C. Grimm, and P. J. Rossman, "Continuously moving table data acquisition method for long FOV contrast-enhanced MRA and whole-body MRI," *Magnetic Resonance in Medicine*, vol. 47, no. 2, pp. 224–231, 2002.

[117] P. Börnert and B. Aldefeld, "Principles of whole-body continuously-moving-table MRI," *Journal of Magnetic Resonance Imaging*, vol. 28, no. 1, pp. 1–12, 2008.

[118] J. Schaefer and H.-P. Schlemmer, "Total-body MR-imaging in oncology," *European Radiology*, vol. 16, no. 9, pp. 2000–2015, 2006.

[119] J. A. Polzin, D. G. Kruger, D. H. Gurr, J. H. Brittain, and S. J. Riederer, "Correction for gradient nonlinearity in continuously moving table mr imaging," *Magnetic Resonance in Medicine*, vol. 52, no. 1, pp. 181–187, 2004.

[120] D. Rivest-Hénault, N. Dowson, P. Greer, J. Fripp, and J. Dowling, "Robust inverse-consistent affine CT-MR registration in mri-assisted and MRI-alone prostate radiation therapy," *Medical Image Analysis*, vol. 23, no. 1, pp. 56–69, 2015.

[121] M. Modat, G. R. Ridgway, Z. A. Taylor, M. Lehmann, J. Barnes, D. J. Hawkes, N. C. Fox, and S. Ourselin, "Fast free-form deformation using graphics processing units," *Computer Methods Programs Biomedicine*, vol. 98, no. 3, pp. 278–84, 2010.

[122] P. Jezzard and R. S. Balaban, "Correction for geometric distortion in echo planar images from b_0 field variations," *Magnetic Resonance in Medicine*, vol. 34, no. 1, pp. 65–73, 1995.

[123] G. Delaney, M. Barton, and S. Jacob, "Estimation of an optimal radiotherapy utilization rate for breast carcinoma," *Cancer*, vol. 98, no. 9, pp. 1977–1986, 2003.

[124] L. Hong, M. Hunt, C. Chui, S. Spirou, K. Forster, H. Lee, J. Yahalom, G. J. Kutcher, and B. McCormick, "Intensity-modulated tangential beam irradiation of the intact breast," *International Journal of Radiation Oncology*Biology*Physics*, vol. 44, no. 5, pp. 1155–1164, 1999.

[125] C. S. Mayo, M. M. Urie, and T. J. Fitzgerald, "Hybrid IMRT plans-concurrently treating conventional and IMRT beams for improved breast irradiation and reduced planning time," *International Journal of Radiation Oncology*Biology*Physics*, vol. 61, no. 3, pp. 922–932, 2005.

[126] C. C. Popescu, I. A. Olivotto, W. A. Beckham, W. Ansbacher, S. Zavgorodni, R. Shaffer, E. S. Wai, and K. Otto, "Volumetric modulated arc therapy improves dosimetry and reduces treatment time compared to conventional intensity-modulated radiotherapy for locoregional radiotherapy of left-sided breast cancer and internal mammary nodes," *International Journal of Radiation Oncology*Biology*Physics*, vol. 76, no. 1, pp. 287–295, 2010.

[127] RTOG, "A phase III trial of accelerated whole breast irradiation with hypofractionation plus concurrent boost versus standard whole breast irradiation plus sequential boost for early-stage breast cancer," Report 1005, RTOG, 2012.

[128] K. Farahani, U. Sinha, S. Sinha, L. C. Chiu, and R. B. Lufkin, "Effect of field strength on susceptibility artifacts in magnetic resonance imaging," *Computerized Medical Imaging Graphics*, vol. 14, no. 6, pp. 409–13, 1990.

[129] A. van Mourik, S. van Kranen, S. den Hollander, J.-J. Sonke, M. van Herk, and C. van Vliet-Vroegindeweij, "Effects of setup errors and shape changes on breast radiotherapy," *International Journal of Radiation Oncology*Biology*Physics*, vol. 79, no. 5, pp. 1557–1564, 2011.

[130] E. C. Harron, H. M. McCallum, E. L. Lambert, D. Lee, and G. D. Lambert, "Dosimetric effects of setup uncertainties on breast treatment delivery," *Medical Dosimetry*, vol. 33, no. 4, pp. 293–298, 2009.

[131] A. Michalski, J. Atyeo, J. Cox, and M. Rinks, "Inter- and intra-fraction motion during radiation therapy to the whole breast in the supine position: A systematic review," *Journal of Medical Imaging and Radiation Oncology*, vol. 56, no. 5, pp. 499–509, 2012.

[132] T. Nyholm and J. Jonsson, "Counterpoint: Opportunities and challenges of a magnetic resonance imaging-only radiotherapy work flow," *Seminars in Radiation Oncology*, vol. 24, no. 3, pp. 175–180, 2014.

UNIVERSITY OF WOLLONGONG

AGREEMENT FOR DEPOSIT OF HDR THESIS IN DIGITAL REPOSITORY
KEY DETAILS

1.	Student Name	**Amy Louise Walker**
2.	Student No	**3456882**
3.	Email address	**aw554@uowmail.edu.au**
4.	School	**School of Physics**
5.	Faculty	**Engineering and Information Sciences**
6.	Supervisor	**Peter Metcalfe**
7.	Title of thesis	**Physics on MR distortion: Impact on breast cancer radiotherapy**
8.	Keywords	MRI, geometric distortion, radiotherapy, phantom, breast IMRT
9.	*Field of Research (FoR) codes (optional) See explanation below	029903
10.	Restricted Access The University is committed to making HDR theses publicly available. If a restriction is required, please consult your supervisor prior to completing this section	Is a restriction required for this thesis, or part thereof? ☐ Yes ☒ No If Yes: a) Nominate restriction period: _____ months b) Provide details of the reason for the restriction: ☐ Publishing/patent ☐ Third party copyright ☐ Commercial /in confidence ☐ Other (please specify) _____
11.	Release of thesis automatically at the end of the expiry period (if applicable)	☒ Yes ☐ No (To ensure your thesis is deposited and accessible via the UOW digital repository at the expiry of the restriction period, tick Yes) If No, provide the reason why the thesis should not be released at the expiry of the restriction period. (Note: If you tick No, the Library will contact your supervisor at the end of the expiry period to request release of the thesis)
12.	Third party copyright material that has been used without consent (if applicable)	If the thesis contains material whose copyright belongs to a third party and has been used without consent: a) Would gaining consent to include the third party copyright material in the electronic copy of the thesis be onerous or expensive? ☐ Yes ☐ No b) Would removal of the copyright material compromise the thesis?

		☐ Yes ☐ No

***Field of Research (FoR)** code classifications are used in the measurement and analysis of research and experimental development (R&D) undertaken in Australia,according to the field of research. In this respect, it is the methodology used in the R&D that is being considered. UOW uses FoR codes to classify research outputs, and has been used to report research data to the Commonwealth Government.

The FoR has three hierarchical levels, namely Divisions (at the broadest subject or discipline level), Groups and Fields (at finer levels). Students submitting their HDR thesis have the option to classify their research using the Group level (4 digit code) or Field level (6 digit code). All Divisions, Groups and Fields are assigned unique codes.

TERMS & CONDITIONS

1. Definitions

1.1. In this Agreement:

"**Digital Repository**" means Research Online or any other open access electronic repository operated by UOW or its agents;

"**UOW**" means the University of Wollongong;

"**Work**" means the thesis you are depositing including any abstract, object, text, image and related data;

"**You**" means the Candidate identified in item 1 of the Key Details;

"Third party copyright" means any material where the copyright is owned by another person

2. Your warranties

2.1. You warrant that:

(a) all or part of the Work is your original work;

(b) the Work does not violate or infringe any copyright, trademark, patent other rights of any person;

(c) if you have used another person's copyright work or intellectual property rights:

(i) you have obtained permission from that person for the use of this material as contemplated by this agreement; or

(ii) you have confirmed in item 10 of the Key Details reasons you have not obtained permission to use or to grant to UOW the licence contemplated by this agreement;

(d) if the Work has been commissioned, sponsored or supported in any way, you have fulfilled all obligations required by such contract or agreement;

(e) the Work may be deposited in the Digital Repository without breaching the intellectual property rights of any third party provided UOW complies with any restrictions identified in items 8 and 9 of the Key Details.

3. UOW rights

3.1. You grant UOW a perpetual, non-exclusive, worldwide, royalty-free, sub-licensable licence to:

(a) deposit the Work in the Digital Repository;

(b) distribute copies of the Work (including the abstract) in electronic format;

(c) electronically store and copy the Work; and

(d) convert the Work to any format necessary for the preservation of the Work or the deposit on the Digital Repository.

3.2. UOW:

(a) may remove the Work from the Digital Repository for professional or administrative reasons at its sole discretion;

(b) is not under any obligation to take legal action on your behalf in the event breaches of your intellectual property rights stem from the deposit of the work in the Digital Repository;

(c) is not under any obligation to reproduce, transmit, broadcast or display the work in any particular format; and

(d) is not liable for any loss or damage to the Work whilst stored in the Digital Repository.

3.3. If you have used another person's copyright work without consent as identified under item 10 of the Key Details UOW may:

(a) remove this material from the Work and deposit in the Digital Repository;

(b) deposit only the metadata of the Work in the Digital Repository; or

(c) elect not to deposit the Work in the Digital Repository.

I declare my digital thesis is the final version approved by the University for the award of the degree.

Student (candidate) signature	Supervisor signature
25/8/15	25/8/15
Date of student (candidate) signature	Date of supervisor signature